Parylene for MEMS Applications

Thesis by

Tze-Jung Yao

In Partial Fulfillment of the Requirements
for the Degree of Doctor of Philosophy

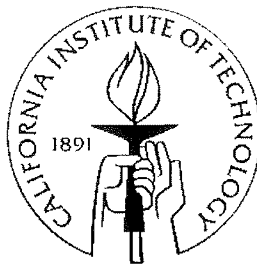

California Institute of Technology
Pasadena, California, USA
2002

(Defended January 9, 2002)

© 2002
Tze-Jung Yao
All Rights Reserved

To my wife,
Yi-Ping Liu,
who made this possible

Acknowledgements

First of all, I would like to thank my advisor, Dr. Yu-Chong Tai, for giving me a chance to participate in his esteemed group to study the intriguing field of micromachining, and for his many years of guidance. Furthermore, I want to thank him for his constant suggestions, non-stopping inspiration, and most importantly, the freedom he gave me to explore any new knowledge that interested me. Without his academic excellence, I would not have grown as fast and think as clearly as I did during my graduate school years. His spiritual encouragement and philosophical advice have been the greatest assets that I have gained during my graduate studies. To me, he has not only served as an advisor but a mentor as well whom I will always be indebted to.

I would also like to thank my committee, Prof. William Bridge, Prof. Jerome Pine, Prof. Michael Shumate, and Prof. Theodore Wu for spending time during the holidays to read my thesis and for participating on the defense committee for discussions.

Words can not describe the appreciation I have for my wife, Yi-Ping Liu, whom I met during my first year of study at Caltech. Her love, encouragement, thoughtfulness, and support have been my motivation for continuation after long, repetitive, and painful experimental failures. Her laugh, sunny smile, and incessant nagging have been the strongest driving force for me to finish the study. She has been the radiance that shines upon my successes and my beloved confidant during the roughest times. Although "thank you" is not enough to repay all the negligence, bad temper, and the fighting I have given her, I still want to say that without her, I could not have reached the achievement that I have today.

I would also like to thank my parents, who have sacrificed so many years to bring me to the stage where I am right now. Their discipline, support and endless caring which I could never repay have inspired me to make sure that someday, I will make them proud.

I would also like to thank all my colleagues, who have helped me in the lab and on my numerous experiments. Ever since I joined the group, Dr. Xing Yang had constantly taught me stuff I was interested in and to always ask why. I have learned so much from his broad knowledge and technical expertise, especially the patience that he has in dealing with details. Dr. Charles Grosjean was always kind and had answers for me no matter what question I asked. His cleverness and technical skills both inside and outside the lab have made me believe that there is much more out there that I have to learn and excel at. Dr. Wen H. Hsieh, with his non-exhausted energy and excellent laboratory skills, has helped me to get an early start with the research.

I would also like to thank Dr. Sangwook Lee, who served as my mentor during my second year of study. From him, I have learned and qualified all the necessary equipments that I need for my research. My thankfulness for the tremendous time and effort that he has spent on me is beyond what words can describe. Over time, we have become not only lab partners but also close friends who have shared the details of life trivia. His suggestions and past experiences have helped me to elucidate the mysteries that I encountered during daily life.

I would like to thank for Mr. Ken Walsh and Mr. Theodore Harder for their contributions of the data they had help to collect for my experiments. I would also like to thank all the colleagues, especially Dr. Hsu-Tseng Yang, Dr. Weilong Tang, Dr. Tom Tsao, Dr. Xuan-Qi Wang, Dr. Fukang Jiang, Yong Xu, Ellis Meng, Zhigang Han, Jun Xie,

and Qing He, who all have given me a tremendous amount of assistance in the laboratory during my study at Caltech. Without them, my experiments could not have gone as smoothly as planned.

I would also like to thank Tanya Owen, who has helped me all the time in dealing with the administration issues so I had one less thing to worry about it. Special thanks go to our lab technician, Mr. Trevor Roper, who always cleaned up the messes that I have done in the laboratory and the screw-ups I did to the machines. Without his diligent help, my Ph.D. would not have been completed in time.

Finally, I would like to thank NSF/ERC and DARPA for their financial support to make my graduate study possible, Caltech for giving me the chance to pursue a Ph.D. in the department of Electrical Engineering, and Agilent Technologies for their partial financial support on the work presented in Chapter 5 of the thesis.

Parylene for MEMS Applications

Thesis by
Tze-Jung Yao

In Partial Fulfillment of the Requirements
For the Degree of
Doctor of Philosophy

Abstract

The goal of this thesis is to utilize Parylene, a room-temperature chemical-vapor-deposited (CVD) polymer, for MicroElectroMechanical Systems (MEMS) applications. The identified unique properties of Parylene are used to fabricate various micromachining devices such as thermopneumatic microvalve, in-channel microflow restrictor, and electret microphones.

First, the properties of Parylene as a MEMS material are reviewed. The electrical, thermal, surface, and mechanical properties are first compared with that of other materials and further studied specifically for MEMS applications. The high dielectric strength (determined as 250V/μm) of Parylene makes it suitable for use as an electrical insulation material. However, its high resistivity causes un-desired charging effects first described in polymer-based electrostatic devices. The undesired high pull-in voltage, "bounce-back," and "snap-down" effects caused by dielectric charging are studied.

Second, to make Parylene as a surface-micromachined material, a process that overcomes the stiction problem has to be developed. Thus, a new technique that combines wet-acetone dissolution and dry BrF3 dry etching has developed to overcome the stiction problem, which prevents Parylene microstructures from freestanding. The devices of mm*mm size with high yield are demonstrated using this technology.

A thermopneumatic microvalve with a corrugated silicone/Parylene composite membrane is designed, fabricated, and tested for gas flows of several slpm and inlet pressures of tens of psi. The lowest power consumption to turn off the gas flow is determined to be 73mW. A silicone-based microfluidic coupler, initially designed for microvalve packaging, is also demonstrated for its ability to connect the external macrofluidic world to microfluidic devices. The demonstrated "quick-connect" microfluidic coupler has low leakage, is reusable, and can maintain good seal up to 60 psi.

An in-channel microflow restrictor is also demonstrated with freestanding Parylene integration technology. The demonstrated restrictor can modulate flow at several tens of *nl/min* range with inlet pressures of several psi. The restrictor, although AC-actuated, can modulate the flow up to 50%.

Finally, an electret microphone with thin-film Teflon AF is demonstrated. Parylene is shown to enhance the rigidity and yield of the microphone back plate. The demonstrated electret microphone has an open sensitivity of up to 45mV/Pa with a bandwidth of up to 10KHz.

Table of Contents

Chapter 1: Introduction

1.1 Background 1
1.2 Silicon Microfabrication for MEMS Applications 3
1.2.1 Bulk Micromachining 4
1.2.2 Surface Micromachining 6
1.2.3 Wafer Bonding 9
1.2.4 LIGA Micromachining 9
1.3 Comparison of the Actuation Mechanisms 10
1.3.1 Electrostatic Actuation 11
1.3.2 Electromagnetic Actuation 12
1.3.3 Bimetallic/ Thermal Actuation 13
1.3.4 Thermopneumatic Actuation 15
1.4 Thesis Outline 16
1.5 References 18

Chapter 2: Parylene as a MEMS Material

2.1 Backgrounds 23
2.1.1 Integration with MEMS and Electronics 24
2.1.2.Parylene deposition Process 26
2.1.3 Pattern Parylene using Oxygen Plasma 27
2.1.4 Substrate Preparation prior to the deposition 29
2.2 Basic Parylene Properties 32
2.3 Electrical Properties of Parylene 34
2.3.1 Dielectric Strength of Thin-Film Parylene 34

2.3.2 Charge Retention Capabilities of Parylene Thin-Film....38

2.4 Mechanical Properties of Parylene....41

2.4.1 Stresses in thin-Film....41

2.4.2 Comparison of Stress Measurement Methods....43

2.4.3 Measurement of Stresses in Thin-Film Parylene....54

2.5 Thermal Properties of Parylene....57

2.6 Surface Properties of Parylene Thin-Film....58

2.6.1 Parylene Surface characterized by Contact Angle Measurement....59

2.6.2 Measurement of flow in Parylene Microchannel....61

2.7 Conclusions....71

2.8 References....72

Chapter 3: Thermopneumatic Microvalve with Corrugated Parylene Membrane

3.1 Preface....77

3.2 Structures of the Thermopneumatic Microvalve....79

3.3 Thermopneumatic Actuation....81

3.4 Fabrication of Components for Thermopneumatic Microvalve....81

3.4.1 Silicone Rubber as Membrane Material....84

3.4.2 Parylene as a Solvent Barrier....87

3.4.3 Design and Fabrication of silicone/Parylene composite membrane....89

3.4.4 Improved Valve-Seat for packaging and Channel characterizations....94

3.5 Testing of themopneumatic microvalve....96

3.6 Micromachined Rubber O-ring Micro-Fluidic Couplers....99

3.6.1 Previous Demonstarted Coupling Methods....99

3.6.2 Design and Fabrication Process....103

3.6.3 Experimental Characterization....105

3.7 Conclusion 109

3.8 References..110

Chapter 4: BrF_3 Dry Release Technology for Large Freestanding Parylene MEMS

4.1 Introduction..115

4.2 Selection of the Sacrificial Layer Material 117

4.2.1 LTO/PSG as Sacrificial Material 118

4.2.2 Metal as Sacrificial Material..119

4.2.3 Polysilicon as Sacrificial Material 119

4.2.4 Photoresist as Sacrificial Material 120

4.3 Problems of Freestanding Parylene 122

4.4 Existing Methods for Dry-Release Freestanding Microstructures.........................127

4.5 Dry Release Technology for Parylene Microstructures..134

4.5.1 Review of BrF_3 vapor etching of silicon..135

4.5.2 Design and Fabrication of Freestanding Parylene Microstructures...........137

4.6 Results and Discussion on Anti-stiction methods..138

4.7 Conclusion 142

4.8 References..143

Chapter 5: Parasitic Charging Effect on Parylene Electrostatic Actuators and a Surface Micromachined In-Channel Flow Restrictor

5.1 Preface...147

5.2 Parylene Electrostatic Actuator and its Interesting Problem 151

5.2.1 Bounce-Back Problem 152

5.2.2 High Pull-in voltage..153

5.2.3 Parylene Microstructures under SEM irradiation 154

5.3 Theoretical calculation of the charging effect and air breakdown mechanisms........157

5.3.1 Breakdown mechanism of Air medium 157

5.3.2 Theoretical examination of the charging effect on electro-static actuators 162

5.4 Experimental Results and Discussion 168

5.4.1 High threshold voltage 168

5.4.2 Bounce-Back effect 171

5.4.3 Temperature effect 173

5.4.4 Permanent charge damage—"Snap-down" Effect 175

5.4.5 Threshold voltage shift with cycles of operations 176

5.5 A Normally-Open In-channel Microflow Restrictor 176

5.5.1 Initial Buckling Valve concepts and problems 177

5.5.2 Design and characterization of modified microflow restrictor 181

5.6 Conclusion 187

5.7 References 188

Chapter 6: Thin-Film Teflon Electret Microphone with Parylene Backplate

6.1 Preface 191

6.2 Design of an Electret Microphone 194

6.2.1 Open Circuit Sensitivity 196

6.2.2 Frequency Response 198

6.2.3 Dynamic Range 200

6.3 The Electret—The Material and Formation 200

6.3.1 Teflon AF thin film 199

6.3.2 Charge implantation Method 202

6.4 Designs and Fabrications of a MEMS Electret Microphone 204

6.4.1 Fabrication Process and Issues 204

6.4.2 Design of a MEMS Electret Microphone 206

6.5 Testing of a MEMS Electret Microphone 208

6.6 Conclusion 209

6.7 References 210

Chapter 7: Conclusion 211

List of Figures

Chapter 1

Figure 1-1: Bulk micromachining 4
Figure 1-2: Surface micromachining 4
Figure 1-3: Pictures of the ADXL-150 accelerometers 7
Figure 1-4: Schematics of the MUMPs Processes 7
Figure 1-5: SUMMiT V™ fabrication process from Sandia National Lab 8
Figure 1-6: Pictures of the microstructures fabricated by LIGA process 10
Figure 1-7: The pressure generated by electrostatic force 11
Figure 1-8: Optical modulators using electromagnetic force 13
Figure 1-9: Self-assembled optical mirrors...14

Chapter 2

Figure 2-1: Chemical structures of Parylene 25
Figure 2-2: Parylene deposition Systems...26
Figure 2-3: Coupling schemes of alkyltrichlorosilanes 29
Figure 2-4: Coupling schemes of alkoxysilanes 30
Figure 2-5: Some commercially available coupling agents...31
Figure 2-6: Low temperature Parylene Process 32
Figure 2-7: Parallel capacitor with Parylene Dielectrics 34
Figure 2-8: Simplified process flow of parallel capacitor 35
Figure 2-9: Experimental setup for measuring I-V curve with current limiter.................36
Figure 2-10: Voltage-Current relationship of a Parylene dielectric capacitor prior to breakdown...36
Figure 2-11: The breakdown moment of Parylene Film..37
Figure 2-12: The positive and negative charge density deposited on Parylene surfaces using Zerostat gun 38

Figure 2-13: The positive charges decaying at room temperature and elevated temperatures....39
Figure 2-14: The volume resistivity of Parylene decreases at elevated temperatures....40
Figure 2-15: The effect of bad stress control....41
Figure 2-16: The method for making freestanding Parylene membrane for bulge test....44
Figure 2-17: Typical Load-Deflection curve for Parylene membrane....47
Figure 2-18: Surface micromachined fabrication steps for In-plane strain gauges....48
Figure 2-19: Unfinished T(a)/H(b) structures of In-plane starin gauges due to the undercutting capability of BrF_3 vapor phase etching....49
Figure 2-20: Photos of Guckle Ring structures by Parylene....49
Figure 2-21: Photos of push-pull structures by Parylene....49
Figure 2-22: Geometrics of the rotating tips for measuring Parylene Stress....50
Figure 2-23: A bad rotating-tips; the connections are broken....51
Figure 2-24: Correction factors as function of the turning-point width....53
Figure 2-25: Parylene stress vs. theoretical thermal mismatch (only TCE of Parylene considered)....53
Figure 2-26: Parylene stress vs. theoretical thermal Mismatch (possion ratio and TCE differences considered)....54
Figure 2-27: Photos of rotating tip at elevated Temperatures....56
Figure 2-28: Parylene stresses vs. theoretical thermal mismatch (initial stress is considered)....56
Figure 2-29: Photos of rotating tips used to measure thermal expansion of coefficient (TCE)......57
Figure 2-30: Schematics of liquid/solid/air interface at equilibrium.....59
Figure 2-31: The configuration of a microchannel....62
Figure 2-32: Fabrication steps of surface micromachined Parylene microchannel....66
Figure 2-33: The Parylene channels....66
Figure 2-34: The position of a capillary meniscus vs. time of DI water filling into a Parylene channel....67
Figure 2-35: The position of a capillary meniscus vs. time of different liquids filling into a silicon nitride microchannel....68

Figure 2-36: The effect of HF cleaning. 69

Chapter 3

Figure 3-1: The structure of designed thermopneumatic microvalve 79
Figure 3-2: Crosslinking of silicone by room temperature vulcanization RTV 84
Figure 3-3: Crosslinking of silicone by addition-cure 85
Figure 3-4: Squeegee Coating of Silicone. 86
Figure 3-5: Comparison of permeability of various materials for moisture. 87
Figure 3-6: Parylene barrier properties for moisture and gas 88
Figure 3-7: The pressure vs. deflection relationship for corrugated Parylene Membrane.90
Figure 3-8: The simplified fabrication steps for corrugated Parylene membrane 92
Figure 3-9: Photos of finished corrugated Parylene/silicone composite membrane....93
Figure 3-10: Bulge-test setup used for measuring membrane performance 93
Figure 3-11: Pressure-Deflection relationship for corrugated Parylene/silicone composite membrane....94
Figure 3-12: Simplified process flow for improved valve seat....95
Figure 3-13: Alpha-step scanned surface-profile on silicone membrane 95
Figure 3-14: Flow rate of the channel formed by the corrugated membrane at various pressure 96
Figure 3-15: The finished device sitting on a quarter 96
Figure 3-16: The simple ON-OFF testing on microvalve....97
Figure 3-17: The flow rate vs. power consumption at different inlet pressures 98
Figure 3-18: Schematics of microfluidic coupler proposed by *Meng et al.* 101
Figure 3-19: Schmeatic view of the O-ring coupler application....102
Figure 3-20: Simplified process for making rubber O-ring fluidic coupler 103
Figure 3-21: Photos of finished O-rings 104
Figure 3-22: View of the assembled rubber O-ring and tubes inserted in O-ring 104
Figure 3-23: Pressure test (a) at 0 psi (b) at 20 psi 105
Figure 3-24: Experimental setup for leak rate measurement. 105
Figure 3-25: The tube under 20psi remains sealed over 12 hours 106
Figure 3-26: Experimental setup of pull-out Test....106

Figure 3-27: The pull-out test results on rubber O-ring....108
Figure 3-28: The reliability test on Rubber O-ring....109

Chapter 4

Figure 4-1: Theoretical calculation of beam deflection due to gravity....116
Figure 4-2: SEM of Parylene surface after long BrF_3 exposure....120
Figure 4-3: SEM of Parylene microchannel using Photoresist as sacrificial layer....121
Figure 4-4: Pictures of stiction of Parylene cantilever beams and diaphragms....123
Figure 4-5: Schematics of evaporation drying process....124
Figure 4-6: Schematics used to explain the Laplace Pressure....125
Figure 4-7: Theoretical calculation of detachment length....127
Figure 4-8: Schematic of different drying process....128
Figure 4-9: Photos of Parylene diaphragms after CO_2 supercritical drying....130
Figure 4-10: Pictures of polynorborene decomposition sacrificial layer technology....132
Figure 4-11: Anti-stiction methods for Parylene freestanding microstructures....134
Figure 4-12: Process flow for Anti-stiction approaches....136
Figure 4-13: Stiction of Parylene microstructures due to large post spacing....138
Figure 4-14: Structures fabricated with the first approach....138
Figure 4-15: WYKO profile of the hole underneath the post etched by BrF_3....139
Figure 4-16: Structures released by sputter silicon method....140
Figure 4-17: Miscellaneous freestanding Parylene microstrutures....141

Chapter 5

Figure 5-1: A SEM Photo showing the Digital Mirror Display and its underlying elements....148
Figure 5-2: Schematics of original buckling valve ideas....149
Figure 5-3: Simplified process flow for Parylene electrostatic actuators....151
Figure 5-4: Photos of fabricated Parylene electrostatic actuators....152
Figure 5-5: Schematics of "bounce-back" effect....152
Figure 5-6: Experimental and theoretical pull-in voltagr for Parylene electrostatic actuators....154

Figure 5-7: Movement of freestanding cantilever beams under SEM 156
Figure 5-8: Paschen's curve 161
Figure 5-9: Voltage vs. Current in a discharge tube 161
Figure 5-10: Schematic of residual charge on Parylene/air interface 162
Figure 5-11: Schematics of mechanical representation of electrostatic actuator 162
Figure 5-12: Threshold voltage of electrostatic actuator as function of temperature 173
Figure 5-13: "Snap-down" effect 174
Figure 5-14: Changes of pull-in voltage over cycles of "bounce-back" 175
Figure 5-15: The original ideas of buckling valve 177
Figure 5-16: The initial prototypes of buckling valve—torsional plate 178
Figure 5-17: The initial prototypes of buckling valve—cantilever plate 179
Figure 5-18: The modified concept for in-channel flow restrictor 179
Figure 5-19: The flow rate vs. inlet pressure for cantilever type flow restrictor 180
Figure 5-20: The flow rate of cantilever types measured along different locations across the plate 181
Figure 5-21: The modified design of in-channel flow restrictor with wedge 182
Figure 5-22: The simplified process flow for in-channel flow restrictor with wedge 182
Figure 5-23: The finished in-channel flow restrictor with wedge 184
Figure 5-24: The SEM photo of finished flow restrictor with wedge 184
Figure 5-25: The flow rate vs. inlet pressure for cantilever type flow restrictor with wedge 185
Figure 5-26: The probe test for cantilever type flow restrictor with wedge 185
Figure 5-27: The measured flow rate against inlet pressure using ac-actuated electrostatic force at 20Hz (with a duty cycle of 50%) 186

Chapter 6

Figure 6-1: Externally biased and self-biasing (electret) microphone 193
Figure 6-2: Schematics of an electret microphone 194
Figure 6-3: Schematics of Teflon AF electret/air interface 196
Figure 6-4: The Back-Lighted Thyratron (BLT) 202

Figure 6-5: The Teflon AF electret generated by BLT at various annealing temperatures............203
Figure 6-6: Simplified fabrication Process flow for an electret microphone............204
Figure 6-7: Photos of fabricated microphone chips............205
Figure 6-8: The frequency response of the electret condenser microphone............208
Figure 6-9: The custom-made package for electret microphone measurement............208

Chapter 7 (no figures)

List of Tables

Chapter 1

Table 1-1: Comparison of common silicon etchants 6

Table 1-2: Thermal conductivites and expansion coefficient of the typical materials used in MEMS..14

Chapter 2

Table 2-1: Critical Temperatures for Surface Micromachining 25

Table 2-2: Adhesion of the materials on Parylene...28

Table 2-3: Parylene Properties...33

Table 2-4: Contact angle measurements on different Parylene-C surfaces.......................60

Table 2-5: The experiment results of water-filling experiments 68

Chapter 3

Table 3-1: Fluid Properties for thermopneumatic operation...82

Table 3-2: Physical Properties of MRTV 1 86

Table 3-3: Leak rate Tests on Rubber O-ring with different inner diameters 107

Chapter 4

Table 4-1: Physical Properties of BrF_3 136

Chapter 5 (no tables)

Chapter 6

Table 6-1: Selected Properties for Teflon AF 1601S 201

Chapter 7 (no tables)

CHAPTER 1

Introduction

Abstract

In this chapter, the backgrounds of simple micromachining techniques will be described. Several different actuation mechanisms used in various devices will be discussed, and the outline of thesis work will be given.

1.1 Background

"I would like to describe a field, in which little has been done, but in which an enormous amount can be done in principle. This field is not quite the same as the others in that it will not tell us much of fundamental physics (in the sense of, `What are the strange particles?'), but it is more like solid-state physics in the sense that it might tell us much of great interest about the strange phenomena that occur in complex situations. Furthermore, a point that is most important is that it would have an enormous number of technical applications [1]." Just as the first transistor invented at Bell Labs in 1957 has revolutionized the way people live everyday, MEMS (MicroElectroMechanical Systems) which borrows technologies developed in the microelectronics industry has penetrated people's daily lives. The silicon-based pressure transducers that were first commercialized in the 1970s [2] have found tremendous applications in automotive

industries, such as the monitoring of intake manifold engines so that the amount of fuel required for each engine cylinder can be computed. Accelerometers that measure in the 0-to-50g range have been employed in air bag systems in almost every car today for crash sensing [3]. Inkjet printer with 12 to 24 30 μm-micromachined nozzles per millimeter are used daily to achieve 300 to 600dpi resolution [4]. Home theater projectors, which make use of a technology called Digital Light Processing (DLP) from Texas Instruments Digital Mirror Display (DMD) [5], are starting to emerge on the markets. Thus, micromachining has provided a very powerful platform in fabricating **SENSORS** that sense environmental parameters such as pressure, temperature, and magnetic field and **ACTUATORS** that respond to environmental parameters to provide electrical, mechanical and thermal signals, which are then integrated with microprocessors that process the response between inputs and outputs.

K.E. Petersen [2], in his legendary review paper "Silicon as Mechanical Material," in which he contributed the success of micromechanics to silicon in conjunction with its conventional role as an electronics material, pointed out that silicon can be explored as a high-precision, high-strength, highly-reliable mechanical material. Since then, tremendous work has been done since the 1970s in the area of polysilicon micromechanics, especially in the expansion of material selection that is not commercially used in microelectronics industry such as quartz, gallium arsenide GaAs, TiNi alloy, and ceramics. In the late 1980s, the United States Defense Advanced Research Project Agency (DARPA) has invested tremendously in MEMS research, leading to proposals involving broad applications that use MEMS as an enabling

technology in biomedical sensing and detection, optical communication, RF wireless communications and display.

Although MEMS technology is not restricted to one single material, device or processing technique, it is usually subdivided into bulk micromachining, surface micromachining, wafer bonding, and LIGA. In the next section, those techniques will be summarized to provide some fundamental knowledge of this growing field.

1.2 Silicon Microfabrication for MEMS Applications

The United States is not alone in recognizing the potential impact of MEMS technology. The name MEMS (**M**icro**E**lectro**M**echanical **S**ystems) is used for the DARPA program, and therefore has found acceptance among most U.S. researchers. Overseas, the Japanese government has increased its support of MEMS R&D funded through the Ministry of International Trade and Industry (MITI) under the Micromachines Project. Investments by European Governments, primarily Germany, Switzerland, Netherlands, and France, are coordinated through the European Community to reduce research duplication and promoting collaboration across borders on what is described by them as MST (Microsystem Technologies). Although different names such as micromachining, MEMS, MST, and Micromachines exist, this field is generally differentiated by its separate technologies: bulk micromachining, surface micromachining, wafer bonding, and LIGA. Over the years, many other MEMS techniques have also been developed such as 3-D stereolithography [6], micro-electrical discharge machining (Micro-EDM) [7], laser micromachining [8], and plastic injection molding [9]. However, this section will overview the fundamental techniques to provide the base knowledge of

this field. Detailed treatments on extended topics can be found in more descriptive literature (i.e., [2,10-12]).

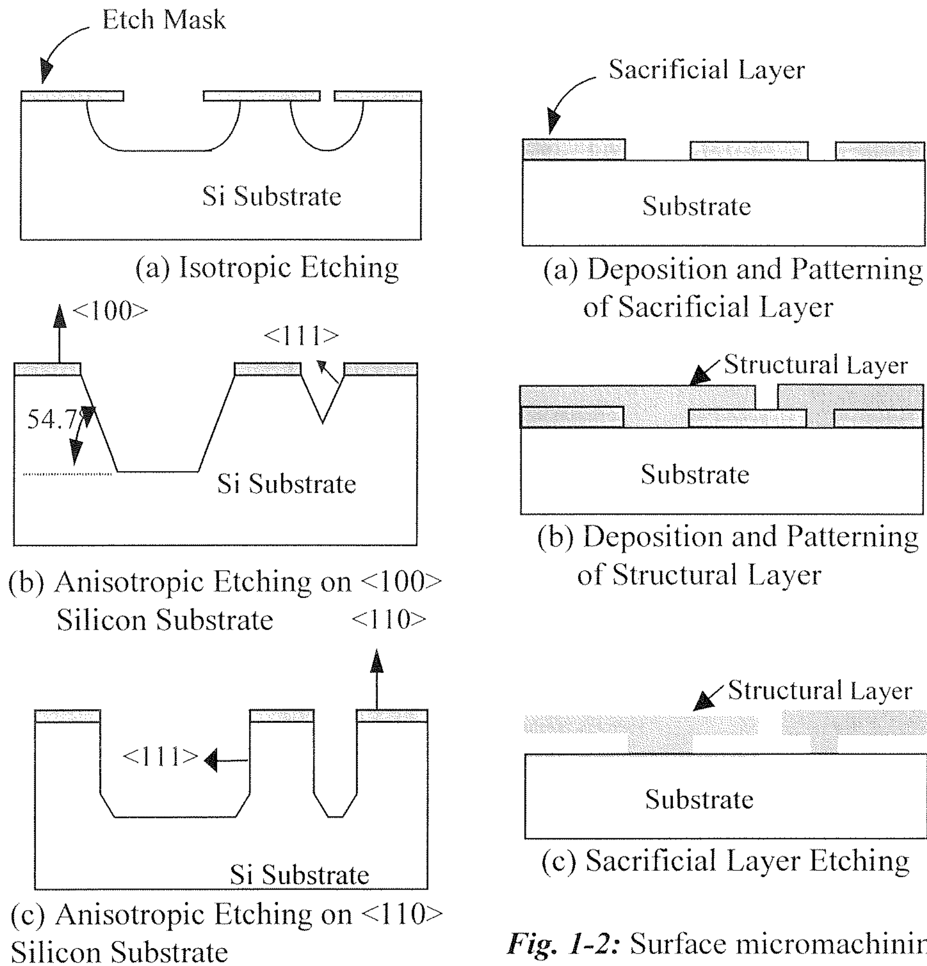

Fig. 1-1: Bulk micromachining (from [32])

Fig. 1-2: Surface micromachining (from [32])

1.2.1 Bulk Micromachining

In bulk micromachining, three-dimensional microstructures are typically created by selectively removing the substrate material, mostly bulk silicon substrate. The removing process as shown in Fig. 1-1 can be done either through anisotropic etching in which the etching rate is dependent on the crystalline direction of the substrate, or isotropic etching in which the crystalline structure of the substrate has only minor effects

on the etching rate. The etching processes can be also divided into either dry-etching or wet-etching depending on the phase of the etchants. For example, Table 1-1[10] shows a comparison of different etchants typically used to create three-dimensional bulk-micromachined structures such as HNA (HF+HNO_3+Acetic acids), Alkali-OH (KOH is mostly used), EDP (ethylene diamine pyrochatechol), TMAH (tetramethyl-ammonium hydroxide), XeF_2, SF_6 plasma and DRIE (deep reactive ion etching). The selection between different etchants may be determined by its applications; for example, KOH solution is mostly used to create the groove structures on (100) silicon shown in Fig. 1-1(b) using silicon dioxide SiO_2, or silicon nitride Si_xN_y as masks. However, the same etchants can be used to create vertical sidewalls on (110) silicon substrate shown in Fig. 1-1(c).

Moreover, etchants such as TMAH is metal-ion-free which makes it compatible with CMOS integrated circuits to accomplish MEMS/IC integration. Vapor phase etchants such as XeF_2 etches silicon spontaneously at room temperature and usually have large selectivity over mask materials due to their inherent chemical etching characteristics. Moreover, dry-vapor isotropic etching also has the advantage of preventing stiction problems commonly encountered in releasing fragile micromachined structures. This property will be explored later in the thesis. Finally, dry plasma etching (i.e., DRIE) helps to create high-aspect-ratio microstructures in silicon from 30:1 up to millimeter depths, which enables it to overcome the constraints that most micromachined structures have on limited z-direction stiffness.

Table 1-1: Comparsion of common silicon etchants

	HNA	KOH	EDP	TMAH	XeF_2	SF_6 plasma	DRIE
Etch type	Wet	Wet	Wet	Wet	Dry	Dry	Dry
Anisotropic	No	Yes	Yes	Yes	No	Varies	Yes
Availability	Common	Common	Moderate	Moderate	Limited	Common	Limited
Si etching rate (μm/min)	1 to 3	1 to 2	1 to 30	~1	1 to 3	~1	>1
Roughness	Low	Low	Low	Varies	High	Variable	Low
Etch Nitride?	Low	Low	Low	1 to 10nm/min	Low	Low	Low
Etch Oxide?	10 to 30nm/min	1 to 10nm/min	1 to 80nm/min	~1nm/min	Low	Low	Low
Al Selective?	No	No	No	Yes	Yes	Yes	Yes
Au Selective?	Likely	Yes	Yes	Yes	Yes	Yes	Yes
P++ etch stop?	No	Yes	Yes	Yes	No	No	No
Electrochemical Stop?	?	Yes	Yes	Yes	No	No	No
CMOS Compatible ?	No	No	Yes	Yes	Yes	Yes	Yes
Cost	Low	Low	Moderate	Moderate	Moderate	High	High
Disposal	Low	Easy	Difficult	Moderate	N/A	N/A	N/A
Safety	Moderate	Moderate	Low	High	Moderate	High	High

1.2.2 Surface Micromachining

Unlike bulk micromachining where the bulk material is selectively etched, the structural materials shown in Fig. 1-2 in surface micromachining are intentionally added-on to the substrate. The structural materials are finally released and become freestanding from the substrate by etching the sacrificial layer away. The most dominant material combination for structural material and sacrificial layer are polysilicon and phosphosilicate glass (PSG), which in Fig. 1-3 is demonstrated as ADXL-150 surface

micromachined accelerometers integrated with on-chip BiCMOS signal conditioning circuitry.

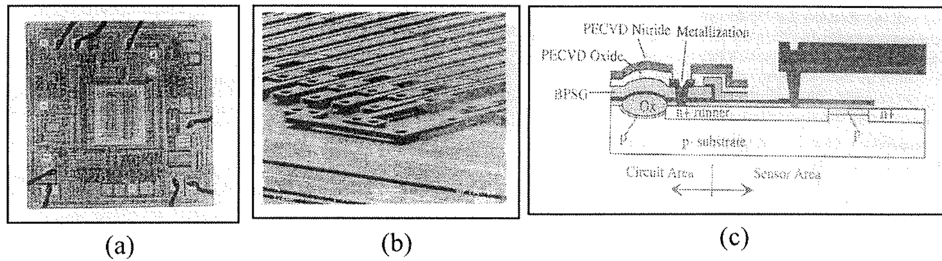

(a) (b) (c)

Fig. 1-3: Pictures of the ADXL-150 accelerometers [12]
(a) Photo of ADXL-150 die
(b) SEM photo of sensor part of ADXL-150
(c) Schematic of final released structures

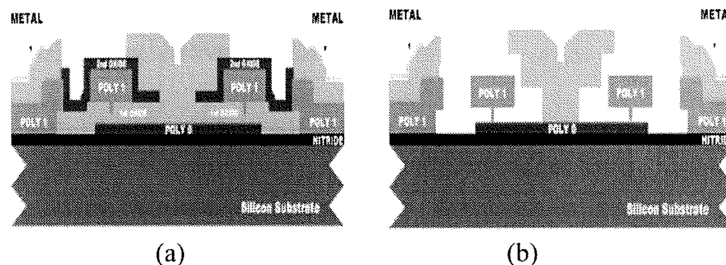

(a) (b)

Fig. 1-4: Schematics of the MUMPs processes
(a) The structure prior to BHF release
(b) The released MEMS structures

Many interesting devices are fabricated and demonstrated using polysilicon surface micromaching techniques such as resonators [13], micro-pin joint sliders [14], grippers [15], micromotors [16], and micromirrors [17]. Some of the devices are previously fabricated through MUMPs (Multi-use-MEMS Process) shown in Fig. 1-4 provided by MCNC foundry services [18], now Coronos (aquired by JDS Uniphase), which employs three-layer polysilicon layers and two-layer PSG layers. The similar Ultra-planar, Multi-level MEMS Technology for Five levels (SUMMiT V™) fabrication process from Sandia National Lab is a five-level polycrystalline silicon surface

micromachining process. Several devices [19] are also fabricated using the technology as shown in Fig. 1-5.

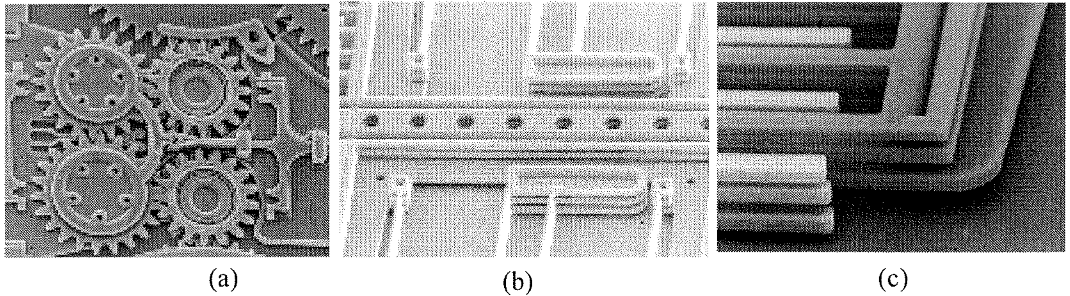

(a) (b) (c)

Fig. 1-5: SUMMiT V™ fabrication process from Sandia National Lab

(a) Meshing gears on a moveable platform.

(b) Laminated support springs containing only three mechanical layers result in more than 2 orders of magnitude greater out-of-plane stiffness compared to a single mechanical layer.

(c) A laminated comb actuator results in nearly five times the electrostatic force of a single level actuator.

Since the structural material is an added-on material rather than the substrate, there is no constraint that requires the structural material to be polysilicon. Several different combinations of structural material and sacrificial layer have been developed such as aluminum/polyimide [20], polysilicon/copper [21], and silicon nitride/PSG [22]. However, in order to utilize a specific combination, several issues must be addressed first. The add-on material is typically thin (in the range of ~μm), so the control of material quality such as Young's modulus and residual stress is important to prevent the curving of the structures after releasing. Second, because of the inherently small gap in surface micromachined processes, the structure tends to stick onto the substrate after the wet chemical releasing due to the surface tension. Both of these topics will be discussed in more detail in later sections.

1.2.3 Wafer Bonding

Wafer bonding is also an essential technique in micromachining to permanently couple similar or dissimilar materials together. Over time, several different techniques have been developed for different materials and applications such as silicon/Pyrex anodic bonding [23], silicon/silicon fusion bonding [24], and photoresist gluing. Although it may not seem significant or actively researched, most of the costs involved in commercializing micromachined devices lie in wafer bonding and packaging. MEMS devices, especially those that are bulk-micromachined, usually consist of more than one substrate and therefore require permanent bonding. The bonding processes are usually low-yield, time-consuming and labor-intensive; therefore, it drastically reduces the overall yield of the MEMS devices. However, to the author's knowledge, there is no ideal and universal bonding solution, especially one that can be applied to polymers, which can only withstand low temperatures.

1.2.4 LIGA Micromachining

LIGA, the German acronym for X-ray lithography (X-ray lithographie), electrodeposition (galvanoformung), and molding (abformtechnik), usually involves a thick layer of X-ray resist from μm to cm range, a high-energy X-ray source, and subsequently developing and electrodeposition to form the desired three-dimensional structures. The advantage of LIGA processes is to enable high aspect ratio structures up to centimeter height as shown in Fig. 1-6 [25]. However, the expensive mask-making processes and scarce synchrotron source make it suitable only for selected applications such as making mold inserts as shown.

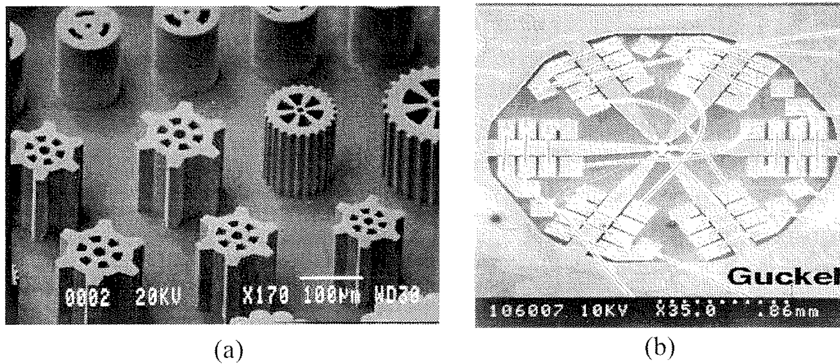

(a) (b)

Fig. 1-6: Pictures of the microstructures fabricated by LIGA process

(a) Various gears created at MCNC using the LIGAMUMPS, a multiple user LIGA fabrication process. The gears are all about 100 microns across and about 150 microns tall.

(b) The micromotor at the University of Wisconsin, Madison. The wire bonding that is shown is used to complete the windings of the stator electromagnets.

1.3 Comparison of the Actuation Mechanisms

By definition, actuators are devices that transform electrical energy into mechanical energy. Over the past few decades, several actuation mechanisms have been proposed and demonstrated to perform in the micro-domain. However, there has yet to be a "perfect" mechanism that can provide large force, long working distance, energy efficiency, low operating temperature, and simple fabrication simultaneously. Therefore, selection of the actuation mechanism is done on a case-by-case basis. Within the numerous actuation mechanisms that have been proposed, the electrostatic, electromagnetic, thermal bimetallic, and thermopneumatic forces are the most well-accepted mechanisms used in the micro-actuation field and therefore will be first discussed here. The purpose of this section is to provide an estimation of the various actuation mechanisms so that a particular mechanism can be identified easily for the design of specific applications.

1.3.1 Electrostatic Actuation

Over the past decades, electrostatic actuation has found tremendous applications in micromachining devices. The fundamental principle behind it is simply the Columbic attraction force between two oppositely charged plates. Taking a simple parallel-plate capacitor as an example, the force between two plates can be expressed as follows:

$$F = \frac{dW}{dx} = \frac{1}{2}\frac{\varepsilon A V^2}{x^2} \tag{1.1}$$

where

F : the electrostatic attraction force

W : the energy stored in the system

ε : dielectric constant (here, we use air $\varepsilon = 8.85 * 10^{-12}\ N/V^2$)

A : the area of the electrodes

V : the applied voltage

x : the gap beteen the electrodes

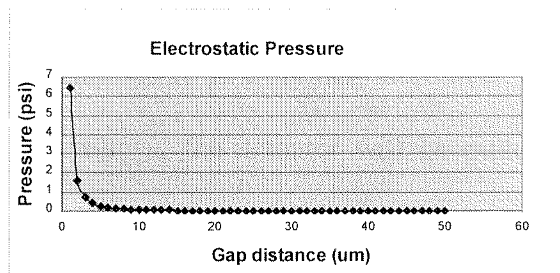

Fig. 1-7 The pressure generated by electrostatic force (voltage=100V)

Therefore, in order to get a large force, the gap between two parallel plates has to be small. Otherwise, the voltage required to achieve the force would be tremendously high. For example, Fig. 1-7 shows the pressure generated using electrostatic actuation with voltage V=100V; it is clear that the pressure generated is less than 1psi unless the gap is less than 3μm. However, for many micromachining applications, it is relatively

easy to fabricate closely spaced electrodes with small gaps. The low power consumption and fast frequency response also makes this actuation mechanism well accepted.

Comb-drive electrostatic actuators that make use of large numbers of interdigitated fingers have become an important building block for many MEMS devices [3,13,26], not only for actuators but also for sensors. For example, ADXL series of accelerometers from Analog Devices has employed feedback stabilization with on-chip electronics to overcome the inherent nonlinear voltage-to-position relationship in electrostatic actuation.

Several other important inventions based on electrostatic actuation have been demonstrated such as micromotors [16], microgrippers [15], resonators [13], and scratch-drive actuators [26]. To conclude, electrostatic actuators are typically used for movement with less than 10μm gap spacing. Several drawbacks of using electrostatic actuators are: (1) the position-to-voltage relationship is extremely nonlinear, and when the voltage is above some certain pull-in voltage, the actuator will be pulled into contact with the substrate [12] (2) at large distances, the fringing field capacitance becomes non-negligible and the voltage required is too high for most applications.

1.3.2 Electromagnetic Actuation

A current-carrying conductor in magnetic field will experience a Lorentz force according to the following:

$$F = (I * B)L \tag{1.2}$$

F : electromagnetic force
B : the magnetic field
L : length of the wire
I : the passing current

A simple calculation using I=1A, B=0.1N/m-A (commercially available), and L=1mm, the force in the range of 0.1mN, can be achieved. Several devices using electromagnetic actuation have been demonstrated. Shown in Fig. 1-8 is an optical modulator [27] using NiFe permalloy. The common drawback of using electromagnetic force is that the device has to be placed near an external and bulky permanent magnet. In addition, the current flowing through the wire is typically in the ampere range that may cause an undesired heating effect on the substrate. Moreover, to achieve high torque, the wire is usually formed into a coil shape, which consumes lots of chip area.

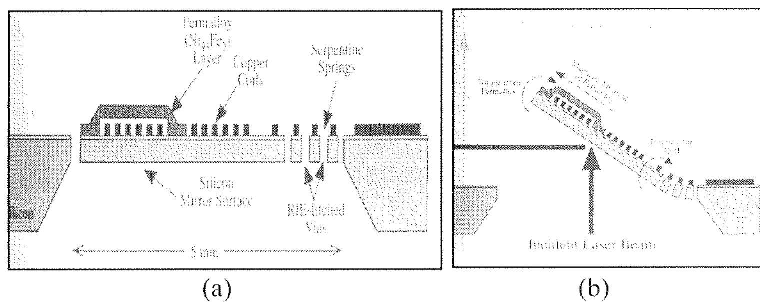

(a) (b)

Fig. 1-8: Optical modulators using electromagnetic force
(a) Device schematic
(b) Light modulation by deflecting a mirror

1.3.3 Bimetallic/Thermal Actuation

Bimetallic or thermal actuation makes use of the differences in thermal expansion coefficients between different materials [28], or the thermal expansion differences of a single material at different temperatures [29]. The advantage of thermal bimetallic actuation is that the force generated is typically large and that the structures are easily constructed by putting one material on top of another other and running current through them. For example, as shown in Fig. 1-9 [30], an array of thermal actuators are used to self-assemble a flipped-up mirror. Tables 1-2[10] shows that differences in thermal

expansion coefficients are usually small and therefore require high temperatures (several hundred degrees Celsius) to achieve the desired actuation. This high temperature operation usually limits the reliability of the devices.

Table 1-2:

Thermal conductivities and expansion coefficient of the typical material used in MEMS

Material	Thermal Conductivity (W/cm*K @300K)	Thermal Expansion Coefficient (ppm/K)
Aluminum	2.37	25
Gold	3.18	14.2
Carbon, diamond	23	-
Silicon	1.49	2.60
Silicon Dioxide (fused silica)	0.0138	0.4
Silicon Dioxide (thermal)	0.0138	0.35
Silicon Nitride	0.16	1.6
Polysilicon	0.34	2.33
Polyimide, Dupont PI2611d	-	3.0
Polyimide, Hitachi PIQ-3200	-	50
Teflon^{TM}(PTFE)	0.0225	-

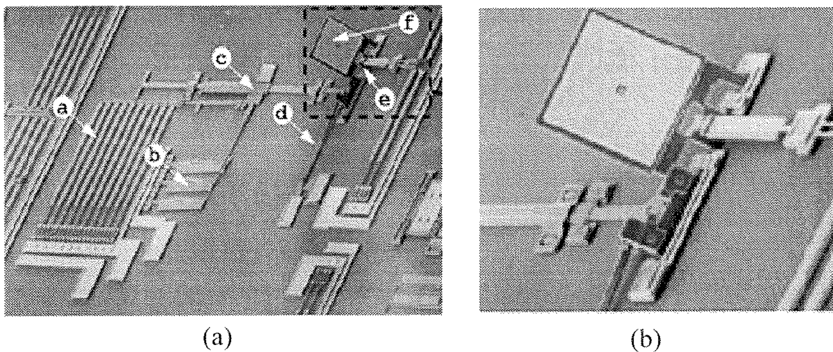

(a) (b)

Fig. 1-9: Self-assembled optical mirrors
(a) Device overview—thermal actuators are used to self-assemble the flip-up mirror
(b) Detailed photo of flipped-up mirror and its connection

1.3.4 Thermopneumatic Actuation

When either a liquid or gas is put into a constrained box and heated, it expands. However, if the volume is confined, pressure is generated inside the cavity. Taking gas expansion as example, assuming the gas is an ideal gas, where

$$P = \frac{nRT}{V} \tag{1.3}$$

P : the pressure inside the cavity (atm)
n : the number of mole
R : ideal gas constant 0.08206 L atm / mol K
T : absolute temperature (K)
V : volume (L)

In order to double the pressure inside the cavity, the absolute temperature has to be doubled and, therefore, the temperature required would be around 300°C, which is high for most applications. Devices such as micropumps [31] and microvalves [32] have been demonstrated using air as a working fluid.

Another approach in generating pressure utilizes the expansion of a liquid, which can be expressed as follows:

$$\Delta P = E(\beta\Delta T - \frac{\Delta V}{V}) \tag{1.3}$$

ΔP : Pressure change
E : bulk modulus of elasticity (psi)
β : thermal expansion coefficient (/°C)
ΔT : temperature increase
$\frac{\Delta V}{V}$: volume change percentage

Therefore, assuming there is no volume expansion, the pressure increase would be $E\beta(/°C)$. For water, where $E=3.3*10^5$psi, $\beta=2.3*10^{-4}$/°C, $E\beta$=76psi/°C, which is very high for most micromachined device applications. However, to utilize thermopneumatic

actuation with a liquid, the liquid has to be sealed into the cavity, which requires bonding many substrates together and hence increasing device complexity. In Chapter 3, a thermopneumatic microvalve based on this actuation principle will be demonstrated.

Many other actuation mechanisms such as piezoelectric actuation [33], shape memory alloy actuation [34], chemical/biological actuation [35], and magnetostrictive actuation [36] have been demonstrated in the micromachining field. Most actuation mechanisms only satisfy parts of the requirements for an ideal actuator. Therefore, careful consideration must be given when choosing the most suitable actuation mechanism for the desired application.

1.4 Thesis Outline

The object of this thesis is to study a new polymer, Parylene, and its applications for MEMS devices. Parylene is a room-temperature Chemical Vapor Deposition (CVD) deposited polymer and therefore is suitable for post-CMOS integration to combine both MEMS structures and microelectronics on the same substrate. In Chapter 1, we have discussed the simple fabrication steps for micromachined structures and the pros and cons of different actuation mechanisms for MEMS devices. Some of the mechanisms described are suitable to be used with Parylene material while others are not ideal to be integrated with Parylene. This point will be discussed again in the later chapters when the actuation mechanism is chosen for different applications.

The rest of the thesis is divided as follows: Chapter 2 will be the main focus for this thesis; the material properties of Parylene will be examined and studied especially for micromachining applications. Properties including mechanical, electrical, chemical,

thermal, and surface properties will be examined in detail to determine the applications of this material. Chapter 3 begins with the use of low Young's modulus properties of Parylene to make a thermopneumatic microvalve targeted to handle up to 90psi gas pressure with flow rate at slpm range. In the second part of Chapter 3, a silicone O-ring designed to reduce the packaging complexity of microfluidic devices is developed and characterized.

Chapter 4 treats one of the most important difficulties in surface micromachining technology, stiction. Stiction itself remains an interesting problem even for polysilicon surface micromachining. In this chapter, a new sacrificial layer technology that combines wet photoresist dissolution and dry BrF_3 dry etching will be developed and tested. Therefore, large MEMS microstructures using Parylene as mechanical material can be realized. Chapter 5 is devoted to utilize the technology developed in Chapter 4 for electrostatic actuation application with the initial goal of making a surface micromachined microvalve. However, due to the high resistivity of Parylene, several undesired properties that have never been reported in polysilicon are first characterized and understood in this study. Therefore, to use Parylene as a dielectric with air as a medium, the device has to be designed to operate with low electric field regions. A bulk-micromachining electret microphone, which uses Parylene as a back-plate support to enhance the overall yield of the device, is designed and characterized in Chapter 6. Finally, Chapter 7 provides a concluding summary and potential future research on this material.

1.5 References

[1] R. P. Feynman, "There's Plenty of Room at the Bottom," *Journal of Microelectromechanical Systems*, vol.1, pp.60-66, 1992.

[2] K. E. Petersen, "Silicon as a Mechanical Material`," *Proc IEEE*, vol.70, pp.420-457, 1982.

[3] J. M. Giachino and T. J. Miree, "The Challenge of Automotive Sensors," SPIE Conference on Microlithography and Metrology in Micromachining, Austin, TX,1995.

[4] E. V. Bhaskar and J. S. Aden, "Developement of the Thin-Film Structure for the ThinkJet Printhead," *Hewlett-Packard Journal*, vol.36, pp.27-33, 1985.

[5] L. J. Hornbeck, "Digital Light Processing and MEMS: Timely Convergence for a Bright Future," Proceedings of the SPIE Workshop on Micromachining and Microfabrication Processes, Proceedings of the SPIE- The International Society for Optical Engineering, Austin, TX, Oct. 23-24, 1995.

[6] K. Ikuta and K. Hirowatari, "Real Three-dimensional Micro Fabrication Using Stereo Lithography and Metal Molding," Proceedings of IEEE Workshop on Micro Electro Mechanical Systems (MEMS '93), Fort Lauderdale, USA, Febuary, 1993.

[7] T. Masaki, K. Kawata, and T. Masuzawa, "Micro Electro-Discharge Machining and Its Applications," Proceedings of IEEE Workshop on Micro Electro Mechanical Systems (MEMS '90), Napa Valley, USA, Febuary 1990.

[8] D. J. Elliott, *Ultraviolet Laser Technology and Applications.*, San Diego, CA, Academic Press, 1995.

[9] R. C. Anderson, G. J. Bogdan, and R. J. Lipshutz, "Miniaturized Genetic-Analysis System," Technical Digest, Solid-State-Sensors and Actuators Workshop, Hilton Head Island, South Carolina, USA, June 1996.

[10] G. T. A. Kovacs, *Micromachined Transducer Sourcebook*, McGraw-Hill Book Co., 2000.

[11] M. Madou, *Fundamentals of Microfabrication*. Boca Raton, New York, CRC Press, 1997.

[12] S. D. Senturia, *Microsystem Design*, Kluwer Academic Publishers, 2000.

[13] C. T.-C. Nguyen, "Micromechanical Resonators for Oscillators and Filters," Proceedings of the 1995 IEEE International Ultrasonic Symposium, Seattle, WA,1995.

[14] L. S. Fan, Y. C. Tai, and R. S. Muller, "Integrated Movable Micromechanical Structures for Sensors and Actuators," *IEEE Transactions on Electron Devices*, vol. ED-35, pp.724-730, 1988.

[15] C. J. Kim, A. P. Pisano, R. S. Muller, and M. G. Lim, "Polysilicon Microgripper," Technical Digest, IEEE Solid-State Sensors and Actuators Workshop, Hilton Head Island, South Carolina, USA, June 1990.

[16] Y. C. Tai, "IC-Processed Polysilicon Micromechanics: Technology, Materials, and Devices," Ph.D. thesis, University of California, Berkeley, 1989.

[17] N. C. Tien, O. Solgaard, M. H. Kiang, M. Daneman, K. Y. Lau, and R. S. Muller, "Surface-micromachined mirrors for laser-beam positioning," *Sensors and Actuators A*, vol.52, pp.76-80, 1996.

[18] http://www.memsrus.com/cronos/CIMSmain2ie.html

[19] http://www.sandia.gov/mems/micromachine/summit5.html

[20] C. Storment, D. Borkholder, V. Westerlind, J. Suh, N. Maluf, and G. Kovacs, "Dry-Released Porcess for Aluminum Electrostatic Actuators," Technical Digest, Solid State Sensor and Actuator Workshop, Hilton Head Island, South Carolina, USA, June 1994.

[21] T.R. Tsao, T.Y. Hsu, and Y.C. Tai, "Copper Sacrificial Layer Technology for use in surface micromachining," Micromachining Workshop III- Southern California Chapter of American Vacuum Society, Anaheim, CA, September 1996.

[22] J. Q. Liu, Y. C. Tai, J. Lee, K. C. Pong, Y. Zohar, and C. M. Ho, "In Situ Monitoring and Universal Modeling of Sacrificial PSG Etching Using Hydrofluroic Acid," Proceedings of IEEE Workshop on MicroElectroMechanical Systems (MEMS '93), Fort Lauderdale, USA, Feburary 1993.

[23] W. H. Ko, J. T. Suminto, and G. J. Yeh, "Bonding Techniques for Microsensors," in *Micromachining and Micropackaging of Transducers*, Amsterdam, Elsevier Science Publishers B.V.,1985.

[24] K. Peterson, P. Barth, J. Poydock, J. Brown, J. M. Jr., and J. Bryzek, "Silicon Fusion Bonding for Pressure Sensors," Technical Digest, IEEE Solid State Sensors and Actuators Workshop, Hilton Head Island, South Carolina, USA, June 1988.

[25] http://dvorak.mse.vt.edu/faculty/hendricks/mse4206/projects98/group09/ moregear.htm

[26] T. Akiyama, "Controlled Stepwise Motion in Polysilicon Microstructures," *Journal of Microelectromechanical Systems*, vol.2, pp.106-110, 1993.

[27] R. A. Miller and Y. C. Tai, "Micromachined electromagnetic scanning mirrors," *Optical Engineering*, vol. 36, pp.1939-1407, 1997.

[28] M. Ataka, A. Omodaka, N. Takeshima, and H. Fujita, "Fabrication and Operation of Polyimide Bimorph Actuators for a Ciliary Motion System," *Journal of Microelectromechanical Systems*, vol. 2, pp.146-150, 1993.

[29] M. F. Pai and N. C. Tien, "Low voltage electrothermal vibromotor for silicon optical bench applications," *Sensors and Actuators A*, vol. 83, pp.237-243, 2000.

[30] http://mems.colorado.edu/c1.gen.prjct/DARPA_mems/

[31] C. Grosjean and Y. C. Tai, "A thermopneumatic Peristaltic Micropump," 1999 International Conference on Solid-State Sensors and Actuators (Transducers '99), Sendai, Japan, 1999.

[32] X. Yang, "Micromachined Silicone Rubber Membrane Valves for Fluidic Applications," Ph.D thesis, California Institute of Technology, 1999.

[33] S. Akamine, T. R. Albrecht, M. J. Zdeblick, and C. F. Quate, "A Planar Process for Microfabrication of a Scanning Tunneling Microscope," *Sensors and Actuators A*, vol. 23, pp. 964-970, Apr. 1990.

[34] P. A. Krulevitch, A. P. Lee, P. B. Ramsey, J. C. Trevino, J. Hamilton, and M. A. Northrup, "Thin Film Shape Memory Alloy Microactuators," *Journal of Microelectromechanical Systems*, vol. 5, pp. 270-282, Dec. 1996.

[35] E. Smela, O. Inganas, and I. Lundrstrom, "Self-Opening and Closing Boxes and Other Micromachined Folding Structures," 1995 International Conference on Solid-State Sensors and Actuators (Transducers '95), Stockholm, Sweden,1995.

[36] E. Quandt, A. Ludwig, and K. Seemann, "Giant Magnetostrictive Multilayers for Thin-Film Actuators," 1997 International Conference on Solid-State Sensors and Actuators (Transducers '97), Chicago, IL, 1997.

CHAPTER 2

Parylene as a MEMS Material

Abstract

In this chapter, the properties of Parylene as a MEMS material will be studied. First, the rationale in investigating Parylene as a material for possible applications in MEMS will be given. Then, the electrical, thermal, surface, and mechanical properties will be studied and compared with that of other materials. The possible actuation mechanism inferred from the material properties will also be discussed.

2.1 Backgrounds

Parylene is the generic name for members of a unique family of thermoplastic polymers that are deposited by using the dimer of para-xylyene (di-para-xylylene, or DPXN) [1]. Parylene coating processes were originally developed in the 1950s by William F. Gorham and then commercialized by the Union Carbide Corporation in 1956 [2]. Parylene is widely used for coating of electronic components, medical instruments, and has recently been explored to be used as interlayer dielectrics (ILD) in the microelectronics industry [2]. The main reason for studying Parylene material to be used in MEMS applications lies in its unique conformal room-temperature-CVD-deposited characteristics.

2.1.1 Integration with MEMS and Electronics

Putting signal-conditioning electronics with sensors on the same substrate would greatly reduce the noise and cost of the device, thereby enhancing performance. One of the key benefits of MEMS devices is the mass-producible characteristic inherited from IC microelectronics processes. However, putting MEMS structures together with standard electronics is not easy because the metal used in interconnection for electronics (i.e. usually aluminum) has a low melting point. This poses an issue for some typical surface micromachining processes in which the required processing temperature is higher than 500°C (see Table 2-1). Therefore, the micromachining steps have to be done before the metallization can occur, or else the metal will not survive. This approach requires the tuning of CMOS IC processes usually done in the foundry. Due to contamination issues, foundries seldom allow pre-processed wafers to come into the production lines. This limits the chance of integration using pre-IC processing methods. However, several successful devices have been demonstrated to integrate MEMS structures with electronics by modifying microelectronics IC processes. For example, Fig. 1-3(c) shows the ADXL-150 from an analog device that was fabricated using its modified BiCMOS processes.

Therefore, aluminum metallization had been replaced with tungsten (W) [3] to avoid a low melting point and to achieve integration of MEMS with CMOS [3]. However, the tungsten reacts with silicon at temperatures higher than 600°C, and therefore requires an extra diffusion barrier. In addition, the heavily doped structural and sacrificial layers also affect the finely tuned CMOS processes.

In order to easily avoid the pre-IC problem and the integration of microstructures with electronics, the post-CMOS approach is usually adapted. In this approach, no single

step in the processes requires temperatures higher than 450°C, thus avoiding the aluminum melting and associated sintering problem. Several materials have been used (i.e., polyimide, metal (aluminum, copper) and Plama Enhanced Chemical Vapor Deposition (PECVD) material) to demonstrate post-CMOS microstructures. The central theme of this thesis is to study and develop micromachining processes for the Parylene polymer, which requires temperature less than 100°C.

Table 2-1: Critical Temperatures for Surface Micromachining

Materials	Temperature (°C)
LPCVD Nitride	800
LPCVD doped Polysilicon	650
LPCVD low stress Polysilicon	610
LPCVD LTO/PSG	450
Annealing of PSG (for densification)	950
Annealing of Polysilicon (for reducing stress)	1050

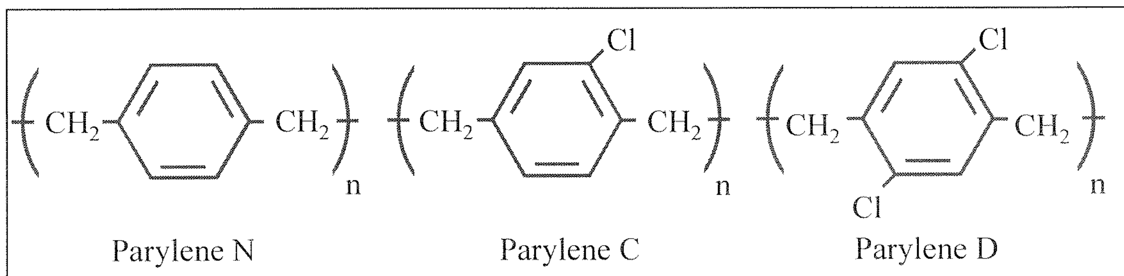

Fig. 2-1: Chemical structures of Parylene [1]

As shown in Fig. 2-1 [1], there are three different kinds of Parylene commercially available on the market [2]. Parylene N is poly-para-xylylene, a completely linear and highly crystalline polymer. Parylene C, which is the main focus of study in this thesis, is basically Parylene N with a chlorine atom replacing one of the aromatic hydrogens.

Parylene D is similar to Parylene C but with two aromatic hydrogens being replaced with chlorine atoms. In the next section, the deposition system of Parylene will be described to reveal its room temperature deposited characteristics.

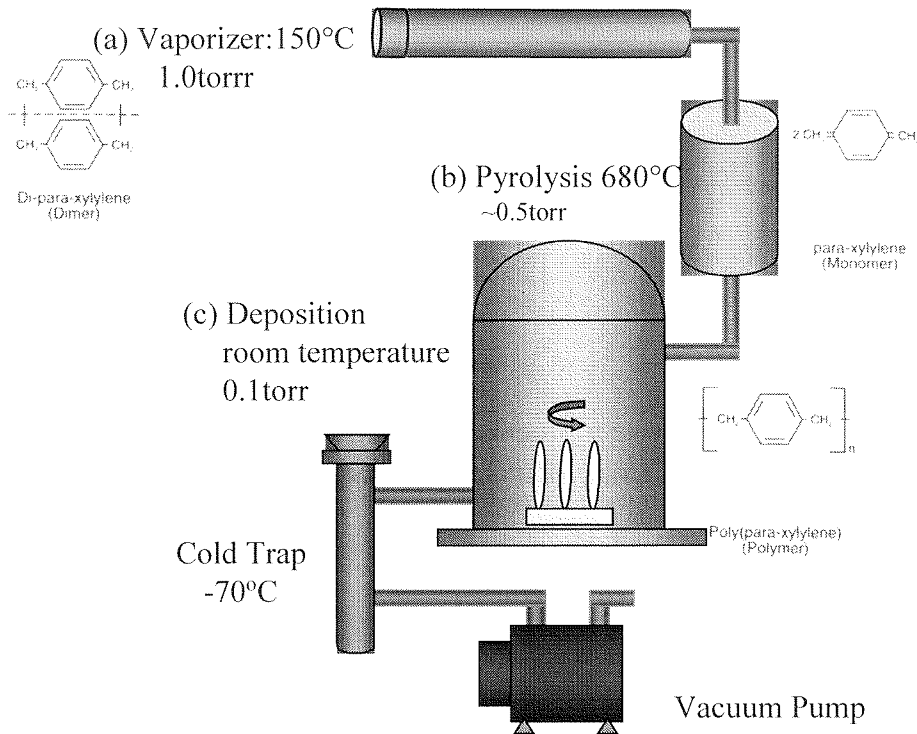

Fig. 2-2: Parylene deposition systems [1]

2.1.2 Parylene Deposition Processes

Shown in Fig. 2-2 [1, 2] is the deposition system of Parylene from Special Coating Systems Inc., model PDS 2010 Labcoater 1, which is the system [1] used for all the Parylene deposition in this study. Parylene is deposited at room temperature around 0.1 torr where the mean free path of the molecules is on the order of 0.1cm. Therefore, the deposited Parylene is conformal within the critical size ranges that we are concerned.

The first step of the deposition process is the vaporization of the solid dimer at approximately 150°C. The second step is the pyrolysis of the dimer at about 680°C, in which the dimer is cleaved at the two methylene-methylene bonds to yield the stable monomeric diradicals, para-xylylene. Finally, the monomers enter the deposition chamber at room temperature where they simultaneously adsorbs and polymerizes on the substrate. The cold trap at approximately -70°C is used to collect the un-reacted monomers before they enter the mechanical pump.

2.1.3 Pattern Parylene using Oxygen Plasma

Although Parylene can be deposited selectively using heated resistors to create local heating [4, 5], Parylene, like most materials, is best patterned with positive photoresist and plasma etching. Because Parylene is CVD-conformal deposited, using the lift-off process to pattern the Parylene is difficult. Therefore, positive photoresist is used for patterning in most cases. Oxygen plasma is often selected as an etchant for most polymer materials because it reacts with the polymer in plasma, thereby decomposing it into gas phase products such as carbon monoxide and carbon dioxide.

Other masking materials are also used in place of photoresists to etch Parylene in oxygen plasma. The selectivity of oxygen plasma between photoresist and Parylene is low, often in the 1:1 range, because the photoresist itself is a polymer. Other metals and even polysilicon (i.e., sputtered amphorous silicon) have been explored as potential etching masks. However, the most important criteria for selecting a mask material is the adhesion between the etch mask and the material itself. Adhesion of photoresist and Parylene is excellent because they are both polymers, whereas some metals such as

evaporated aluminum do not demonstrate good adhesion with Parylene and therefore have to be used with great care. Table 2-2 shows the adhesion between different materials and Parylene, which can be used as a guideline to choose the mask material for Parylene etching. A-174 is the adhesion promoter suggested by the manufacturers in order to enhance the adhesion between the Parylene film and the substrate. The chemistry of the adhesion promoter will be discussed in the later sections.

Table 2-2: Adhesion of the materials on Parylene

Material	Adhesion of Material on Parylene-C	Adhesion of Parylene-C on material
Evaporated Aluminum	Poor	Good with A-174
Evaporated Gold	Good	Poor
Evaporated Chromium	Good	Good with A-174
Sputtered Silicon	Often cracked without pre-annealing the Parylene at high temperature	Good with A-174
Single Crystal Silicon	N/A	Good with A-174
Thermal Silicon Dioxide	N/A	Good with A-174
Sputtered Silicon Dioxide	Often cracked without pre-annealing the Parylene at high temperature	Good with A-174
LPCVD Silicon Nitride	N/A	Good with A-174

It has been experimentally determined that a short O_2 plasma treatment (200 mtorr, 200W, 1minute) between successive Parylene depositions enhances the adhesion between different Parylene layers. It has also been found that the same O_2 plasma helps to improve the adhesion between photoresist and Parylene.

2.1.4 Substrate Preparation prior to the deposition

Applying an organic coupling agent, the "adhesion promoter," prior to polymer deposition usually couples the polymers to the silica surface. Commercially used coupling agents can be categorized into three different chemical mechanisms; chlorosilanes, alkyltrichlorosilanes and alkoxysilanes [6, 7]. Chlorosilanes are more reactive to nucleophilic substitution than alkoxysilanes and therefore are used as coupling agents when only a single point of attachment is required or when well-defined materials must be prepared.

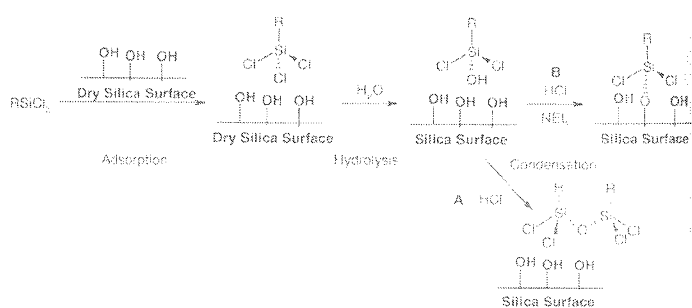

Fig. 2-3: Coupling schemes of alkyltrichlorosilanes

Alkyltrichlorosilanes do not react directly with an anhydrous silica surface below 300°C except trichlorosilane. However, when diluted in organic solvents in the presence of surface water, they begin to hydrolyze to RCl_2SiOH groups and begin to condense, particularly in the presence of the HCl catalyst formed in the process. With excess surface water, the majority of the hydrolysis and condensation reactions occur at the solid/water interface, leading to crosslinked siloxanes not bound to the surface, as shown in step A in Fig. 2-3. However, in the presence of base and irrespective of the other ligands on silicon, condensation rapidly occurs with the surface as shown in step B in Fig. 2-3.

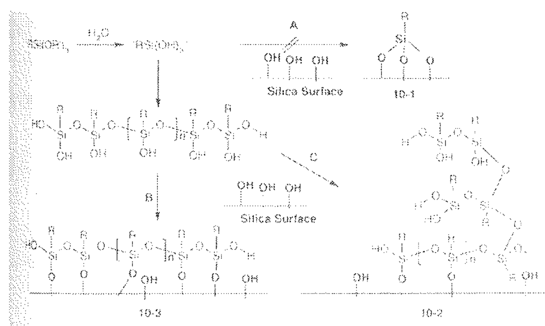

Fig. 2-4: Coupling schemes of alkoxysilanes

Trifunctional silanes are generally preferred in surface modification reactions as they form a crosslinking network on and likely *with* the surface. Although it is usually drawn as in diagram A in Fig. 2-4 with three covalent bonds, this is not a true picture of chemical coupling. With water as the reaction solvent, monolayer coverage of the surface is not generally observed. Instead, ill-defined multilayer systems result from the reaction of coupling agents with silica surfaces as shown in step C of Fig. 2-4, especially with activating organic groups on the alkoxysilane, such as aminopropyl.

Shown in Fig. 2-5 are some commercially available coupling agents. Many different functional groups including carbinols, thiols, carboxylic acids, sulfonic acid derivatives, and phosphates have been incorporated. Functional surface groups may also contain organic residues (e.g., CH_2=CH_2, styryl, methacryl, etc.) that can undergo radical copolymerization with organic monomers such as Parylene, or hydrosilylation with silicones, to give stable, reinforced composites. The adhesion promoter used for Parylene adhesion is A-174 that contains the coupling agent gamma-Methacryloxypropl-trimethoxysilane (shown in Fig. 2-5), which is one of the alkoxysilanes discussed in the previous section. In most applications, the surface has to be adhesion promoted with A-174; otherwise, the interface between Parylene and the substrate will be too weak to even pass the dicing steps. Some other ways such as roughening the silicon surface with

bromine trifluoride (BrF_3) have been proposed [8]. Nonetheless, applying the adhesion promoter is straightforward and therefore is always used to couple the first Parylene layer to substrate in the study.

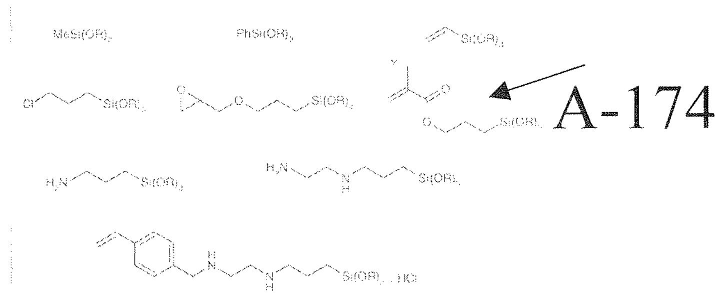

Fig. 2-5: Some commercially available coupling agents

The procedures of substrate preparation prior to the deposition can be described as follows. First, the adhesion promoter is prepared in 0.5% A-174/IPA/DI H_20 solution, (i.e., 2.5 ml A-174 silane, 250 ml IPA, and 250ml DI H_20). The manufacturer suggests that the adhesion promoter be mixed and put aside for two hours prior to applying it to the substrate to ensure full mixing of the solution. The solution should be discarded after 24 hours, because most of the coupling agents internally react with themselves after prolonged periods. After two hours, wafers are immersed into the adhesion promoter for 15-30 minutes and then air-dried for 15-30 minutes to ensure full reaction on the surface. IPA is then used to rinse the substrate for 15 seconds to get rid of the adhesion promoter residue that has not reacted with the surface. Finally, the substrate should be air-dried to prevent any residual solvents from remaining on the surface.

In this section, we have described the general cycles of Parylene processing (see Fig. 2-6)[1]. All the processes described here only require room temperature operation. The only high temperature step is photoresist-baking process, which can be significantly lowered if application demands.

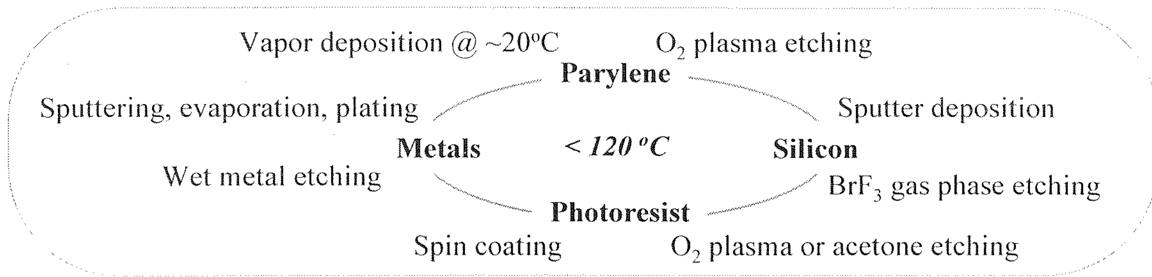

Fig. 2-6: Low temperature Parylene process (from [1])

In the following sections, the properties of Parylene for MEMS applications will be explored, and several basic Parylene structures will be built to investigate the different properties of Parylene.

2.2 Basic Parylene Properties

Although the basic data of Parylene material properties are given from the manufacturers (see Table 2-3)[2], several important properties have to be understood fully in order to build a MEMS microstructure. For example, the dielectric strength provided in the data is usually measured in thick film, which may differ significantly from our thin film applications. Furthermore, the surface energy of Parylene, which is important for many microfluidic applications, is not included in the data.

The manufacturers' data reveal that Parylene has very high electrical resistivity, which is important for electrical insulation, and low dielectric constant, which is also important for interdielectric layer applications to reduce the RC delay. The low Young's modulus (2.5-2.7 GPa) of Parylene compared to single crystal silicon (170GPa) provides an alternative material selection for MEMS applications. With an elongation to break

percentage of more than 200% makes it a perfect membrane material for large deflection applications.

It is believed that Parylene is bio-compatible and therefore has the potential to be implanted into the human body. For example, Parylene has been used for cochlear implantation [9] and gel electrophoresis [10], as well as PCR reactions [11] where DNA has been successfully amplified in Parylene coated microvials. Therefore, it is important to understand fully the fundamental Parylene properties for various MEMS applications.

Table2-3: Parylene Properties

	Parylene N	Parylene C	Parylene D
Dielectric Strength (V/μm)	275	220	220
Dielectric Constant	2.6	3.1	2.8
Young's Modulus (GPa)	2.5	2.8	2.7
Yield Strength (MPa)	42	55	62
Elongation to Break (%)	20-250	200	10
Density (g/cm3)	1.10-1.12	1.29	1.42
Index of Refraction	1.66	1.64	1.67
Melting Point (°C)	420	290	380
Glass Transition (°C)	>300	240	240
Linear Coef. Of Expan. /°C	6.9×10^{-5}	3.5×10^{-5}	$3\text{-}8 \times 10^{-5}$
Specific Heat at 20°C (cal/g°C)	0.20	0.17	-
Thermal Conductivity at 20°C (cal/cm°Cs)	3.0×10^{-4}	2.0×10^{-4}	-

2.3 Electrical Properties of Parylene

In this section, the dielectric strength of thin-film Parylene will be determined. This parameter determines the maximum voltage that can be applied on the Parylene material or MEMS microstructures based on Parylene. The charge retention capability of the Parylene film will also be determined. Insulators with high resistivity such as Teflon™ (PTFE) or even Parylene usually have good charge retention capability. Some of them can hold the stable charge for a long time (PTFE could hold charge longer than hundred years), while some of them can only hold the charge temporarily (lousy PECVD oxide could only hold charge for several minutes). Observations discussed here will be used in Chapter 5 to study the interesting phenomena found in electrostatic actuators made of Parylene.

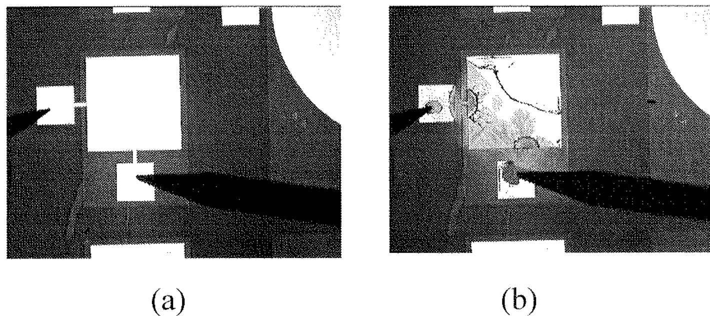

(a) (b)

Fig. 2-7: Parallel capcitor with Parylene dielectrics
(a) Photo of parallel capacitor prior to apply voltage
(b) Photo of the capacitor after breakdown

2.3.1 Dielectric Strength of Thin-Film Parylene

Insulating polymers have been used widely as electrical insulating materials. However, the high-field phenomena of insulating polymers like Parylene are very complicated because of their chemical and physical structures and because of the various additives or impurities in the polymers. In addition, space charge is known to affect electrical conduction and breakdown of insulating materials[12] with mechanisms that

are not yet well understood. In this section, the breakdown dielectric strength of Parylene thin film will be investigated to further understand the role of electric conduction inside Parylene film.

As shown in Fig. 2-7, the dielectric strength is investigated using the parallel capacitor method [12]. The process flow for parallel capacitors starts with 4''quartz wafers. The first layer of Cr/Au electrodes are then thermally evaporated and patterned. Different thicknesses of Parylene thin film (0.8μm and 1.8μm) are then deposited at room temperature. Then, the top Cr/Au electrodes are thermally evaporated and patterned for the top electrodes. Finally, Parylene is patterned with oxygen plasma to define the electrode shapes.

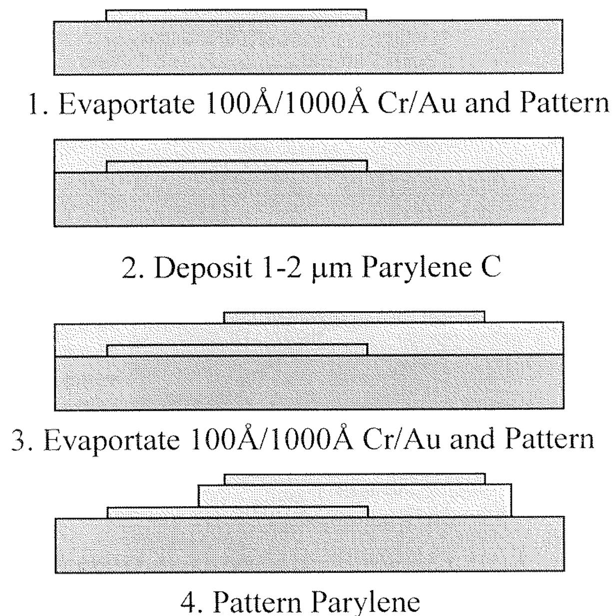

Fig. 2-8: Simplified process flow of parallel capacitors

The experimental setup for measuring current-voltage relationship is shown in Fig. 2-9; the current-voltage relationship of a pair of capacitors with similar geometrical shape is shown in the following Fig. 2-10. It's clear that the electrical behavior of the Parylene

thin film is like a resistor with high resitivity at low electric fields. However, at high electric field (around 2.5MV/cm), the conduction current increases drastically and the material starts to breakdown. These results seem to correlate with the manufacturer's data well. The data here is also consistent with those described in [13].

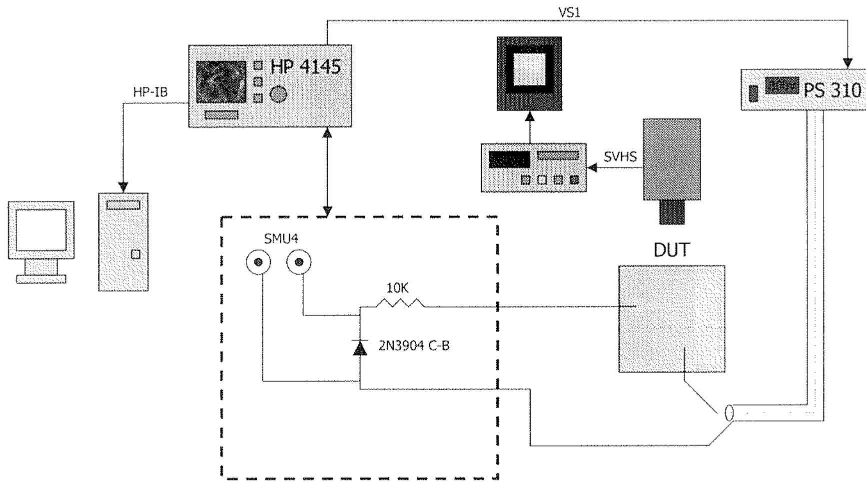

Fig. 2-9: Experimental setup for measuring I-V curve with current limiter

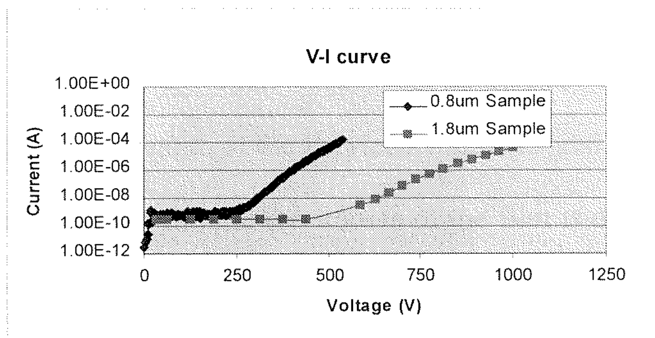

Fig. 2-10: Voltage-Current relationship of a Parylene dielectric capacitor prior to breakdown

The breakdown of Parylene thin film was also investigated by several other groups because of its potential use in integrated circuit passivation or as interlayer dielectrics (ILD). Other findings are consistent with the results shown here in that the

breakdown has a negative temperature dependence and positive film-thickness dependence to the breakdown voltage. Some authors also point out that the breakdown is further accompanied by electroluminescence possibly due to collision ionization (electron avalance) [13] (see Fig. 2-11). Also, the breakdown in Fig. 2-11 starts from the edge of the capacitor where the sharp edge increases the local electric field.

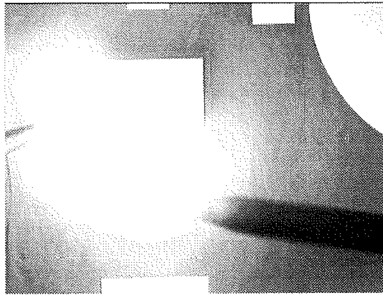

Fig. 2-11: The breakdown moment of Parylene film

Several other groups have also looked into the possible mechanisms of breakdown in Parylene thin film because of its simple chemical structure and the purity of its deposition (no additives). The majority of them conclude that it is the space charge inside the Parylene thin film during high field conduction that is causing the breakdown. In this section, the breakdown strength of the Parylene was measured and characterized to be 2.5MV/cm. The survey shows that the breakdown of the film is directly related to the space-charge accumulated inside the thin-film at high field conduction. In the next section, the charge retention capability of the Parylene film will be studied to provide a more complete picture of charges in Parylene.

2.3.2 Charge retention capabilities of Parylene thin-film

Many methods of charging dielectrics have been developed in the past for electret applications such as triboelectric charging [14], isothermal charging [15], liquid contact charging [16], partially penetrating electron and ion beams charging, and penetrating radiation charging [15, 17, 18]. In this section, the charge retention capability of Parylene thin film is studied to understand the significance of the charging effect and the strange phenomena in Parylene electrostatic actuators. Moreover, the behavior of the Parylene microstructure in a SEM (scanning electron microscope) will also be investigated later in Chapter 5 as another demonstration of charging effect on Parylene dielectrics.

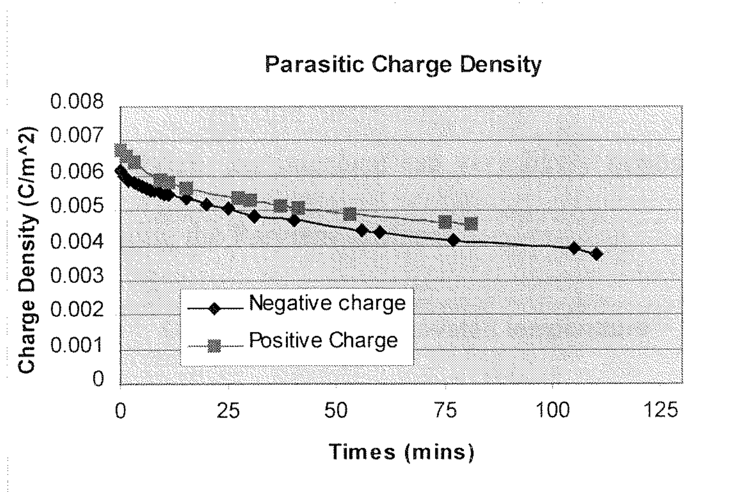

Fig. 2-12: The positive and negative charge density deposited on Parylene surface using Zerostat gun

In this section, the charge retention capability of Parylene thin film will be examined. The charge source will be provided by two methods. One is Zerostat3 gun, a piezoelectric device which generates high voltage and thus breaks down the air surrounding it. Then, positive or negative ions can be deposited onto the desired surfaces. The advantage of using this apparatus is that the polarities of the ions can be controlled, and that the apparatus is relatively small (hand-held size). We also investigated this

problem using the Back Light Thyratron [19], which can only deposit negative electrons onto surfaces.

The test sample starts with a highly-doped SCS (single-crystal silicon) followed by the careful removal of the native oxide grown on top. Then, 100Å-Cr/2000Å-Au is thermally deposited on the bottom, serving as the electrodes. Next, 3-4μm of Parylene thin-film is room temperature deposited on top. The wafers are then diced for testing.

Fig. 2-12 shows the charge density on the Parylene samples fabricated using the previously described method. Here, the charge deposition method is performed using the Zerostat gun. It is clear that Parylene holds a tremendous amount of charge for an extended period of time. The charge density can be as high as $7*10^{-3}C/m^2$, which causes the surface potential of Parylene to be several hundred volts. Because of this, any current flowing through the Parylene-air interface can very likely deposit ions/electrons on the surface, therefore charging the Parylene surfaces.

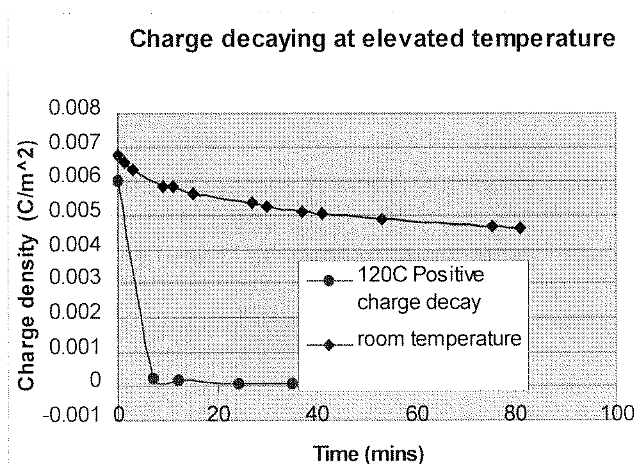

Fig. 2-13: The positive charge decaying at room temperature and elevated temperatures.

From Fig. 2-12, it is also clear that the Parylene thin film can not only hold negative ions but also positive ions as well. This phenomenon is interesting because the

Teflon samples that will be investigated in Chapter 6 can only hold negative charges. Thus, the BLT as will be described in Chapter 6 is also used here to see if Parylene can also hold electrons. However, the Parylene tested here failed to hold any significant amount of charge under BLT irradiation. The charge measurement was done by Morone isoprobe, which uses a charge compensation method that will be discussed in Chapter 6.

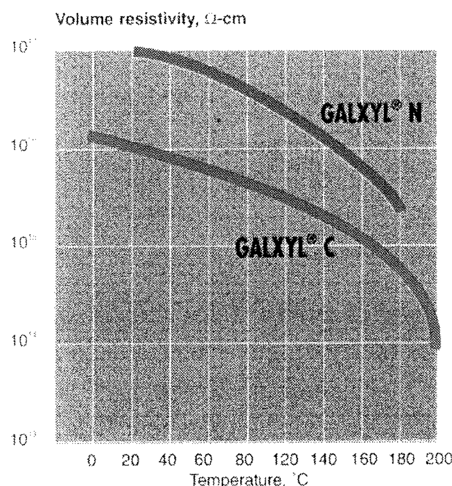

Fig. 2-14: The volume resitivity of Parylene decreases at elevated temperatures

As shown in Fig. 2-13, charges on Parylene thin film are very temperature sensitive and diminish in short amounts of time (a few minutes at 120°C). Like most of the electret, this phenomena may be due to various reasons, but likely results from the lowering of the potential barrier and the ease of carrier movement. Even more simply put, the conductivity of Parylene drops significantly at elevated temperatures as shown in the following curves of Fig. 2-14 [20].

2.4 Mechanical Properties of Parylene

For micromachining applications, the mechanical properties of the desired material are important. Parameters such as Young's modulus, yield strength, and elongation to break will determine or constrain the material's applications. Moreover, the residual stresses in the film after deposition is also important to prevent undesired curving or buckling as shown in Fig. 2-15 [21]. In this section, the existing measurement methods for the residual stress of thin-film Parylene will be examined to determine the best method to measure Parylene stress. Parylene residual stresses will then be measured using surface micromachined techniques. The Young's modulus will be confirmed at the same time using bulge-testing method and will be compared against the manufacturer's data.

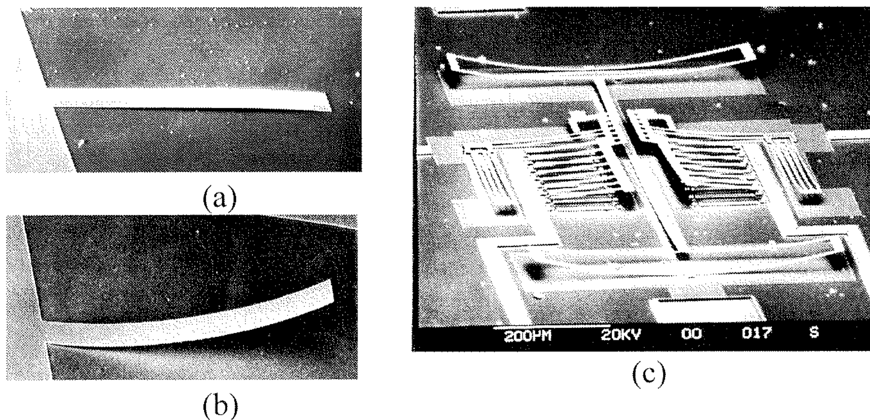

Fig. 2-15: The effect of the bad stress control
(a) More tensile on the bottom (bending down)
(b) More tensile on the top (curved up)
(c) Bad day at MCNC polysilicon processes

2.4.1 Stresses in thin-film

The latest developments of micromachining fabrication have benefited dramatically from the understanding of residual stress of thin film materials. For most micromachining applications, the film thickness is on the order of a few microns. At this

size range, a slightly tensile residual stress is preferred. Many problems of fabrication are either directly or indirectly linked to the stress such as film cracking, de-lamination, and void formation. Even more, compressive stresses can cause severe buckling in the clamped structures, which in turn damage the devices. A large residual tensile stress drastically reduces the sensitivity of membrane-based sensors such as microphones and pressure sensors. Furthermore, the stress gradient inside the stress-released microstructures can cause undesired curvature bending and often make the structure unusable. Thus, to fully optimize the performance of the MEMS sensors and actuators, a thorough understanding of the residual stress is required.

The stress-causing factors can be categorized as either intrinsic or extrinsic [3]. The intrinsic stress (also growth stress) develops during film nucleation, while extrinsic stress is caused by unintended factors such as temperature gradients or package-induced stress. Thermal stresses, which is the most understood extrinsic stress type, are caused by structures with inhomogeneous thermal expansion coefficients that are subjected to a uniform temperature change or in a homogeneous material that is exposed to a thermal gradient. Although intrinsic stress is often much larger than extrinsic stresses in most LPCVD-deposited materials, stresses in CVD-deposited Parylene are mainly caused by extrinsic factors (i.e., thermal mismatch).

The next two sections will focus on stress measurement. Section 2.4.2 discusses the advantages and disadvantages of methods to measure the stresses in thin films. It will also discuss how to apply the existing methods to our Parylene systems. Section 2.4.3 will first be devoted to measurement of stress of Parylene thin films, especially the

residual stresses at different annealing temperatures. The origin of stresses in the Parylene thin-films will be also explored.

2.4.2 Comparison of Stress Measurement Methods

When a structure under stress is released by removing the underlying layer, the stress is subsequently relieved by a change of dimensions of the structure. Because this change is intrinsically small, some amplification mechanisms are required to transform the dimension change to a larger displacement for easier readout. Several methods have been developed in the past to measure thin-film stresses. They generally fall in two categories: (1) displacement and (2) resonance frequency [22].

Resonance Methods

As the name implies, this method is based on measuring the change in resonance frequency that is caused by the change in structural dimensions by stresses of thin-films. This measurement method inherently requires complicated, supplementary instruments not readily available in many laboratories to measure the resonance change. The method can be roughly divided into (1) bridge type and (2) cantilever type.

For bridge type measurements, a doubly-supported bridge structure is fabricated using either bulk or surface micromachining techniques. The resonance frequency ω of this bridge would shift due to the stress. For the cantilever type, the stress is not related to the resonance frequency because the stress is already released at the free end. However, it is possible to measure the resonance change through the change in structural dimensions.

Because of the inherent process variability, the dimensions of the structure have to be measured prior to the release steps, which complicates the stress measurement.

Therefore, in order to use the resonance method to measure thin-film stress, the equipment first has to be able to measure the small change in resonance. Second, because most of the resonance frequency measurements involve a laser vibrometer, the device has to be inherently large enough to allow the instrument to pick up the signal from the devices. The surface of the device also has to have reasonable reflectivity. Third, because air damping underneath the structures significantly shifts the resonance frequency to a lower value, the measurement either has to be able to compensate for the error, or the measurement has to be done in a vacuum environment, presenting another complication to the measurement. Therefore, the resonance frequency method is not used in this study when measuring the stresses in thin film Parylene.

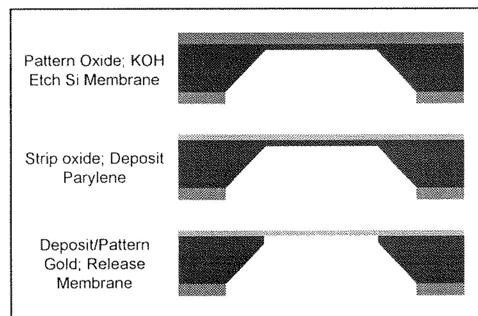

Fig. 2-16: The method for making freestanding Parylen membrane for bulge test

Displacement Methods

The displacement method can be divided as (1) wafer warpage measurement, (2) bulge measurement, (3) in-plane T/H structures, (4) in-plane bridge/Guckle ring type and, (5) in-plane rotation tip type.

Wafer Warpage

For wafer warpage methods, the overall wafer curvature before and after deposition are measured and the stresses are calculated from Stoney's equation[23]:

$$\sigma_f = E_s \frac{t_s^2}{6(1-\nu_s)t_f R_c}$$

σ_f : residual stress in thin film

E_s : Young's modulus of the substrate

ν_s : Possion's ratio of the substrate, 0.25 is often assumed (2.1)

R_c : change of the radius

t_f : film thickness

t_s : substrate thickness

This method is good for measuring both tensile and compressive stresses. A special instrument is needed to measure the curvature of the wafers, and only the average stress of the whole wafer is measured. The resolution of this method is approximately 5MPa and thus is not good enough for our Parylene measurement which has a stress range of around 20MPa.

Bulge Measurement

The bulge measurement is usually done by bulk micromachining to make a thin suspended diaphragm. Fig. 2-16 [24] shows the typical fabrication steps for making a Parylene freestanding membrane. A pressure differential is applied to create the diaphragm displacement. The maximum vertical displacement h at the center of the diaphragm can be related to the applied pressure by the following expression [25]:

$$P = \frac{C_1 \sigma t h}{a^2} + \frac{C_2 E t h^3}{a^4} \qquad (2.2)$$

$$C_1 = \frac{\pi^4(1+n^2)}{64}$$

$$C_2 = \frac{\pi^6}{32(1-\nu^6)}\{\frac{9+2n^2+9n^4}{256} - \frac{[4+n+n^2+4n^3-3n\nu(1+n)]^2}{2[81\pi^2(1+n^2)+128n+\nu(128-9\pi^2(1+n^2))]}\} \quad (2.3)$$

P: applied pressure
E:Young's modulus of the membrane material
σ:residual stress in the membrane
ν: Possion's ratio of the membrane material
t: thickness of the membrane
h: deflection of the membrane
n:a/b (1 for square membrane)

For a square membrane, C_1 and C_2 are 3.04 and 1.83 respectively. The above relationship is nonlinear, so a significant amount of data has to be collected at a low-pressure range with good accuracy in order to get good stress measurements. Although this approach collects data for the Young's modulus and stresses simultaneously, the data collection is rather time consuming. A typical load-deflection curve is shown in Fig. 2-17 while the displacement is measured by a WYKO interferometer (white light interferometry). Furthermore, this method is only good for measuring tensile stresses. Compressive stresses will buckle the membrane and thus make the method inapplicable. The measured Young's modulus from Fig. 2-17[24] is around 4.5GPa, which deviates significantly from the manufacturers' 2.8GPa. Therefore, 4.5GPa should be used for designing mechanical structures using Parylene-C.

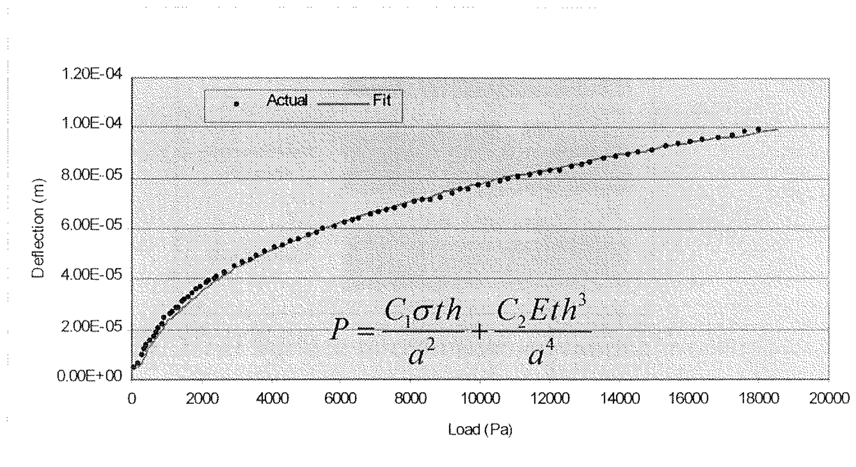

Fig. 2-17: Typical Load-Deflection curve for Parylene membrane

This time-consuming process is not used in this section to measure the stress inside the Parylene thin film. However, the load-deflection method will be used again in section 3.2 to measure the effective stress and Young's modulus of the composite silicone/Parylene membrane.

T/H In-plane structures

Bulk micromachining is usually used to make T/H structures. However, due to the lack of precision alignment between the front and back side of the wafer, significant dimension errors can happen, causing the measurement to be inaccurate. Here, a surface micromachine process is developed to make surface micromachine in-plane strain gauges. This technique will be used in this section to fabricate all the in-plane strain gauges, including T/H structures, Guckle ring/bridge structures and rotation tips.

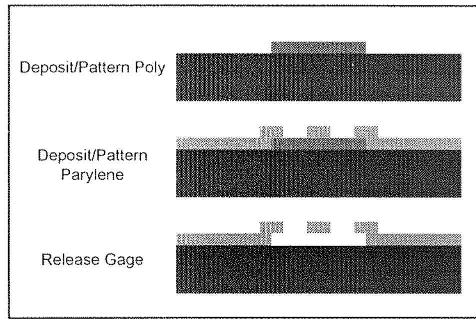

Fig. 2-18: Surface micromachined fabrication steps for In-plane strain gauge

The process flow as shown in Fig. 2-18 starts with 4" silicon wafers with 1μm thermal oxide. The oxide layer is used to protect the silicon substrate from subsequent BrF_3 etching. Then, 2μm LPCVD polysilicon layer is deposited and patterned as the sacrificial layer. Next, a 3μm Parylene C layer is CVD-deposited and patterned to define the shape of the strain gauges. Finally, the devices are diced and the sacrificial polysilicon etched away by BrF_3 etching.

The T structure uses the big pull bar to generate the deflection on the thin beam connected to it and the H structure uses a big plate to pull four thin beams connected to it. Thus, it is clear that both methods are only good for tensile stresses. The compressive stresses may cause the beam to buckle and become futile. The finished T/H structures with unfinished polysilicon etching underneath the Parylene is shown in Fig. 2-19. Because of the inherently small displacement generated by the stresses, the test structure has to be large enough (>mm) to measure the desired stress range. This creates another problem for fabrication; the release of the 2μm polysilicon using BrF_3 has a very slow undercut rate and thus it takes many cycles of BrF_3 etching to free the Parylene structures. However, the selectivity of polysilicon and Parylene is not indefinite under BrF_3. The Parylene structure will finally get damaged and change the surface morphology.

Therefore, the T and H structures are not used to measure the Parylene stress for our study.

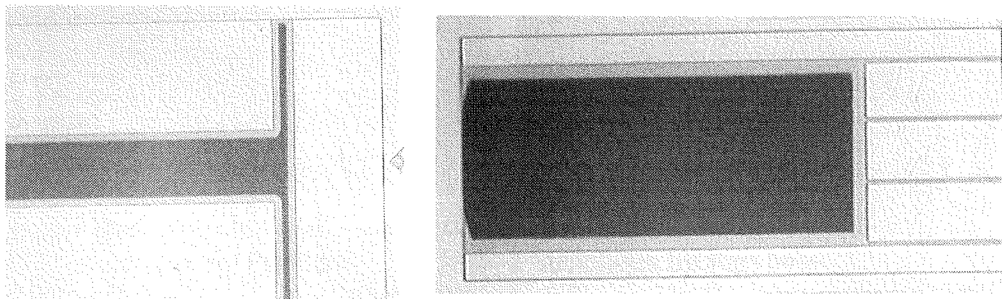

Fig. 2-19: Unfinished T(a),H(b) structures for In-plane strain gauge due to the undercutting capability of BrF_3 vapor phase etching

Guckle Rings

For the Guckle ring structure shown at Fig. 2-20, residual tensile stresses are transformed into compressive stresses for the beam inside the ring, making this method only good for measuring tensile stresses. If the residual stress of the film exceeds a critical value, the beam would buckle. This value depends on the boundary condition of the supports and often does not have an analytical solution.

Thus to make a precise measurement, an array of Guckle rings is needed, sacrificing a large area of the dies. For Parylene measurement, all the Guckle rings under test are all buckled, implying that smaller rings (diameter less than 10μm) are required. This poses a real difficulty for the lithography step available to the lab. Therefore, this method is not employed here but only indirectly used to confirm the stress range measured by rotation tips.

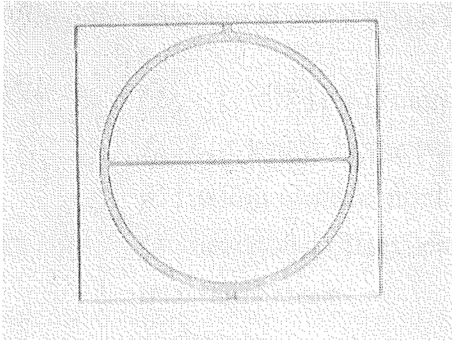

Fig. 2-20: Photos of Guckle ring structures by Parylene

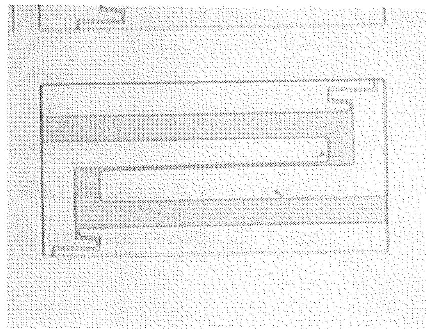

Fig. 2-21: Photos of push-pull structures by Parylene

Push-Pull Structures

Shown in Fig. 2-21 is an idea similar to the Guckel ring, the push-pull structure. It suffers similar problems as the Guckel ring structures and so will not be discussed here.

Rotation Tips

For the rotation tips technique, the strain of the thin film is converted into the torque by rotating the strain gauges. This method is good for compressive stresses and tensile stresses. Since this method does not involve finding critical structures, it does not require the use of an array of devices, so only very small area is needed. This method is used to measure the stress in Parylene for this study. The mathematical model is described in detail as follows.

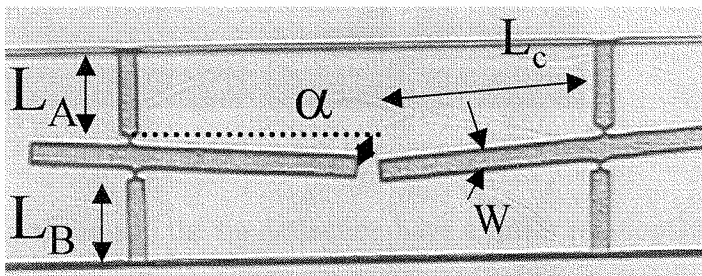

Fig. 2-22: Geometry of the rotating tips for measuring Parylene stress

When the structure is under strain ε, the rotated angle α can be expressed as

$$\begin{aligned} &(L_A + L_B + W)\varepsilon = O\tan(\alpha) \\ &L_A, L_B: \text{ length of the two roatation beams} \\ &W: \text{ width of the central-rotated beam} \\ &O: \text{ horiztonal offset between turning points of beams A and B} \\ &\alpha: \text{rotated angle} \\ &\varepsilon: \text{strain} \end{aligned} \tag{2.4}$$

and thus

$$\varepsilon = \frac{O\tan(\alpha)}{L_A + L_B + W} \tag{2.5}$$

However, the angle α can be measured by tip deflection y by the following expression:

$$\tan(\alpha) = \frac{y}{L_c + \frac{1}{2}O} \tag{2.6}$$

and thus the strain can be expressed by

$$\varepsilon = \frac{Oy}{(L_A + L_B + W)(L_c + \frac{1}{2}O)} \tag{2.7}$$

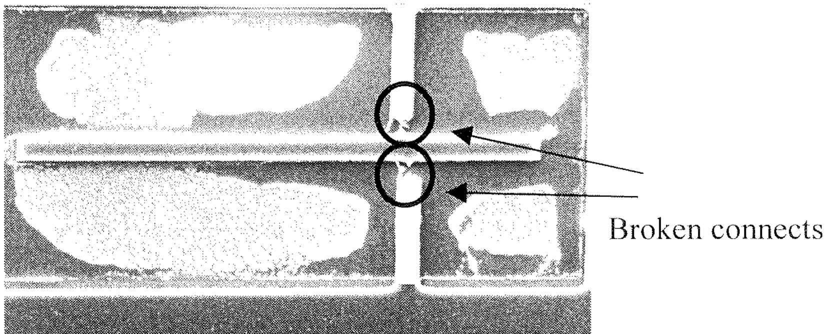

Fig. 2-23: A bad roatating-tip; the connections are broken

Thus, the strain and the tip deflection have a linear relationship. Thus, to ease the difficulty of measurement, L_C can be made as long as possible. However, this

optimization is constrained with the bending of the tips. Furthermore, the distance O has to be made as small as possible to enlarge the tip rotation. However, a value of O less than 5μm increases the difficulty of the lithography steps and further O_2 plasma etching processes for our Parylene microstructures. The small value of O also imposes big challenges on the stiffness of the turning points. For our purposes, turning points are made of Parylene and thus are easy to break as shown in Fig. 2-23.

The other factor that would change the accuracy of this method is the turning point width. As imagined, the large turning point width would impose hindrances for the tip to rotate freely. However, tips with small turning point widths are easily broken and more difficult to fabricate. Various researchers [22] have simulated this problem using finite element programs such as ANSYS. The results are shown in Fig. 2-24. Accordingly, the strain/rotation distance has to be modified as

$$\varepsilon = \frac{Oy}{(L_A + L_B)(L_C + \frac{1}{2}O)} \frac{1}{C_F} \quad (2.8)$$

where C_F is the correction factor.

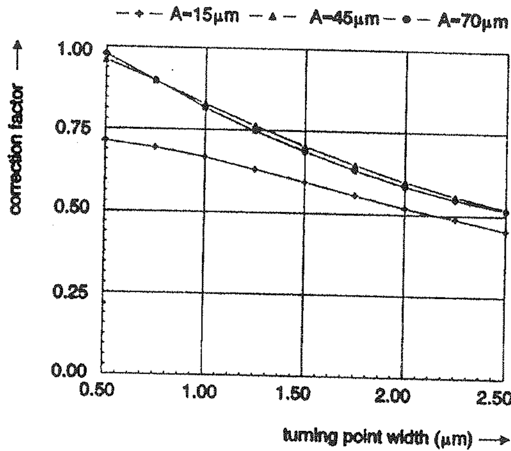

*Fig. 2-24:*Correction factor as function of the turning-point width For different arm lengths (L_A=L_B=A)

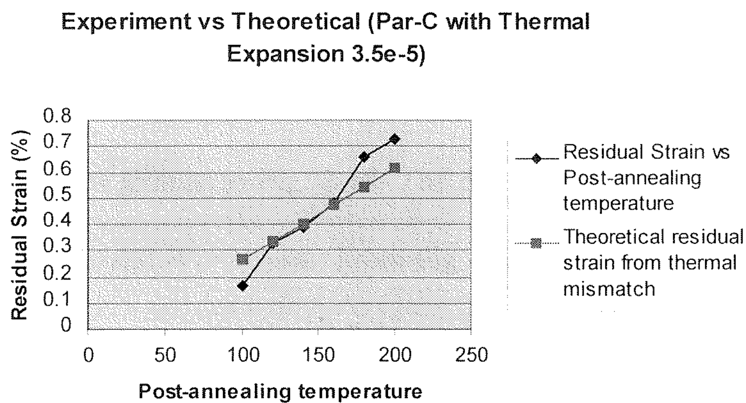

Fig. 2-25: Parylene stresses vs. theoretical thermal mismatch (only TCE of Parylene considered)

From Fig. 2-24, we can deduce that as the turning point width increases, the sensitivity drops significantly and has to be compensated by smaller correction factors. Considering the difficulty of lithography and the following plasma etching steps, the rotation tips width is set at 2.5μm and separation is set at 5μm for this study.

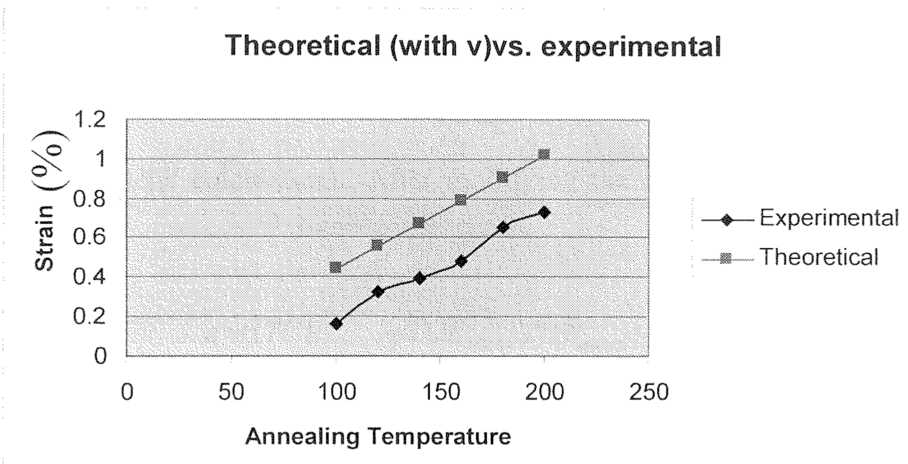

Fig. 2-26: Parylene stresses vs. theoretical thermal mismatch (possion ratio and TCE differences considered)

2.4.3 Measurement of stresses in thin-film Parylene

The relationship between the pre-annealing temperature and residual stresses of Parylene will be studied in this section. The rotation tips under study here are fabricated with a process flow similar to Fig. 2-18. The dimensions of the tips are $L_A=L_B=65\mu m$, $W=20\mu m$, $O=5\mu m$, and $W_b=2.5\mu m$. From Fig. 2-24, these values give $C_F=0.5$, which is then used to calculate strain using eq. 2-8. All the devices are annealed for 30 minutes at the targeted temperature prior to the BrF_3 dry release. As shown in Fig. 2-25, the strain shows a linear dependency on the annealing temperature. On the figures, the theoretical curves are calculated using the following equations:

$$\begin{aligned} &\varepsilon = TCE_{par-C} * (T_{anneal} - T_{room}) \\ &TCE_{par-C} = 3.5*10^{-5} / °C \\ &T_{anneal} = \text{pre-annealing temperature (°C)} \\ &T_{room} = \text{room temperature (25°C is used)} \end{aligned} \quad (2.9)$$

The curve showing the large variation indicates that some other parameters are neglected here. Further examination of the above equation shows that neglecting the TCE of the silicon substrate may cause around a 5% error in ε. Other investigators [26] have

also suggested the importance of the Possion ratio,ν, which is often assumed to be 0.25. The experiment also indicates that a proper value for the Possion ratio of ν=0.4 should be used for the Parylene calculations. After modifying the equation, the theoretical value would be given as

$$\varepsilon = (TCE_{Par-C} - TCE_{silicon}) * (T_{anneal} - 25) / (1 - \nu) \tag{2.10}$$

The calculated value will be higher than the previous value predicted by eq. 2-9. However, as shown in Fig. 2-25, the theoretical value shows a parallel shift from the experimental result. Again this indicates that another parameter has to be considered. Previous study from Dabral *et al.*[27] shows that the assumption of stress relaxation at high temperatures is not completely correct. To measure the stresses at high temperature in Parylene-C thin film, Dabral *et al.* used wafer the warpage method outlined in section 2.4.2. The results from their experiment reveal that a constant compressive stress around 10MPa exists in Parylene thin film at elevated temperatures from 50° to 250°C. This observation can also be seen in our structures shown in Fig. 2-27. If we consider this effect and put the correction term into consideration, the strain can be calculated as

$$\varepsilon = (TCE_{Par-C} - TCE_{silicon}) * (T_{anneal} - 25) / (1 - \nu) + \frac{\sigma}{E} \tag{2.11}$$

where E is the Young's modulus of the Parylene film around 4.5GPa. The resulting strain versus theoretical curve is given in Fig. 2-28, showing good agreement with the experimental results.

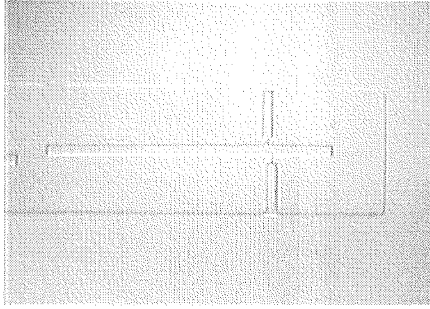

Fig. 2-27: Photo of rotating tips at elevated temperature (140°C); slightly compressive stress is shown by the direction of the rotation

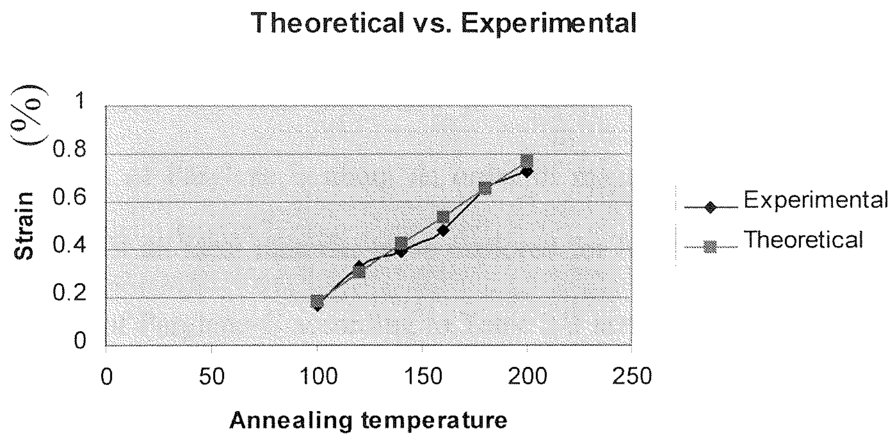

Fig. 2-28: Parylene stresses vs. theoretical thermal mismatch (initial compressive strain is assumed)

It is clear that the stresses inside the Parylene film are directly related to the thermal history of the fabrication processes. To fully control the stresses of the Parylene film, multiple layers of Parylene film should be annealed at elevated temperatures prior to release. However, this step causes a huge constraint on the processes using photoresist as a sacrificial layer, because hard-baked photoresist are usually more difficult to be released in common solvents such as IPA, acetone, or even photoresist stripper.

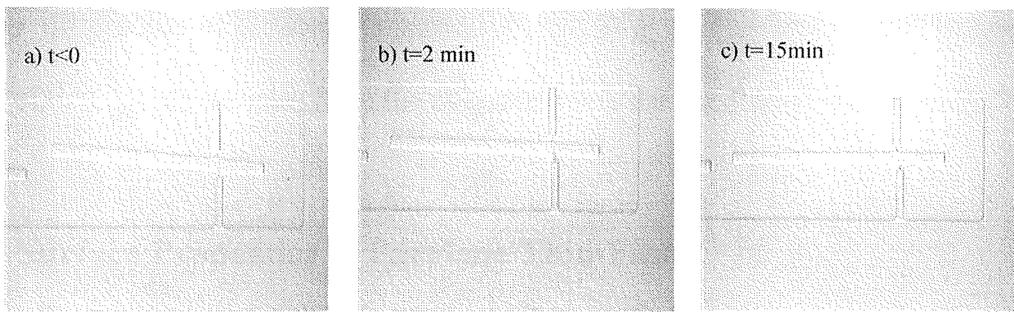

Fig. 2-29: Photos of rotating tips used to measure thermal expansion of coefficient (TCE)

2.5 Thermal Properties of Parylene

Initially, thermal properties of the Parylene are used to explore bimorphic actuation mechanisms discussed previously in Chapter 1. According to Table2-3, the thermal expansion of Parylene is about an order of magnitude higher than the silicon substrate, making it an ideal material to be explored for bimorphic actuation. However, the melting point of Parylene-C according to Table 2-3 is only 290°C; this is too low for a typical bimorphic operation a 600°C. Moreover, the Young's modulus of Parylene is much lower than that of silicon. Hence, the output force generated using Parylene will generally have much lower force output compared to that of silicon.

The rotation tips method developed in the previous sections provide an easy way to measure the thermal expansion coefficient (TCE) in thin film. This data will be used for comparison against the manufacturer's data. As shown in the following picture sequences in Fig. 2-29, the tips are placed at elevated temperatures until the tip deflection stabilizes. The tips are immersed into the high-temperature oil to also prevent the undesired stiction of the tips to the substrate. The time required to reach the equilibrium position is determined by the time constant of the whole apparatus. By calculating the

angle differences at different temperatures, the TCE of Parylene C is calculated to be $3.8*10^{-5}/°C$. This deviates from the manufacturer's data of $3.5*10^{-5}/°C$ by only 10%.

2.6 Surface Properties of Parylene Thin-Film

Surface forces are at the origin of surface properties exhibited by all kinds of materials. The forces generated can be Van Der Waal's forces, electrostatic forces (hydrogen bond, acid-base and covalent), and hydrophobic forces [6, 28]. Parylene has unavoidably complicated surface properties, which changes with the processing steps used in micromachining applications. Therefore, it is necessary to understand the surface properties of Parylene (i.e., hydrophobicity) in order to utilize the material for MEMS applications. For example, high hydrophobicity may lead to the difficulty of applying photoresist to the surface for lithography steps. Parylene, as will be discussed later, is often used to make microchannels for biological applications. The surface properties of Parylene could change the flow rate inside the channel significantly, so prior understanding and treatment of the material are necessary before it is used in such applications.

This section will be divided into two parts. The first part will focus on the understanding of the effect of intricate processing steps to the Parylene surface using contact angle measurements. The second part will focus on the characterization of microflow inside Parylene microchannels.

2.6.1 Parylene Surface characterized by Contact Angle Measurement

Contact angle measurement is probably the most common method of solid surface tension measurement. Contact angle data, especially in the case of polymeric materials, can be obtained from low cost instruments along with simple techniques [6]. Typically, the surface of liquid/solid/air interface can be best described using Young's law with the schematics shown in Fig. 2-30. At equilibrium, the three forces at the interface should be balanced to prevent the liquid from moving. Therefore,

$$
\begin{aligned}
&\gamma_{sa} = \gamma_{sl} + \gamma_{la}\cos\theta_C \\
&\theta_c : \text{contact angle} \\
&\gamma_{sa} : \text{surface tension of solid/air interface} \\
&\gamma_{sl} : \text{surface tension of solid/liquid interface} \\
&\gamma_{la} : \text{surface tension of liquid/air interface}
\end{aligned}
\quad (2.12)
$$

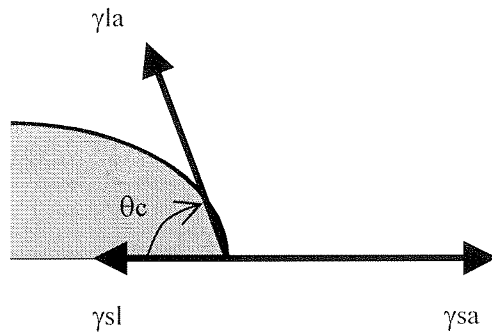

Fig. 2-30: Schematics of liquid/ solid/ air interface at equilibrium

By measuring the contact angle of the water/air/Parylene interface, the surface properties can be calculated using Young's law above. Table 2-4 shows the contact angle measurement on the surface and its effect on the Parylene surface; this data will provide us with the fundamental understanding of the effect of different processing steps to the Parylene surface. This will become useful for the microchannel flow characterization presented in the next section.

Table 2-4: Contact angle measurements of water on different Parylene-C surfaces

Surface Treatment	Contact Angle (°)	Effect on Parylene Surfaces	Adhesion between Parylene/substrate Interfaces
Without Treatment	75°	N.A.	N.A.
Au etchant	75°	None	None
Chrome etchant	61°	Hydrophilic	None
BHF	75°	None	Adhesion attacked (long >2hrs immersion)
HF	75°	None	Adhesion attacked (long >2hrs immersion)
Acetone	75°	None	None
IPA	75°	None	None
O_2 plasma	<5°	Hydrophilic	None
SF_6 plasma	105°	Hydrophobic	None
Piranha Cleaning (3mins)	62°	Hydrophilic	Attacked
A-174	82°	Hydrophobic	None

It is clear that surface treatments, especially those with plasma involved, can readily change the surface properties of Parylene. For plasma applications, oxygen plasma most likely embeds hydroxyl groups on the surface of the Parylene, decreasing the contact angle. Similarity, SF_6 plasma embeds fluorine atoms into the surface and

therefore increases Parylene's hydrophobicity. This information will aid in the characterization of microchannel flow inside the Parylene channels presented in the next section.

2.6.2 Measurement of flow in a Parylene Microchannel

This section will describe a new method and an analytical model for characterizing the surface energy inside a microchannel using the measurement of the marching velocity of a capillary meniscus. This method is based on the fact that surface tension of a liquid meniscus in a hydrophilic case produces pressure to pull liquid into the channel. Hence, the velocity of the liquid meniscus is related to the surface energy. Both Parylene and silicon nitride microchannels with different surface conditions were fabricated to perform the liquid-filling experiments. It will be shown that our model agrees quite well with the data.

Capillary phenomena had been well studied in the early parts of the 19th century. There has been almost no new progress made since then due to the constraints of experimental facilities and techniques. The capillary phenomena can be defined quantitatively in terms of surface tension. Surface tension makes the surface of a liquid act like an elastic sheath, minimizing the surface area of the liquid so as to lower the energy of the fluidic system to a minimum. Although the liquid/solid contact angle method [6] has been established for decades for measuring the surface energy of a flat surface, there is no existing method to our knowledge for measuring the surface properties inside a capillary tube, especially in the micro domain. The difficulty is that once the microchannel is built, it is hard to unfold the microchannel and measure the

contact angle. Therefore, measuring the meniscus velocity inside the microchannel provides a convenient way to measure the surface properties inside the microchannel.

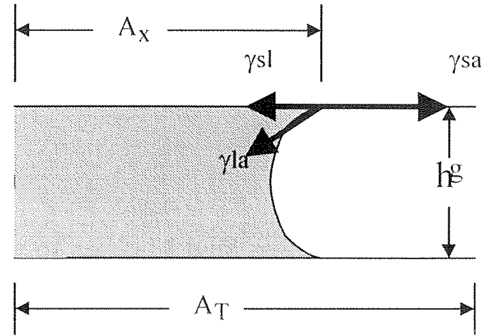

Fig. 2-31: The configuration of a microchannel; h is the channel height. A_X denotes wetting area with the length of x, and A_T denotes the total area with the length of L.

Surface energy

From the energy perspective, the effective surface tension force applied on the fluid column can be deduced from the derivative of the surface energy of the whole fluid system with respect to the spatial coordinates. Figure 2-31 shows a configuration of a capillary microchannel. The total surface energy of the capillary channel is composed of four parts. The first one is the vacant area (A_T-Ax) multiplied with γ_{sa}. The second part is the wetting area Ax multiplied with γ_{sl}. The third part is the surface energy E_0 stored in the filling reservoir. E_0 hardly changes due to the infinitesimal amount of liquid filling into the capillary. The fourth part is the complex surface of the capillary meniscus front multiplied by γ_{la}. We neglect the fourth term for the very small area of meniscus front compared to the other surfaces. Therefore, the total energy of the capillary channel in Fig. 2-31 can be expressed as

$$E_S = E_0 + [A_T\gamma_{sa} + A_X(\gamma_{sl} - \gamma_{sa})] \tag{2.13}$$

Assuming the cross section of the capillary channel in Fig. 2-31 is rectangular with a width of g and height of h, the total energy can be expressed as

$$E_S = E_0 + 2(h+g)[L\cdot\gamma_{sa} - x\cdot(\gamma_{sa} - \gamma_{sl})] \quad (2.14)$$

Capillary force

Taking the derivative of eq. 2-14 with respect to x, we obtain the equivalent force F applied on the capillary fluid column along the x direction:

$$F = -\frac{dE_S}{dx} = 2(h+g)\cdot(\gamma_{sa} - \gamma_{sl}) = \Delta p_{la}\cdot g\cdot h \quad (2.15)$$

The pressure drop across the liquid-air interface is therefore deduced under the assumption that the channel height h is much smaller than the channel width g.

$$\Delta p_{la} \approx \frac{2(\gamma_{sa} - \gamma_{sl})}{h} \quad (2.16)$$

Eq. 2-16 can be rewritten as the so-called "Laplace pressure drop" for the circular capillary tube by changing the channel characteristic length by the hydraulic diameter D_h ($=2r_h=2r\cos\theta_C=2gh/(g+h)$).

$$\Delta p_{la} = \frac{2(\gamma_{sa} - \gamma_{la})}{r}, \quad \text{Laplace equation} \quad (2\text{-}17)$$
$$r: \text{the radius of the capillary tube}$$

Laplace eq. 2-17 demonstrates that the smaller the channel dimension, the larger the pressure drop across the liquid-air capillary interface.

The measurement of contact angles

The contact angle measurement is a powerful method to study open surface properties. However, measuring the inner surface properties is much more difficult. A

delicate apparatus for capturing the meniscus images in quartz capillary tubes for measuring the meniscus velocity is reported by Sobolev [29], where the gas pressure, position, velocity and dynamic contact angle of a meniscus are correlated. The measurement of the inner surface properties of a microchannel is very important for microfluidics and bioMEMS.

Microfluidic properties are even more difficult to characterize and quantify in terms of dimensional control and applications of other parameters (e.g., pressure). Experimentally, filling water into a microchannel with different surface conditions can generate a variety of marching velocities for the same liquid, providing a more elegant way of characterizing inner surface properties.

The velocity model of marching meniscus

Once the pressure drop of a meniscus front is known, one can use the incompressible Navier-Stokes equation to derive the velocity capillary meniscus front [30]. Treated as an one-dimensional time-variant fluid field with only the horizontal velocity variable u generally varying with the spatial coordinates and time, the instantaneous position of capillary meniscus L(t) is described using the following differential system.

Continuity equation (conservation of mass):

$$\frac{\partial u}{\partial x} = 0; (\Rightarrow u = u(y, t)) \tag{2-18}$$

Momentum equation (conservation of momentum):

$$\frac{\partial u}{\partial x} = -\frac{1}{\rho}\frac{dp}{dx} + \frac{\mu}{\rho}\frac{\partial^2 u}{\partial y^2}; \left(-\frac{dp}{dx} = \frac{2(\gamma_{sa} - \gamma_{sl})}{h \cdot L(t)}\right) \tag{2-19}$$

Position of meniscus:

$$u(0,t)=\frac{dL(t)}{dt} \tag{2-20}$$

Boundary condition:

$$u(h,t/2)=0 \text{ and } \frac{\partial u}{\partial y}(0,t)=0 \tag{2-21}$$

Initial condition:

$$u(y,0)=0\ ;\ L(0)=L_0 \tag{2-22}$$

The velocity variation along the y-direction is not important in this model. We substituted a parabolic distribution eq. 2-23 of u(y,t), which satisfies the non-slip boundary conditions eq. 2-22 automatically, into eq. 2-19. We then obtain eq. 2-24.

$$u(y,t)=u_0(t)\cdot\left[1-\left(\frac{2y}{h}\right)^2\right] \tag{2.23}$$

$$u_0'(t)\cdot\left[1-\left(\frac{2y}{h}\right)^2\right]+\frac{\mu}{\rho}\frac{8}{h^2}u_0(t)=\frac{2(\gamma_{sa}-\gamma_{sl})}{\rho\cdot h\cdot L(t)} \tag{2-24}$$

Eq. 2-24 demonstrates the force balance between the momentum of channel- flow and the meniscus (Laplace) pressure-drop. It will inherently be reasonable if we additionally take the average of it along the y-direction. The initial value problem (IVP) of the marching position L(t) of capillary meniscus with respect to time then becomes:

$$\left(L''+\frac{12\mu}{\rho h^2}L'\right)\cdot L=\frac{3(\gamma_{sa}-\gamma_{sl})}{\rho h} \tag{2-25}$$

$$\text{I.C.: } L'(0)=0;\ L(0)=L_0 \tag{2-26}$$

Since there is no exact solution to the nonlinear IVP 2-25,26, we have to solve it numerically. However, if we neglect the acceleration (2nd derivative) term of eq. 2-25,

which is the case in our time domain (t>>μs), then the simplified secular solution of L(t) can be regarded as the marching position following a square-root relation with time (D is a diffusing coefficient).

$$L(t) = \sqrt{L_0^2 + Dt}, \quad D = \left(\frac{h \cdot (\gamma_{sa} - \gamma_{sl})}{2\mu} \right) \tag{2-27}$$

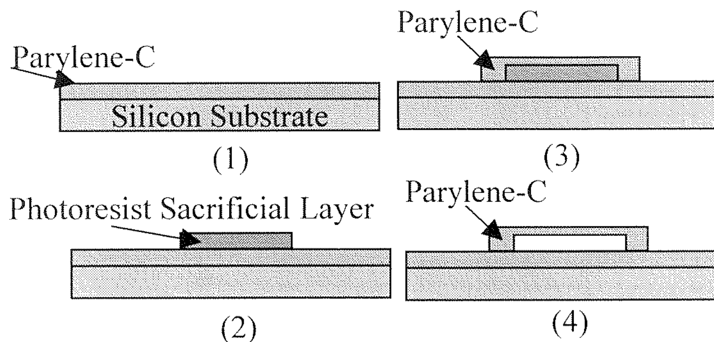

Fig. 2-32: Fabrication steps of surfaced micromachined Parylene microchannel

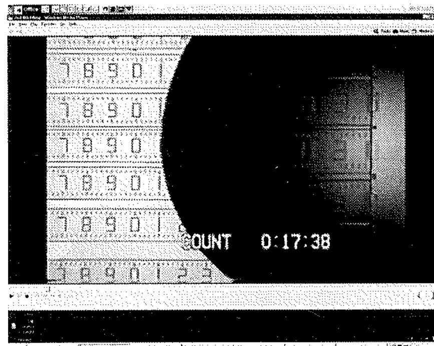

Fig. 2-33: The Parylene channels of 2mm long, with the height of 3μm, the width of 80, 40, 20, 10 μm (from bottom to top) on a silicon chip. Each small step of the ruler is 20 μm. The water droplet (dark area) serves as a reservoir at inlet.

Results and Discussion

Experimentally, silicon chips with Parylene microchannels are fabricated as shown in Fig. 2-33 with a processing flow in Fig. 2-32 to perform the water-filling experiment. The moving images of the water meniscus for a Parylene channel with a

width of 10μm, height of 3μm, subjected to dried, pre-wetted and pretreated (with agents other than water) inner walls, were recorded through an optical microscope and a CCD into a VCR tape. We transformed the VCR images into digital movie files, which have a time resolution of 1/30 sec. Finally, information regarding the position of the moving meniscus was collected and plotted in Fig. 2-34.

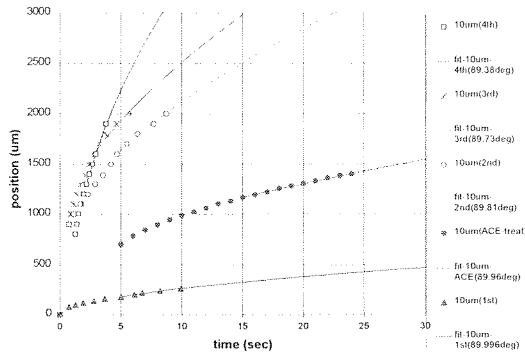

Fig. 2-34: The position of a capillary meniscus vs. time of DI water filling into a Parylene channel. The fitting curves depict the theoretical prediction.

By fitting the data according to the square root in eq. 2-27, we obtained the diffusing coefficient D in Table 2-5. Clearly, the square-root dependence is valid and this model fits with the experimental data fairly well as shown in Fig. 2-34. The results shown in Table 2-5 reveal small values of the surface energy difference ($\gamma_{sa} - \gamma_{sl}$) compared to the surface energy of water (γ_{la} =0.073 Nt/m). This correlates to the dynamic contact angles θ_c of 90° for different cases of water meniscus in a Parylene microchannel, although the diffusing coefficient D changes over three orders of magnitude. This water-filling observation shows the importance of sample preparation when conducting experiments on polymer surfaces. The change in Parylene surface energy with different processes is a well-known and intricate phenomenon. Processes such as photoresist spinning and stripping, plasma roughening, and solvent immersion would change the

surface from hydrophobic to completely hydrophilic as discussed in the previous section. However, these changes can sometimes be reversed after air-drying the sample so the surface would return to the original surface state.

Table 2-5: The experiment results of water-filling experiments

	Diffusing Coefficient D (μm^2/sec)	Surface Energy Difference ($\gamma_{sa} - \gamma_{sl}$) Nt/m	Conditions
A	68450	$3.51*10^{-5}$	Pre-treated with acetone for three times before filling water
B	7584	$3.89*10^{-6}$	1st time of filling water after stripping PR (dried capillary)
C	361500	$1.85*10^{-4}$	2nd time of filling water (pre-wetted capillary)
D	514300	$2.637*10^{-4}$	3rd time of filling water
E	1177000	$6.036*10^{-4}$	4th time of filling water

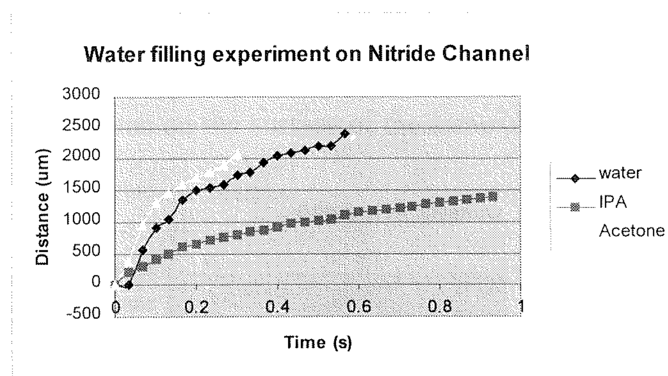

Fig. 2-35: The position of a capillary meniscus vs. time of different liquids filling into a silicon nitride microchannel

The velocity variation due to different surface states

The large variation of diffusion coefficient D and the meniscus velocity in Table 2-5 can be explained by surface humidity of the Parylene micro-channel. Right after the first filling and drying, the inner Parylene surface adsorbs water molecules, allowing the water to flow easier into the micro-channel with a much higher (two order of magnitude higher) speed. It is also interesting that the velocity shifts somewhat back to the case of the first water-filling in Table 2-5, if we treat the inner channel surface with acetone again (just as the situation of stripping away the sacrificial photo-resist).

To further test the theory developed for the water-filling experiment, Si_xN_y microchannels are also fabricated using 0.5μm polysilicon as the sacrificial layer. The sacrificial polysilicon is finally etched away using TMAH and the channels are also subjected to Piranha cleaning (mixture of H_2O_2 and H_2SO_4) prior to testing. The results are shown in Fig. 2-35. The diffusion coefficient extracted from the water experiment in Fig. 2-35 shows a surface energy difference of 0.0395Nt/m. This value corresponds to a dynamic contact angle of 57.24°, which is close to the steady-state contact angle measurement of 45° done on the surface of the same chip.

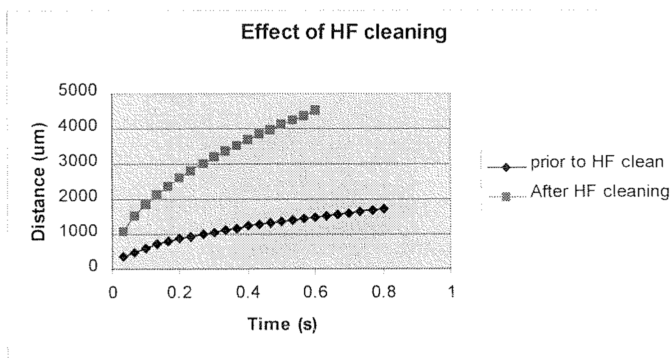

Fig. 2-36: The effect of diluted HF cleaning

Cleaning of the Parylene Surfaces inside microchannels

Thus, the fill-in experiment herein not only describes the surface tension–driven mechanism but also the surface state of a micro-channel. Therefore, it is interesting and necessary to find out under which conditions the surface of Parylene microchannels discussed in this section can be brought back to the original conditions. Several solvents such as acetone, IPA, Piranhna solution, BHF, and diluted HF have been used to treat the air-dried Parylene microchannels. The best result is obtained by using 5% hydrofluoric acid (HF) solution in water. The channel is first taken out of the acetone releasing solution and immediately put into DI water. After 30 minutes, the channels are air-dried for another half-hour to prevent any residue build-up inside the microchannels. The channels are then placed into a 5% dilute HF solution for 30 minutes prior to testing. As shown in Fig. 2-36, the surface contact angle inside Parylene microchannels is reduced from the hydrophobic case (~90°) to almost the original surface contact angle of 72° (the original is 75°). This change is probably due to the organic-removal process during the immersion in the diluted HF solutions.

Therefore, by controlling the surface properties of the microchannels, the flow rate can be manipulated. Moreover, this method provides an elegant way of characterizing microchannel properties.

2.7 Conclusions

In this chapter, the process of Parylene deposition was described. Moreover, the mechanical, electrical, thermal and surface properties are examined for various micromachining applications that will be explored in the later chapter. Other unique properties such as chemical inertness and optical properties of Parylene are not included in the discussion because they are not used in this work. From the above discussion, the combination of many unique properties makes Parylene an interesting polymeric material for micromachining applications. In a later chapter, the high elongation to break property from its polymeric nature will be explored to make corrugated membrane for thermopneumatic microvalve applications. The high electrical insulation properties will be investigated to make surface micromachined microvalves. Finally, Parylene's conformal deposition characteristics will also be examined in its use as a supporting material for the electret microphone.

2.8 References

[1] X.-Q. Wang, "Integrated Parylene Micro Electro Mechanical Systems (MEMS)," Ph.D. thesis, California Institute of Technology, 2000.

[2] http://www.scsalpha.com/indexus.htm

[3] M. Madou, *Fundamentals of Microfabrication*. Boca Raton, New York, CRC Press, 1997.

[4] R. Sabeti, E. M. Charlson, and E. J. Charlson, "Selective Deposition of Parylene," *Polymer Communications*, vol. 30, June1989.

[5] M. Gazicki, G. Surendran, W. James, and H. Yasuda, "Polymerization of Para-Xylyene Derivatives (Parylene Polymerization). II. Heat Effects during Deposition of Parylene C at Different Temperatures," *Journal of Polymer Science*, vol. 23, pp. 2255-2277, 1985.

[6] F. Garbassi, M. Morra, and E. Occhiello, *Polymer Surfaces-- From Physics to Technology*, John Wiley&Sons, 1998.

[7] M. A. Brook, *Silicon in Organic, Organometallic, and Polymer Chemistry*, John Wiley & Sons, Inc., 2000.

[8] X. Q. Wang, X. Yang, K. Walsh, and Y. C. Tai, "Gas Phase Silicon Etching with Bromine Trifluoride," 1997 International Conference on Solid-State Sensors and Actuators (Transducers '97), Chicago, IL, 1997.

[9] T. E. Bell, K. D. Wise, and D. J. Anderson, "Flexible Micromachined Electrode array for Cochlear Prosthesis," 1997 International Conference on Solid-State Sensors and Actuators (Transducers '97), Chicago, IL, 1997.

[10] J. R. Webster, "Monolithic Structures for Integrated Capillary Electrophoresis Systems," Ph.D. thesis, University of Michigan, 1999.

[11] P. F. Man, D. K. Jones, and C. H. Masreangelo, "Microfluidic platic capillaries on silicon substarte: a new inexpensive technology for bioanalysis chips," Proceedings of the 1997 International Workshop on Micro ElectroMechanical Systems (MEMS '97), Nagoya, Japan, 1997.

[12] M. Hikita, T. Hirose, Y. Ito, T. Mizutani, and M. Ieda, "Investigation of electrical breakdown of polymeric insulating materials using a technique of pre-breakdown current measurements," 1990.

[13] T. Mori, T. Matsuoka, and T. Mizutani, "The Breakdown Mechanisms of poly-p-xylyene Film," *IEEE Transactions on Dielectrics and Electrical Insulation*, vol.1, pp.71-76, 1994.

[14] P. S. H. Henry, *Journal of Applied Physics*, vol. 4 (Suppl. 2), pp.31, 1953.

[15] R. A. Creswell and M. M. Perlman, *Journal of Applied Physics*, vol. 41, pp. 2365, 1970.

[16] P. W. Chudleigh, *Applied Physics Letter*, vol. 21, pp. 547, 1972.

[17] L. G. Brazier, *Engineer*, vol.196, pp. 637, 1953.

[18] B. Gross, *Journal of Polymer Science*, vol.27, pp.135, 1958.

[19] T. Y. Hsu, "A Novel Electron Beam Source Based on the Back-Lighted Thyratron," Ph.D. thesis, University of Southern California, 1992.

[20] http://www.Parylene.com

[21] http://www.eecs.berkeley.edu/~pister/245/Notes/Fab2.pdf

[22] B. P. v. Drieenhuizen, J. F. L. Goosen, P. J. French, and R. F. Wolffenbuttel, "Comparison of techniques for measuring both compressive and tensile stress in thin films," *Sensors and Actuators A*, vol. 37-38, pp. 756-765, 1993.

[23] Nancy A. Winfree, Wen H. Hsieh, R. Wu, and Y.-C. Tai, "The Effects of Boundary Conditions on Implementing the Stoney Formula for Stress Measurements," *TRANSDUCERS '93 The 7th International Conference on Solid-State Sensors and Actuators*, 1993.

[24] T. A. Harder, T. J. Yao, Q. He, C. Y. Shih, and Y. C. Tai, "Residual Stress in Thin-Film Parylene-C," Proceedings of IEEE Workshop on Micro Electro Mechanical Systems (MEMS '02), Las Vegas, NV, 2002.

[25] O. Tabata, "Mechanical Property Measurements of Thin-Films Using Load Deflection of Composite Rectangular Membranes," *Sensors and Actuators A*, vol. 20, pp.135-141, 1989.

[26] W. Sim, D. Kim, K. Kim, and K. Kown, "Fabrication, Test and Simulation of Parylene Diaphragm," *TRANSDUCERS '01 The 11th International Conference on Solid-State Sensors and Actuators*, 2001.

[27] S. Dabral, "Stress in thermally annealed parylene films," *Journal of Electronic Materials*, vol. 21, pp. 989-994, 1992.

[28] J. N. Israelachvili, *Intermolecular and Surface Forces*. London, Academic, 1992.

[29] V. D. Sobolev, *Journal of Colloid and Interface Science*, vol. 222, pp. 51-54, 2000.

[30] L. J. Yang, T. J. Yao, Y. L. Huang, Y. Xu, and Y. C. Tai, "Marching Velocity Of Capillary Meniscuses in Microchannels," Proceedings of IEEE Workshop on Micro Electro Mechanical Systems (MEMS '02), Las Vegas, NV, 2002.

CHAPTER 3

Thermopneumatic Microvalve with Corrugated Parylene Membrane

Abstract

In this chapter, the design, fabrication, and testing using a Parylene/silicone composite membrane in a bulk-micromachined thermopneumatic microvalve targeted for several slpm gas flow rate will be presented. First, a discussion of Parylene's exceptional properties in its use as a solvent barrier will be given. Then, the design and fabrication of a corrugated Parylene membrane using the soft characteristics of the Parylene polymer will be presented. In the second part, a microfluidic rubber coupler will be examined as a solution to simplify the packaging of the microvalve. The purpose of this rubber O-ring is to demonstrate a quick-connect between micro and macro fluidic world.

3.1 Preface

In the recent years, micromachining has provided a feasible way to miniaturize several fluidic components such as microvalves [1-3], pumps [4, 5], sensors [6], and mixers [7]. The biggest driving force for these applications is mainly to reduce the current instrumentation used in biomedical diagnostics. Moreover, it is shown that not only diagnostic systems will benefit tremendously from the application of

micromachining techniques [8], but also drug delivery, tissue engineering and minimal invasive therapy will benefit as well from the technology. Therefore, the field of microfluidics that encompasses the study of devices and the fundamental principle of the fluidic flow in microchannels and even nanochannels has grown immensely. However, the study of flow in very small channels is a challenging task. As the channel size reduces, the pressure required to reach the desired flow rate is high and, in some cases, the flow rate will be dominated by surface-tension driven flow as earlier discussed in Chapter 2. Therefore, a lot of separations use electro-osmotic pumping [9], electro-hydrodynamic pumping [10] or electrowetting [11] in the microdomain. Second, the surface-to-volume ratio increases as the fluidic channels are reduced its size, so the absorption of analytes and reagents is enhanced in miniaturized devices. Besides, several fundamental laws such as heat-transfer and flow continuum will reach their limits such that hypothetical flow models have to be modified to accommodate such extreme conditions [12].

However, over the past decades, most of the goals of micromachining efforts in microfluidics have been to provide a simple platform to reduce the sample volume required for chemical and pathogenic detection, to increase the yield and reduce the price of the single working component such as valves and pumps, and finally, to integrate various devices for sample preparation, separation, and fluidic control to sensing elements on a single chip. Therefore, the goal of microfluidics research is to aim for "μ-TAS," micro-total-analysis systems which enable high integration, high sensitivity, high speed, and low cost in diagnostic and biomedical applications.

In this chapter, a microvalve using high elongation properties of Parylene polymer is demonstrated. The actuation mechanism is chosen to be thermopneumatic for reasons

that will be discussed later in the chapter. In order to simplify the packaging of the microvalve, a microfluidic coupler using silicone will also be demonstrated in the second part of the chapter.

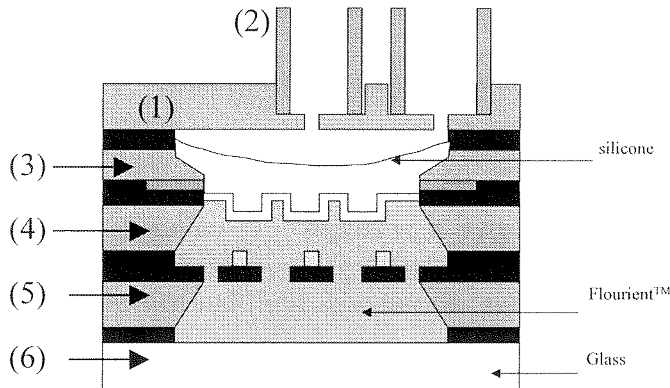

Fig. 3-1: The structure of designed thermopneumatic microvalve

3.2 Structures of the Thermopneumatic Microvalve

The designed microvalve structure, which is similar to the one in [13] consists of six different pieces as shown in Fig. 3-1. Six different pieces serving various functions are manually glued together.

(1) Valve seat: The improved valve seat is used to connect the external inlet/outlet stainless steel tubes to the microvalve. This piece is improved by using DRIE to enhance the yield of packaging. Nevertheless, this step is still the most critical step in assembling the device. In the second part of the chapter, a new microfluidic silicone O-ring coupler will be designed to further simplify the packaging steps.

(2) Stainless tube: The stainless steel tube is used to connect the devices to the Tygon tubing used for measurement.

(3) The silicone/Parylene composite membrane: The cured silicone rubber provides automatic recess to be used as a fluidic channel, so no extra chip is required to form the fluidic channels.

(4) A bulk-micromachined silicon spacer: This chip is used to increase the fluid volume and to separate the direct contact between membrane and the integrated heater.

(5) Integrated heater: The integrated Cr/Au electrodes on the nitride membrane borrowed from previous studies [13] serves as a freestanding heater and to increase the contact area of the heater and fluid. The nitride membrane is used to provide low-heat loss conducted through the substrate.

(6) Backside glass cover: This chip is to seal the fluid and to reduce the heat loss through the substrate by low thermal conductivity of glass compared to silicon.

Finally, each piece in the experiment is manually glued using "5 minute epoxy." The reason to use epoxy instead of direct bonding is because most of the bonding techniques requires high temperature or high pressure and therefore is not well suited for bonding between piece (1)/(3) and (3)/(4)[14, 15]. Besides, due to the high evaporation rate of working fluid PF5060[3], it is also difficult to bond (5)/(6) without fluid leakage. Therefore, the glue method is used for laboratory use, which causes an undesired effect as will be demonstrated later.

In the next couple of sections, key components in thermopneumatic actuation will be discussed in detail. The chapter will first discuss the choice of the actuation mechanism used to explain why thermopneumatic actuation is chosen. Second, the silicone membrane technology developed by Yang *et al.* [13] will be reviewed. Third, the

corrugated membrane using Parylene will be designed and characterized to form a composite silicone/Parylene membrane. Fourth, the fabrication of the valve seat and channel characterization will be provided. Finally, the device will be assembled and tested under compressed N_2 gas flow.

3.3 Thermopneumatic Actuation

Different actuation mechanisms have been described in Chapter 1. For the thermopneumatic valve application of interest here, the actuation mechanism has to provide at least 10 psi of pressure with a traveling distance of around 90μm. This 90μm distance is set by the automatic recess formed by cured silicone. The recess here is also used for fluidic channels for gas passing through the devices and, therefore, the channel depth has to be in the several tens of microns range to reach the desired ml/min flow rate.

Over time, numerous microvalves have been demonstrated using different mechanisms such as electrostatic [1], thermal bimorph [2], piezoelectric [16] and, of course, thermopneumatic [3]. However, as shown in Chapter 1, electrostatic mechanism only provides a large force when the distance is less than 5 μm and thus is not suitable for our application. A thermal bimorph usually requires a high operating temperature and would affect the gas passing through the channel. A piezoelectric mechanism usually requires an external PZT glued onto the membrane and therefore can not be integrated easily.

Therefore, the most promising mechanism for the microvalve application is the thermopneumatic mechanism, which easily provides a large pressure and long traveling distance, with a moderate temperature increase from the surrounding. As described in

Chapter 1, the thermopneumatic force is generated while the fluid or gas is being heated up. When the fluid or gas is heated up inside a sealed cavity, the volume of the gas cannot expand and thus increases the pressure. This pressure can be calculated by the equation 1-3 and rewritten here for reference.

$$\Delta P = E(\beta \Delta T - \frac{\Delta V}{V}) \tag{3.1}$$

where

E: bulk modulus of elasticity

β: thermal coefficient of expansion

ΔT: temperature increase

ΔV/V: volume increase percentage

In order to reach high performance of thermopneumatic actuation, it is preferred that the working fluid has a larger bulk modulus of elasticity (E) and thermal coefficient of expansion β. Moreover, in most cases the operation mode of the valve is mixed with both liquid expansion and gas expansion. Therefore, high vapor pressure would also help the device operations. Table 3-1 shows several of the important properties of fluid to be used as a working fluid here.

Table 3-1: Fluid properties for thermopneumatic operation

	E(psi)	β(/°C)	Vapor Pressure (torr)	Boiling Point (°C)	Melting Points (°C)
Water	$3.3*10^5$	$2.3*10^{-4}$	23.7	100	0
Acetone	N/A	$1.49*10^{-3}$	229.52	56.05	-94.85
Methanol	$1.3*10^5$	NA	100	64.55	-97.68
PF5060/ FC-72	NA	$1.6*10^{-3}$	232	56	-90

It is clear that the pressure generated by thermopneumatic operation is huge compared to what we need for the real application. Our target is only to generate around 1 psi of pressure and deflect the membrane by about 90μm. However, as the membrane deflects, the volume does change and therefore reduces the pressure drastically. As demonstrated by [13], the actual mechanism of thermopneumatic operation in our case is the mixture of gas expansion and liquid expansion. As shown in Table 3-1, the best working liquid is FC-72 or "Fluorinert™," since the thermal expansion coefficient of PF5060 is six times larger than water. In addition, they are chemically inert and non-toxic. Although the bulk modulus of the FC-72 is not available, it is believed it should be moderately high (~10^5psi) because PF5060 is its polymeric essence.

Although acetone and methanol are readily available and can provide enough pressure for the applications, acetone and methanol are problematic with the manual bonding procedures. The epoxy used for bonding is readily dissolved and swollen when it comes in contact with the acetone or methanol. Therefore, they are not used as working fluids.

3.4 Fabrication of Components for thermalpneumatic microvalve

In this section, several pieces of the components in the microvalve will be described in detail. First, silicone rubber, which has been used for many micromachining applications, will be discussed along with the method of applying the silicone. Second, the chemical resistance of Parylene will be examined, because Parylene serves as a solvent barrier inside the microvalve to prevent working fluid leakage. Third, a 10 μm-thick corrugated Parylene membrane will be designed and fabricated. The membrane

characteristics will be tested using the bulge method provided in the last chapter; the ultimate goal is to reach 90μm deflection with as little as 1 psi pressure difference. Fourth, the fabrication of the improved valve seat will be discussed and the channel flow rate will be characterized.

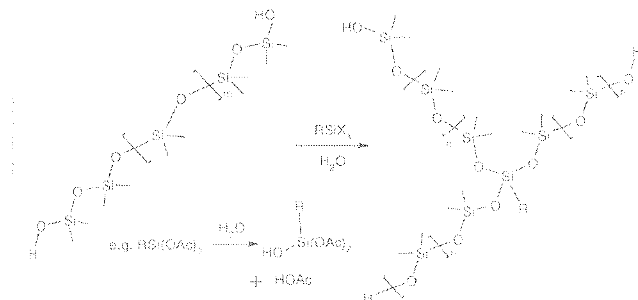

Fig. 3-2: Crosslinking of silicone by room temperature vulcanization (RTV)

3.4.1 Silicone Rubber as Membrane material

Silicones have found use in applications that requires direct human contact primarily because of their lack of significant bioactivity. Silicones (i.e., polysiloxanes) is derived from polymers with silicon-oxygen bonds or siloxanes bonds. The general chemical formula of silicone can be written as $(RR'SiO)_n$. The simplest silicones are therefore polydimethylsiloxanes(PDMS); PDMS is a clear fluid which is widely used as a sealant. Although silicone fluids (PDMS) are valuable materials, many applications require the material not to flow. There are several possible routes to crossslinking the polymers such as the incorporation if tri- or tetrafunctional silanes that can react under ionic conditions, or the use of organic residues on the silicone polymers to form the network.

However, the vast majority of silicone elastomers are prepared using three different crosslinking routes [17]: moisture cure (room-temperature vulcanization RTV), high-temperature vulcanization (HTV), transition metal-catalyzed hydrosilylation or

addition cure. For this study, only the RTV system and the addition-cure system will be discussed. In the moisture cure system, the hydroxyl-terminated polydimethylsiloxanes $[HO(SiMe_2O)_nH]$ form crosslinks by reacting with relatively small quantities of tri- or tetrafunctional silanes as shown in Fig. 3-2. The reactions occur at room temperature and therefore the term RTV is associated with the process. In this process, chlorosilanes can be used because of its excellent ability as leaving groups. However, as the use of the chlorosilanes leads to the formation of hydrochloric acid, and they generally not used commercially.

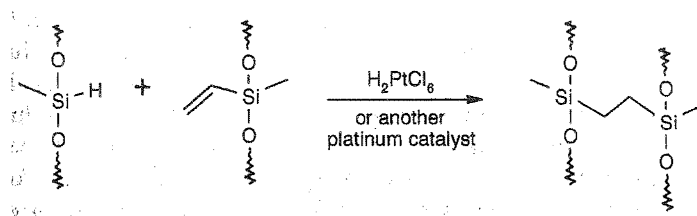

Fig. 3-3: Crosslinking of silicone by addition-cure

Fig. 3-3 shows a typical commercially available addition-cure route to crosslink silicones. The silicone is usually sold as a two-part system where one contains Si-H system while the other contains $Si\text{-}CH=CH_2$ system with the addition catalyst in this vinyl-polymer part. The reaction occurs rapidly and under mild conditions at room temperature. However, increasing the temperatures drastically increases the speed of vulcanization. The advantage of this system is that there are no by-products produced in the process, although residual platinum that remains trapped in the gel can turn the elastomer somewhat yellow. The silicone rubber MRTV1 used in the study is also a two-part addition-cure system with a mixing ratio 10:1 from the American Safety Technologies, Inc. As shown in Table 3-2, the silicone rubber has very tensile elongation

strength up to 1000%. However, the high viscosity makes it difficult for spin-coating applications in most MEMS applications (~μm).

Table 3-2: Physical Properties of MRTV 1 [13]

Mixed Viscosity, cps	60,000
Hardness, Durometer	Shore A 24
Tensile Strength, psi	500
Tear Strength, Die B lb/in	125
Tensile Elongation, %	1,000
Temperature Range, °C	-55 to 200
Thermal Conductivity, W/cm-°C	0.002
Dielectric Strength, Volts/mil	550
Volume Resistivity, ohm-cm	1.6×10^{15}

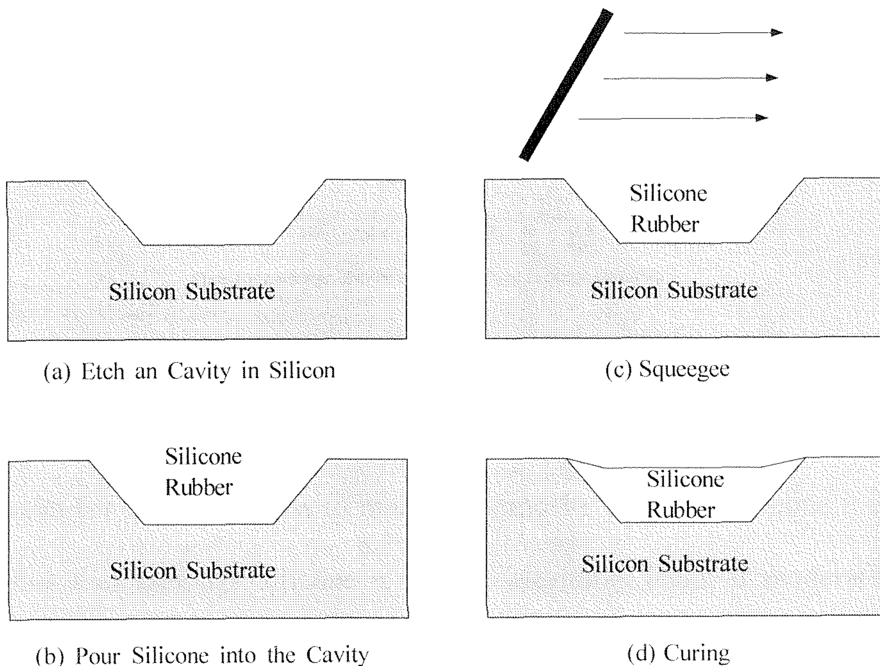

Fig. 3-4: Squeegee Coating of silicone (from [13])

Using the polymer as a solvent barrier is fundamentally a difficult problem and has been one of the important issues for the food packaging industry [19]. As shown in Fig.3-5 [19], silicone has permeability for moisture of around 10^{-8} g/cm-s-torr and would allow moisture to penetrate through in the order of minutes (assuming a 100μm thickness). Therefore, a diffusion barrier is required to overcome this constraint. However, the best solvent barriers are probably hard materials such as metals and glasses. Although these materials provide low permeability, they significantly increase the rigidity of the diaphragm and the consumption power.

Parylene as a polymer appears to be a good candidate as a solvent barrier here [20]. As shown in Fig. 3-6 [21], Parylene has a moisture permeability of around $2.25*10^{-13}$ g/cm-s, which is five orders of magnitude lower than silicone but one order of magnitude higher than glass. By considering their thickness, the composite membrane should have 2500 times of life expectancy to prevent the solvent from leaking through the diaphragm. Therefore, this would meet the requirement of our applications.

Table 5. Parylene Barrier Properties

Gas Permeability at 25 °C, (cm^3 (STP)·mil)/(100 in^2/d·atm)*					
Polymer	**N_2**	**O_2**	**CO_2**	**H_2**	**Moisture Vapor Transmission at 90% RH, 37 °C, (g·mil/100 in^2·d)****
Parylene N	7.7	39	214	540	1.5
Parylene C	1.0	7.2	7.7	110	0.21
Parylene D	4.5	32	13(a)	240	0.25
Epoxides	4	5-10	8	110	1.79-2.38(a)
Silicones	-	50,000	300,000	45,000	4.4 - 7.9(a)
Urethanes	80	200	3,000	-	2.4 - 8.7(a)

(a) Lacari, J.J. and Brands, E.R., *Machine Design*, May 25, 1967, p. 192.
* ASTM D 1434
** ASTM E 96

(International Conversion Chart, Page 12)

Fig. 3-6: Parylene barrier properties for moisture and gas

Moreover, Parylene resists chemical attack and is insoluble in all organic solvents up to 150°C [21]. Although some degree of swelling (~0.3%) does happen when Parylene is immersed into an organic solvent, in most cases the processing time is short and Parylene is consistently baked to prevent the accumulation of solvent inside the film.

3.4.3 Design and Fabrication of silicone/Parylene composite membrane

The diaphragm materials in typical MEMS structures are silicon, polysilicon, nitride and sometimes various metals. However, because of the intrinsically high Young's modulus and yield strength, membranes made from these materials can not achieve high deflections and therefore are not well suited for large deflection applications.

This section will focus on the design of a corrugated Parylene membrane. By corrugation, we imply that the thickness of the Parylene can be increased without sacrificing its softness. However, the target goal is to reach 80 μm deflection under 1 psi pressure as defined by the automatic-recess from the silicone membrane. This will be explained in detail at later sections.

Corrugated membranes are often used to provide larger deflections under equivalent loads and at the same time increase the linear operation range [22]. Assuming the residual stress is negligible (which is true for large deflections in this case), the pressure/deflection can be described as follows:

$$\frac{Pr^4}{Eh^4} = A_p(\frac{y}{h}) + B_p(\frac{y}{h})^3$$
$$A_p = \frac{2(q+2)(q+1)}{3(1-(\frac{v}{q})^2)}$$
$$B_p = \frac{32}{q^2-9}(\frac{1}{6} - \frac{3-v}{(q-v)(q+3)})$$
$$q = \sqrt{\frac{s}{L}(1+1.5(\frac{H}{h})^2)} \quad (3.2)$$

s: Corrugation arc length
H: Corrugation depth
L: Corrugation spatial period
r: Diaphragm radius
h: Diaphragm thickness
v: Possion ratio (0.25)
P: Applied pressure
y: Deflection at the center

As will be experimentally shown, the Parylene corrugation membrane itself will determine the stiffness of the composite Parylene/silicone membrane. Therefore, let us assume a Young's modulus for Parylene (4.5GPa), H(10μm), L(50μm,20μm), and s/L≈1(for shallow corrugations). The simulated load-deflection relationship is shown in Fig.3-7 using $r^2=4a^2/\pi$ with a=4mm.

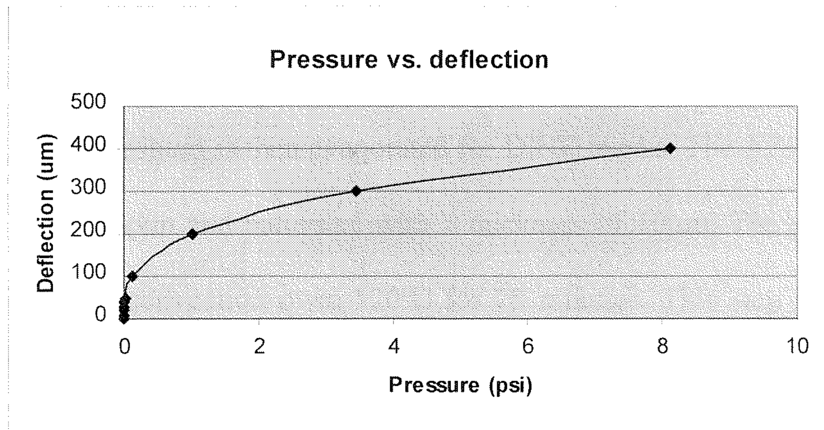

Fig. 3-7: The pressure v.s. deflection relationship for corrugated Parylene membrane (Residual stress is neglected)

From Fig. 3-7, it would only take less than 1 psi to reach a 200μm deflection, indicating that the design should be good enough for the application. However, the residual stresses are neglected in the simulation and shallow corrugation is assumed.

Experimentally, we will find that the deflection required for the application is still within the residual-stress-dominated region.

The study now will focus on the fabrication of the corrugated Parylene/Silicone composite diaphragm. The fabrication process for the corrugated membrane shown in Fig. 3-8 begins with a 5000Å LPCVD nitride deposition on 4'' silicon wafers for the KOH mask. The backside nitride is then patterned using the plasma etching system (SF_6(270mtorr)+O_2(30mtorr)). The wafers are then KOH etched for 22 hours until a 20μm silicon membrane is left. The reason for the remaining 20μm of silicon is to simplify the wafer-handling steps afterwards because the silicon membrane may be too fragile for the remaining processes. Besides, the remaining silicon membrane can also enhance heat conduction during the photoresist baking processes, helping to prevent the cracking of the photoresist during baking.

The frontside nitride is then patterned using a similar recipe as mentioned earlier, and 1000 Å of aluminum is then evaporated for DRIE masks. The AZ9260 photoresist at this stage is then spun and patterned with a thickness of 10μm. The photoresist is then hard-baked in the convection oven 120°C for 20 minutes. This step is critical because thick photoresist tends to crack during the baking process and is difficult to expose using a stepper with depth of focus around 2 μm. This is the most important motivation to use AZ9260 instead of AZ4620. Although both photoresists have similar characteristics, it has been found experimentally that AZ9260 is easier to bake and endures a temperature gradient without cracking. The cracking of the thick photoresist is a difficult problem, especially when the photoresist is on the top of the thin membrane where heat conduction occurs primarily through the top of the film through convection.

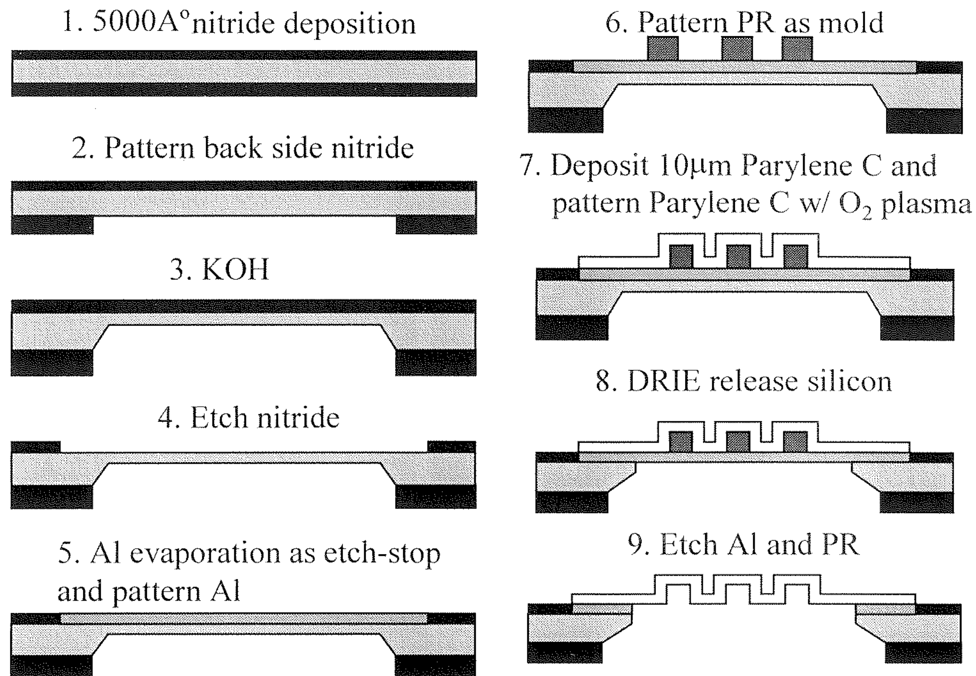

Fig. 3-8: The simplified fabrication steps for corrugated Parylene membrane

After the photoresist is successfully patterned, 10μm of Parylene C is then room temperature CVD deposited to be used as a fluid barrier to prevent leaking. Parylene C is then patterned and O_2 (400W, 400mtorr) plasma etched to define the desired pattern. This is a tedious step because the etching rate of Parylene C under 400W, 400mtorr O_2 plasma etching is around 1μm for every 6 minutes. Thus, 10μm of Parylene C would take around one hour to finish. Besides, because of the non-uniformity of the etching system, the wafer has to be rotated manually every 6 minutes to achieve acceptable uniformity. Finally, the frontside of the wafer is spun with photoresist and baked for 15 minutes at 100°C in a convection oven to prevent the cracking of the photoresist during the DRIE operation. Then the silicon and nitride on the backside of the wafer are etched away using DRIE until aluminum is reached. The aluminum is then etched using commercial Al

etchant. Then the wafers are diced and the photoresist is stripped away by immersion in acetone and IPA solutions.

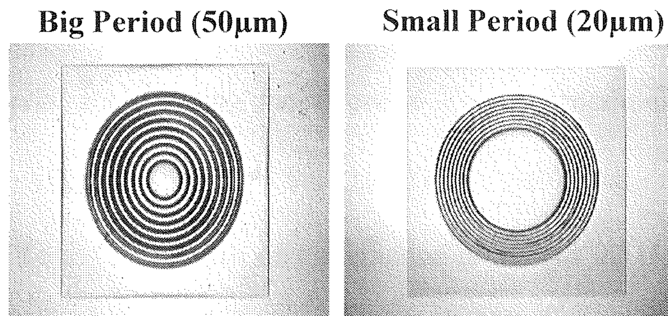

Fig. 3-9: Photos of finished corrugated Parylene/silicone composite membrane

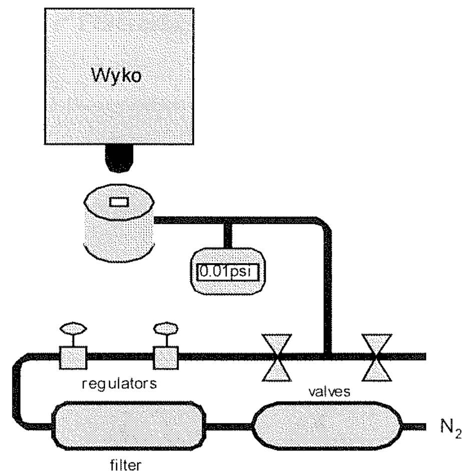

Fig. 3-10: Bulge-test setup used for measuring membrane performance

The finished membranes as shown in Fig. 3-9 consist of two different corrugation periods (50μm and 20μm). The membrane size is 4mm*4mm and all consist of nine turns of corrugation. The membranes are then tested using the bulge-test method outlined in section 2.4 with the setup shown in Fig. 3-10. The measured data are then shown in Fig. 3-11. From Fig. 3-11, it is clear that the corrugation does soften the membrane and thus loosen the requirement and the operating temperature for thermopneumatic operations. The membranes with big periods and small periods both only requires pressure of around

1psi to reach 80μm of the deflection which is considered as the operation point of the thermopnumatic valve here. Moreover, the composite silicone/Parylene membrane fabricated by squeegee silicone into the silicon cavity as outlined by section 3.2.1 has similar load-deflection curve of small-corrugation Parylene diaphragm and implied that the dominant material for deciding the effective Young's modulus is 10μm-Parylene rather than 400μm-silicone. That is because the Young's modulus of Parylene is around 4.5GPa while the Young's modulus of the silicone is around 0.51Mpa which differs 4 orders of magnitude.

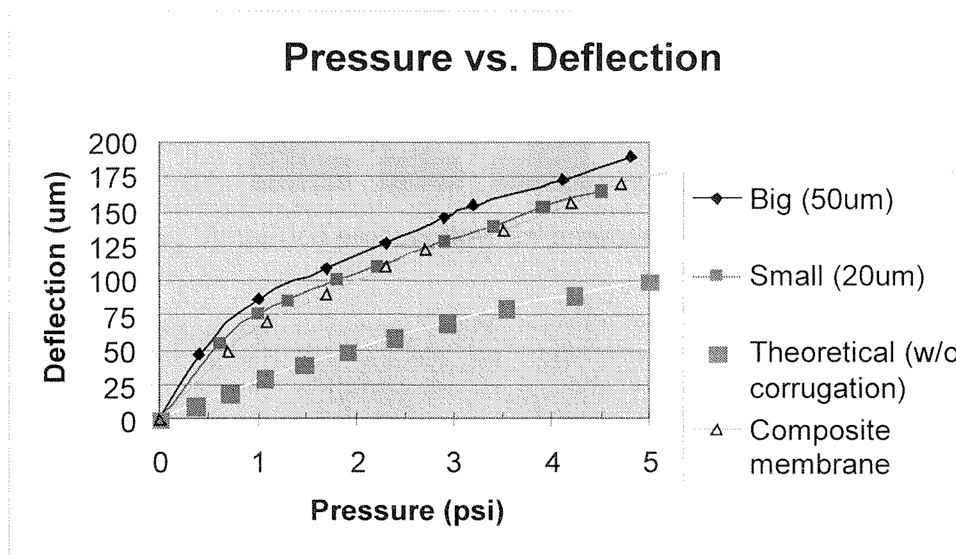

Fig. 3-11: Pressure-Deflection relationship for Parylene/silicone composite membrane

3.4.4 Improved Valve-Seat for packaging and Channel characterization

The improved valve seat is intended to simplify the packaging process. The fabrication of this valve seat is straightforward shown in Fig.3-12 with Deep-Reactive-Ion-Etching. First, the front side of wafer is patterned with AZ4620 photoresist and etches in DRIE for 800 loops until 350μm is reached. Then the backside of the wafer is again patterned with AZ4620 and etches in DRIE until the front and back are connected.

As discussed earlier, the fluidic channel is actually formed in the recess automatically created by surface tension when the silicone is cured. Therefore, no extra provision has to be made separately for the channel. Shown in Fig. 3-13 is the alpha-step surface profile scanning across the silicone diaphragm after curing. The curve shows the automatically formed recess is around 90μm and that is the reason the design is targeted at this range.

1. DRIE etch front side hole and channel

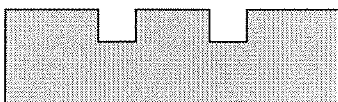

2. DRIE etch back side hole

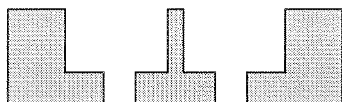

Fig. 3-12: Simplified process flow for improved valve seat

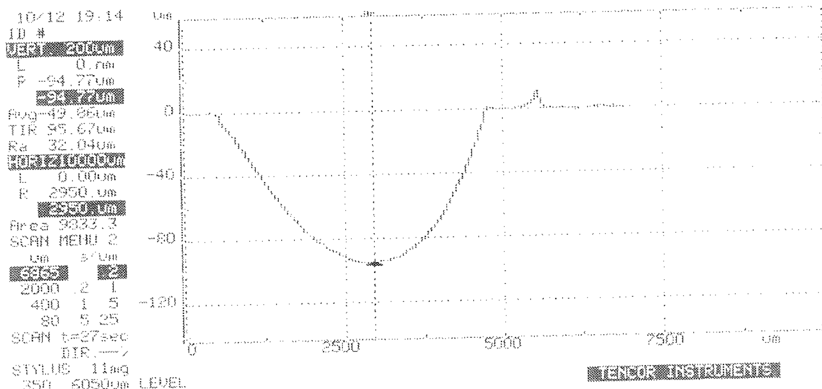

Fig. 3-13: Alpha-step scanned surface-profile on silicone membrane

The channel formed by manually gluing the valve seat and silicone membrane as part (1)/(2)/(3) shown in Fig.3-1 is tested with various inlet pressures. The target for this microvalve is to control gas in the flow range of several slpm. As shown in Fig. 3-14, the flow rate shows a linear relationship with the inlet pressure, and the flow rate range is at

the targeted range. Moreover, by varying the inlet/outlet size experimentally at the valve seat, the conclusion is that the flow rate is limited by the size of the inlet/outlet rather than the channel size.

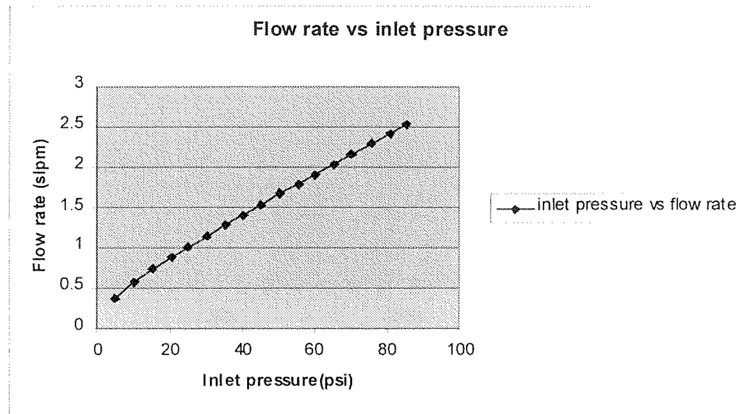

Fig. 3-14: Flow rate of the channel formed by the corrugated membrane at various pressure

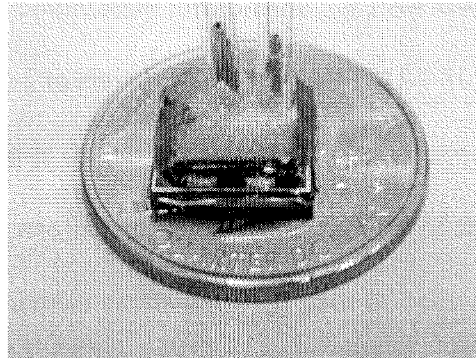

Fig.3-15: The finished device sitting on a quarter

3.5 Testing of thermopneumatic microvalve

The finished device as shown in Fig. 3-15 is around 1cm*1cm with thickness around 3mm. The valve is tested using N_2 as the gas. The power is calculated by the product of current and the voltage; flow rate is measured by the flowmeter (Cole Parmer,

Model 32916, 0.01slpm resolution). Pressure is measured by pressure sensor (Omega, Model HHP 4100, 0.1psi resolution).

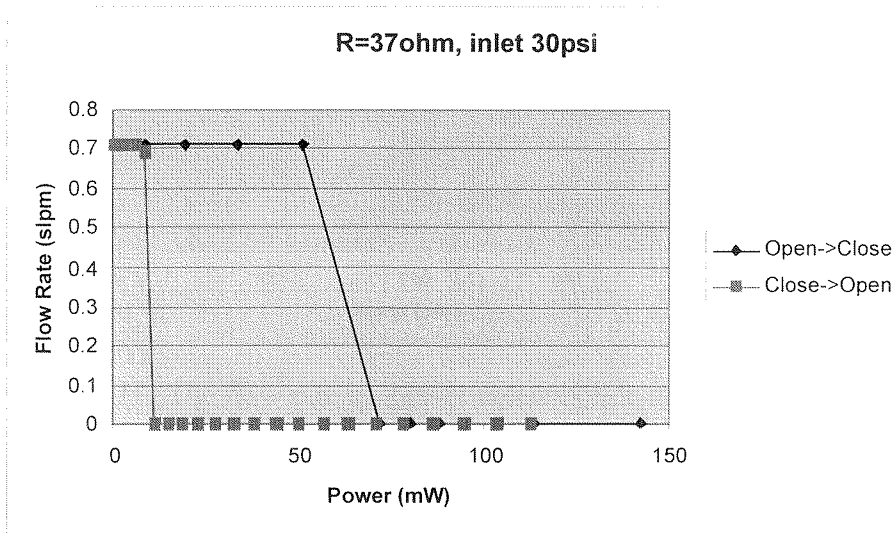

Fig. 3-16: The simple ON-OFF testing on microvalve (it requires 72mW to close)

The simple ON/OFF data is shown in Fig. 3-16; the fabricated microvalve required around 70mW to completely turn off the gas flow with inlet pressure 30psi. This result is not low compared to those published in [3, 18]. However, the reason for this higher power consumption is due to the thicker Parylene layer used in the experiment to prevent the liquid leaking and hence increase the rigidity of the membrane. Furthermore, it is clear that a huge hysteresis exists over the path of open to close and close to open. The most likely reason is that the substrate has to be heated up prior to closing the valve; and this process consumes power [18]. While the valve is heated up and thus the substrate, it would require less power to keep the membrane deflected to close the valve. Thus, the power required to maintain the valve at the off-flow condition is much less than the power needed initially to turn off the flow.

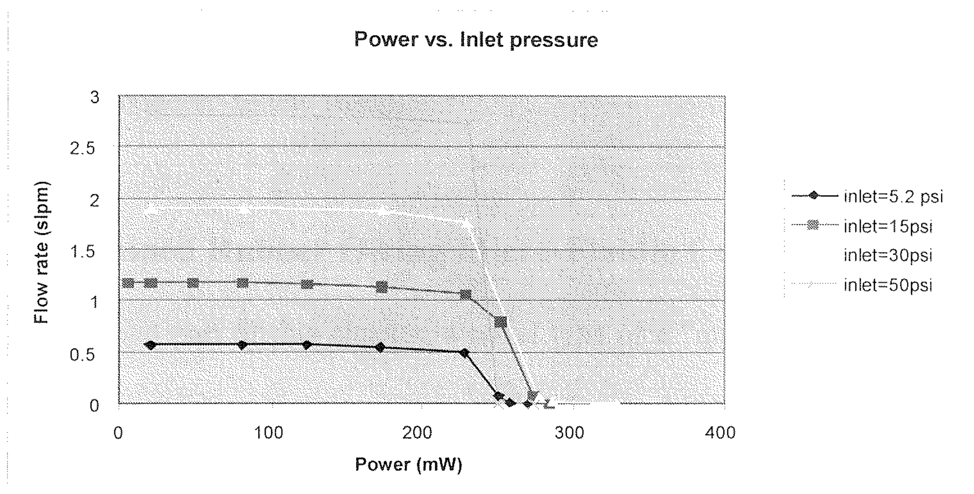

Fig.3-17: The flow rate vs. power consumption at different inlet pressures

Experiment is also conducted to investigate the power consumption required for different inlet pressure. As shown in Fig. 3-17, the power required to turn off the flow change very little with the inlet pressure. The power consumption in Fig. 3-17 is significant higher than the result shown in Fig. 3-16. The reason for this is due to the manual assembly of the valve. Actually, it seems that the higher the inlet pressure, the lower the power consumption required to turnoff the flow. The higher power consumption at low inlet pressure can be explained by the fact that when the inlet pressure is low, the cavity is free to expand and thus the contact area between the membrane and the valve seat and this contact causes higher heat loss due to the high thermal conductivity of silicon.

In the first part of the chapter, a silicone/Parylene composite membrane is demonstrated to be used for thermopneumatic microvalve applications. The microvalve with a minimum of 70mW power consumption is capable of controlling the flow at several slpm range with inlet pressure up to 50psi. In the second part of this chapter, silicone rubber O-ring microfluidic coupler will be demonstrated to simplify the

packaging of the microvalve. The final goal is to achieve a universal fluidic board to couple the micro to macro fluidic world.

3.6 Micromachined Rubber O-ring Micro-Fluidic Couplers

In the second part of this chapter, a novel type of a "quick-connect" for micro-fluidic devices realized by a simple silicone-rubber O-ring MEMS coupler is described. As shown in this work, the proposed O-ring couplers are easy to fabricate and utilize, they are reusable, and they can withstand high pressure (>60psi) and provide good seals. Results from both the leak rate test and pull-out test are presented, demonstrating the functionality of the O-ring couplers.

In the expanding field of microfluidics, it is clear that many micro-fluidic handling devices such as the micro-pump, micro-valve, and micro-filters have been demonstrated. However, for a successful micro-fluidic system, it is still a very challenging task to connect the external macro-fluidic reservoir to a micro-fluidic system. This is shown in the rising interest in the development of fluidic interconnects. There are still no working MEMS "quick-connects" yet. Some of the micro-fluidic interconnection schemes that have been proposed will be compared in the next section.

3.6.1 Previous Demonstarted Coupling Methods

Mechanic Clamping or Bonding

The most common method used for fluidic boards in micromachining is to use mechanical parts to clamp many fluidic components [23]. Some researchers have explored bonding technologies such as silicon to silicon and silicon to quartz to reduce

the complexity of the packaging. However, the tube itself is still mechanically clamped and glued. Thus, this method is inherently bulky, labor-consuming and thus not mass-producible.

Wet-chemical etching

At prototype stage in most laboratories, the fluidic coupling of MEMS devices such as valves, pumps, and mixers is still done by etching the fluidic port into the silicon wafer, whether anisotropically or isotropically [24]. The most common way is to etch the fluidic port from backside of the wafer using KOH solution and, therefore, because of its anisotropic etching characteristics, a lot of area has to be wasted, and a high-density of fluidic ports can not be achieved. Although this can be overcome by using new techniques such as DRIE to increase the density of fluidic ports, glue is still used to fasten the external tubes with larger diameters than the fluidic ports to the fluidic ports on silicon substrate. Therefore, not only a lot of area has been wasted but the glue is often leaked into the fluidic channel, and decreasing the yield of the devices. Therefore, to achieve higher yield in fluidic packaging, a new method without using glue has to be found.

Microfluidic Coupler with PDMS Gasket

Kovacs *et al.* [25] at Stanford University has demonstrated a reusable silicon/plastic fluid coupler with a polydimethylsiloxane (PDMS) gasket formed in a deep reactive ion etched (DRIE) silicon mold. The plastic press fittings are fabricated using injection molding of polyoxymethylene (POM) plastic. The PDMS gasket which is placed at the silicon/plastic interface is fabricated with a DRIE etched silicon mold. To

align and hold the plastic parts in place, the silicon/Pyrex dice have vias fabricated by DRIE and ultrasonic drilling, respectively. After insertion, the couplers' alignment posts are melted with a heat-staking tool as the temperature reaches 250°C, thereby securing the posts within the vias. Experiments show this sealed fluidic coupling with a PDMS gasket can withstand pressures up to 250psi compared to one without gaskets, which can only withstand pressure up to 60psi. Furthermore, it is also demonstrated that the pull-out force can be up to 2N.

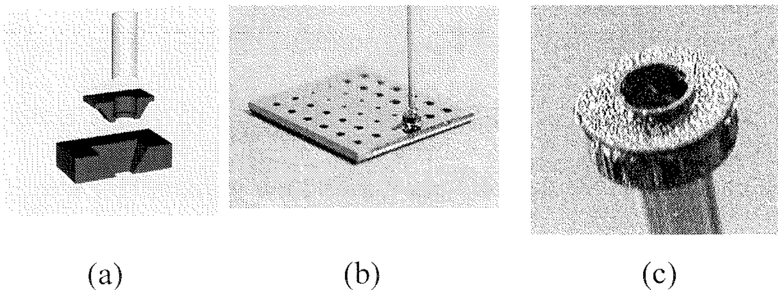

(a) (b) (c)

Fig. 3-18: Schematics (a), the photo (b) and close-up photo (c) of microfluidic coupler proposed by *Meng et al.*

However, to utilize this coupler, many parts have to be injection molded, and the manual alignment and assembly is still critical. Therefore, this method would be difficult for applications requiring lots of fluidic inlets/outlets. However, the coupling achieved by this method could reach high pressure which could be beneficial for some specific applications.

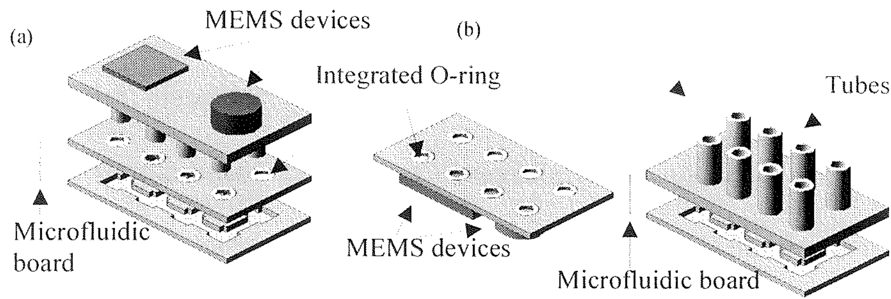

Fig. 3-19: Schematic view of the O-ring coupler application
(a) A multi-port micro-fluidic device is plugged into a micro-fluidic board with O-ring couplers.
(b) A MEMS micro-fluidic device with O-ring coupler is plugged into a micro-fluidic board.

Silicon Truncated Pyramidal Coupler

Meng *et al.* [26] have demonstrated both wet-etching and DRIE to create the two-part couplers shown in Fig.3-18. The peek tube is first glued into the male parts created by DRIE or KOH etching with corner compensation. Then the tube with the male part is glued into the pre-etched female part on the fluidic board that has micromachined parts pre-fabricated on top. By using this two-part methods, the yield of the coupling is greatly increased. Experimentally, the test demonstrated that the assembled couplers can withstand up to 1300psi. However, this method required initial batch fabrication of the male parts, and glue is still required. Therefore, this method is not reusable and thus is not an ideal fluidic-circuit board architecture. However, this method would enhance the yield of packaging of a fluidic board and can be used to extreme high pressure.

Therefore, to achieve lab-on-the-chip concepts, a new technology that reduces the complexity of the packaging has to be developed to increase the overall yield. In the following sections, a new quick-connect that emphasizes reusability and good seal (minimum 10psi) will be developed and characterized, targeted for our microvalve applications described earlier in this chapter. Therefore, the demonstration of a quick-

connect coupler will be used to connect a stainless steel tube size around 860μm and a silicon chip with pressure up to 60psi. The final target of this fluidic coupler is to demonstrate a fluidic board that different microfluidic components can be plugged into and in which they can be replaced easily as shown in Fig. 3-19, similar to a conventional electronic circuit board.

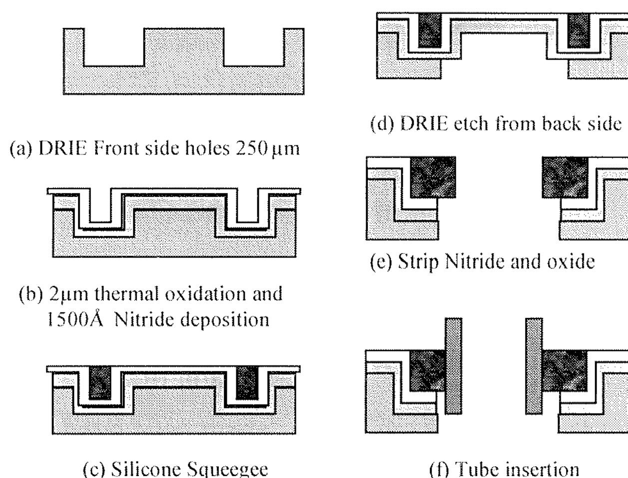

Fig. 3-20: Simplified process for making rubber-O-ring fluidic coupler

3.6.2 Design and Fabrication Process

The initial design of the rubber O-rings are for two sizes of capillary tubes (O.D. 860μm and 640μm). The process shown in Fig. 3-20 starts with etching of the silicon substrate to a depth of 250μm by deep reactive ion etching (DRIE) to define the O-ring mold shape. Then a 2.5μm thick SiO_2 layer is thermally grown to be used as the mask for later DRIE etching. A 1μm thick layer of Silicon Nitride (SiN_x) is then deposited on top of the SiO_2 to serve as the adhesion layer between the substrate and the silicone rubber. This step is necessary because the silicone rubber does not have very good adhesion on SiO_2. After nitride deposition, the silicone rubber is squeezed into the DRIE cavities to form the O-ring. The process is then followed by DRIE etching from the backside of the

substrate to form the backside hole. The oxide and nitride membranes are then stripped off in buffered hydrofluoric acid (BHF) and SF_6 plasma.

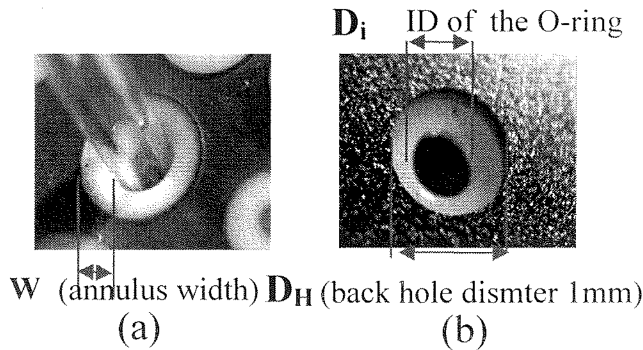

Fig. 3-21: (a) A capillary tube plugged into the tube (front side)
(b) O-ring is viewed from back

The finished O-ring dimensions are shown in Fig. 3-21. Various 250μm-thick silicone-rubber O-rings have been made. All of the O-rings have the same annulus width (500μm) but with different IDs ranging from 400 to 700μm. A schematic view of the couplers is shown in Fig. 3-22a. After a tube is inserted, the rubber O-ring deforms to establish a good seal, as pictured in Fig. 3-22.

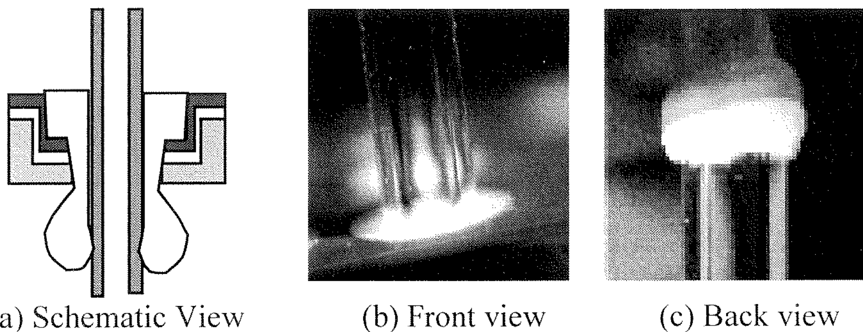

Fig. 3-22: View of the assembled rubber O-ring and tubes inserted in O-ring

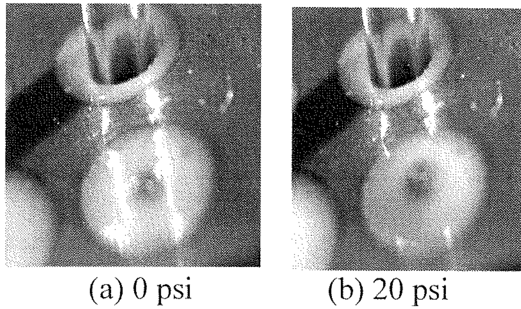

Fig. 3-23: Pressure test (a) at 0 psi (b) at 20 psi

3.6.3 Experimental Characterization

In order to characterize the performance of the rubber O-ring couplers, two of the most important tests are performed – leak rate tests and pull-out force measurements. First, Figure 3-23 shows the O-ring seals under pressure at 20 psi. There is no observable shape change of the O-rings found, which indirectly proves the mechanism of sealing we proposed in Fig.3-21a. In short, a good seal is promoted by rubber deformation so that the effective rubber-tube contact thickness is much larger than the original rubber thickness (250μm).

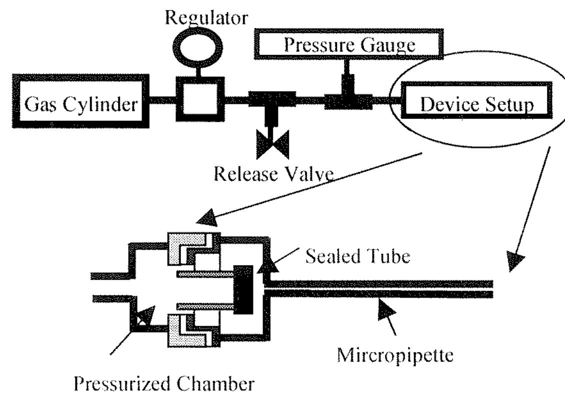

Fig. 3-24: Experimental setup for leak rate measurement

After the hypothesis was confirmed, subsequent tests were performed on the O-rings, including the leak test and pullout test. The experimental setup of the leak test is illustrated in Fig. 3-24. A blocked tube is first inserted into the O-ring chip. The front

side is then sealed with a 10μl micropipette (filled with water to serve as a positive-displacement leak monitor). A pressure gauge is connected to monitor the backside chamber.

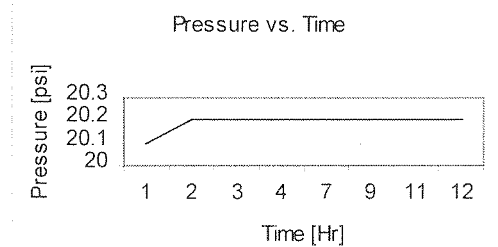

Fig. 3-25: The tube under 20psi remains sealed over 12 hrs

The results of the leak test for 860μm-OD tube coupled to a 400μm-ID O-ring is shown in Fig. 3-25. A good seal was maintained over 12 hrs with no measurable pressure drop (constant at 20.2psi). The same leak tests have been performed on the other O-ring couplers, with the results given in Table 3-3. We conclude that tight seals can be achieved if the O-ring is properly designed (i.e., the ID of the O-rings is smaller than the tube OD). The experimental setup shown in Fig. 3-24 can only withstand pressures up to 60psi, with good seals achieved up to that pressure.

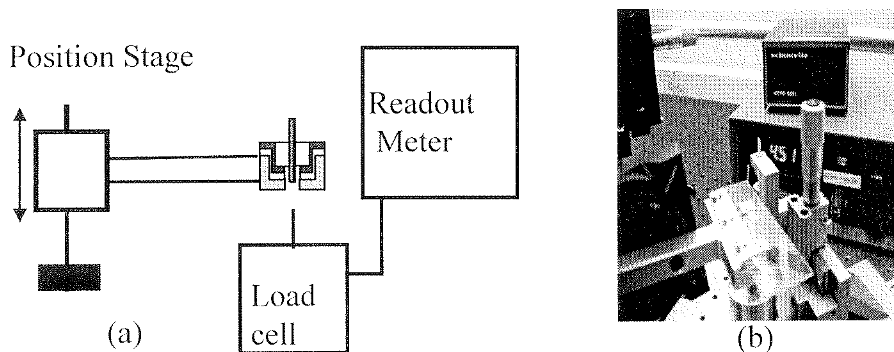

Fig. 3-26: Experimental setup of pull-out test
(a) Schematic view (b) Photo of setup

Table 3-3: Leak rate tests on rubber O-ring with different inner diameters

Tube O.D. (μm)	Inner Diameter of rubber O-ring (μm)			
	400	500	600	700
860	Non-detectable	Non-detectable	Non-detectable	Non-detectable
640	Non-detectable	11μl/min @20psi	Infinite	Infinite

Non-detectable (<<0.1μl/min @20psi)

Infinite (>>10μl/min @0.5psi)

The experimental setup for the pullout test is shown in Fig. 3-26. A position stage is used to pull-out the tube from the O-ring couplers while the load cell is used to measure the resistant force when the position stage moves downward to push-out the tube. As the position stage slides downward and begins to push the tube, the reading on the load cell starts to increase. However, when the tube starts to move relative against the O-ring coupler, the force starts to decrease due to the fact that the kinematic friction coefficient is smaller than the static friction coefficient. Hence, the maximum reading on the load cell before the tube sliding is recorded in this experiment.

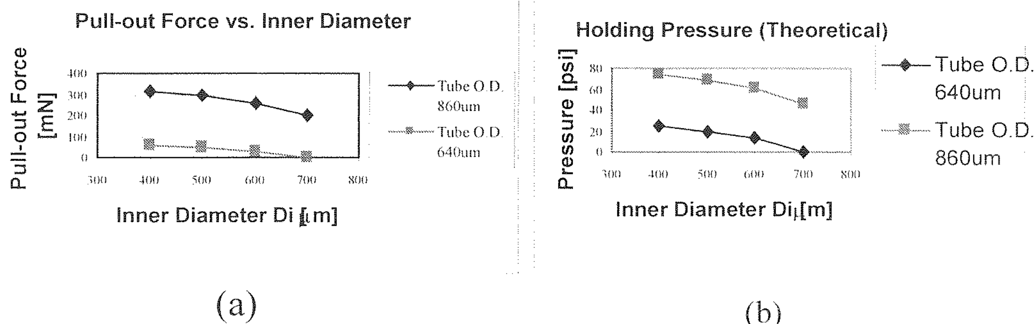

(a) (b)

Fig. 3-27: The pull-out test results on rubber O-ring
(a) Pull-Out Force vs. Inner Diameter of rubber O-rings
(b) The Theoretical Holding Pressure calculated from (a)

The results of pull-out measurements are shown in Fig. 3-27. The results suggest that the force required to pull the tube out of the O-ring decreases as O-ring ID increases. Figure 3-27b shows the calculated theoretical holding pressures converted from the data in Fig. 3-27a. A wide range of holding pressures (all >10psi) has been achieved with the maximum around 80psi for the tube with OD 860µm against the O-ring ID 400µm. And all the results agree with our leak test data.

Reliability Test on O-ring Couplers

Finally, the pull-out tests were repeated several times to simulate the reusability of the devices (Fig. 3-28). We observe that stabilization of the pull-out force is reached after several cycles (showing no further decay), indicating reliability of the devices. A repetition test (>200 times) has also been performed, showing good adhesion between rubber and nitride sidewall. In a few instances, cracking of the O-rings around the inner diameter of the rubber membrane was observed. This problem is expected to be easily solved by using different silicone rubbers as O-ring materials.

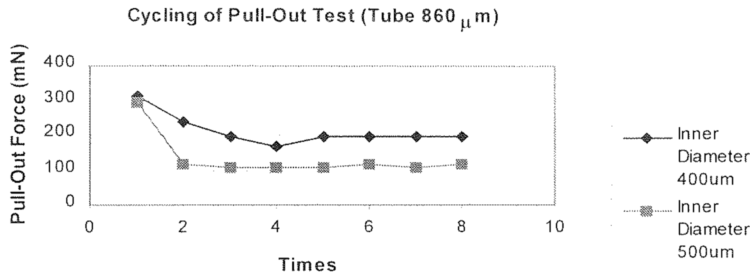

Fig. 3-28: The reliability test of rubber O-ring

In this section, a micromachined rubber O-ring coupler has been designed, fabricated and tested. The result shows the coupler is reusable and can maintain good seal as high as 60psi.

3.7 Conclusion

In this chapter, a micromachined, normally open thermopnuematic microvalve has been designed, fabricated, and characterized for microfluidic applications targeted for controlling gas flow at slpm range. The low Young's modulus and good solvent barrier properties are used to make Parylene/ Silicone composite diaphragm. Minimum power of 73 mW is required to turn off the gas flow up to 70psi. In the second part, a reusable microfluidic rubber O-ring coupler was also designed and characterized to simplify the packaging of the microvalve demonstrated in the first part of the chapter. The demonstrated rubber O-rings have negligible leak rates up to 60psi and are reusable.

3.8 References

[1] M. Shikida, K. Sato, S. Tanaka, Y. Kawamura, and Y. Fujisaki, "Electrostatically Driven Gas Valve with High Conductance," *Journal of MicroElectroMechanical Systems*, vol.3, pp.76-80, 1994.

[2] P. W. Barth, C. C. Beatty, L. A. Field, J. W. Baker, and G. B. Gordon, "A Robust, Normally Closed Silicon Microvalve," Proceedings of the Solid-State Sensor and Actuator Workshop, Hilton Head Island, SC, June 13-16, 1994.

[3] M. J. Zdeblick, R. Anderson, J. Jankowski, B. Kline-Schoder, L. Christel, R. Miles, and W. Weber, "Thermopneumatically Actuated Microvalves and Integrated Electro-Fluidic Circuits," Proceedings of the Solid-State Sensor and Actuator Workshop, Hilton Head Island, SC, June 13-16, 1994.

[4] C. Grosjean, "Silicone MEMS for Fluidics," in *Electrical Engineering*, Pasadena, CA, California Institute of Technology, 2001.

[5] R. Zengerle, S. Kluge, M. Richter, and A. Richter, "A Bidirectional Silicon Micropump," Proceedings of the IEEE 1995 Micro Electro Mechanical Systems Workshop (MEMS '95), Amsterdam, Netherlands, 1995.

[6] H. D. Goldberg, R. B. Brown, D. P. Liu, and M. E. Meyerhoff, "Screen Printing: A Technology for the Batch Fabircation of Integrated Chemical-Sensor Arrays," *Sensors and Actuators B*, vol.21, pp.171-183, 1994.

[7] J. Evans, D. Liepmann, and A. P. Pisano, "Planar Laminar Mixer," Proceedings of the IEEE 1997 Micro Electro Mechanical Systems Workshop (MEMS '97), Nagoya, Japan, 1997.

[8] P. Dario, M. C. Carrozza, A. Benvenuto, and A. Menciassi, "Micro-systems in biomedical applications," *J Micromech Microeng*, vol.10, pp. 235-244, 2000.

[9] A. Manz, C. S. Effenhauser, N. Burggraf, D. J. Harrison, K. Seiler, and K. Flurri, "Electroosmotic Pumping and Electrophroetic Separations," *Journal of MIcromechanics and Microengineering*, vol.4, pp.257-265, 1994.

[10] A. Richter, A. Plettner, K. A. Hofmann, and H. Sandmaier, "A Micromachined Electrohydrodynamic (EHD) Pump," *Sensors and Actuators A*, vol. 29, pp.159-168, 1991.

[11] E. Colgate and H. Matsumoto, "An Investigation of Electo-Wetting-Based Microactuation," *Jounal of Vacuum Science Technology*, vol. A8, pp.3625-3633, 1990.

[12] M. Madou, *Fundamentals of Microfabrication*. Boca Raton, New York, CRC Press, 1997.

[13] X. Yang, "Micromachined Silicone Rubber Membrane Valves for Fluidic Applications," in *Electrical Engineering*. Pasadena, CA, California Institute of Technology, 1999.

[14] K. Peterson, P. Barth, J. Poydock, J. Brown, J. M. Jr., and J. Bryzek, "Silicon Fusion Bonding for Pressure Sensors," Technical Digest, IEEE Solid State Sensors and Actuators Workshop, Hilton Head Island, South Carolina, USA, June 1988.

[15] W. H. Ko, J. T. Suminto, and G. J. Yeh, "Bonding Techniques for Microsensors," *Micromachining and Micropackaging of Transducers*. Amsterdam, Elsevier Science Publishers B.V., 1985.

[16] M. Esashi, "Integrated Micro Flow Control Systems," *Sensors and Actuators A*, vol. 21-23, pp. 161-167, 1990.

[17] M. A. Brook, *Silicon in Organic, Organometallic, and Polymer Chemistry*, John Wiley & Sons, Inc., 2000.

[18] X. Yang, C. Grosjean, Y.-C. Tai, and C.-M. Ho, "A MEMS Thermopneumatic Silicone Membrane Valve," Proceedings of IEEE Workshop on MicroElectroMechanical Systems (MEMS '97), Nagoya, Japan, 1997.

[19] "High-Barrier films look strong through 1996," *Packaging (Boston, Mass,)*, vol. 37, pp. 92, 1992.

[20] J. R. Webster, "Monolithic Structures for Integrated Capillary Electrophoresis Systems," Ph.D. thesis, University of Michigan, 1999.

[21] http://www.scscookson.com/indexus.htm

[22] J. H. Jerman, "The fabrication and Use of Micromachined Corrugated Silicon Diaphragms," *Sensors and Actuators A*, vol. 23, pp. 988-992, 1990.

[23] D. VerLee, A. Alcock, G. Clark, T. M. Huang, S. Kantor, T. Nemcek, J. Norlie, J. Pan, F. Walsworth, and S. T. Wong, "Fluid Circuit Technology: Integrated Interconnect Technology for Miniature Fluidic Devices," *Hilton Head '96*, pp.9-14, 1996.

[24] D. Jaeggi, B. L. Gray, N. J. Mourlas, B. P. v. Drieenhuizen, K. R. Williams, N. I. Maluf, and G. T. A. Kovacs, "Novel Interconnection Technologies for Integrated Microfluidic sytems," *Hilton Head '98*, pp.112-115, 1998.

[25] N. J. Mourlas, D. Jaeggi, N. I. Maluf, and G. T. A. Kovacs, "Reusable Microfluidic Coupler with PDMS Gasket," *Transducers '99*, pp. 1988-1989, 1999.

[26] E. Meng, S. Wu, and Y. C. Tai, "Micromachined Fluidic Couplers," *Fourteenth IEEE International Conference on Micro Electro Mechanical Systems (MEMS '01)*, 2001.

CHAPTER 4

BrF_3 Dry Release Technology for Large Freestanding Parylene MEMS

Abstract

In this chapter, the technical challenge to use Parylene as a surface micromachined structural material will be addressed. Stiction, which remains a challenging problem for polysilicon micromachining, prevails in the case of using low Young's modulus Parylene as structural material. A new method, which combines wet chemical and dry vapor etching, is used to solve the stiction problem by drying the Parylene microstructure in wet solutions. Many large area Parylene microstructures (>mm*mm) are demonstrated using this technology and will be used as the foundation technology for Chapter 5 to build electrostatic actuators.

4.1 Introduction

Parylene is a promising MEMS structural material because it has many advantages over traditional MEMS materials as discussed earlier in Chapter 2. For example, Parylene is deposited using a room temperature CVD process, and the process can be CMOS compatible. It is widely available, and the cost of the material and processing is fairly low. In the past few years, application of Parylene in MEMS devices

[1, 2] has been investigated. A surface micromachining technology [1] has been developed with photoresist as the sacrificial layer. The structures are freed by dissolving the sacrificial photoresist layer in acetone at room temperature. So far, many Parylene MEMS structures and devices such as channels [1], diaphragms [3], and valves [2] have been demonstrated.

Since Parylene has a fairly low Young's modulus, the bending of the structures due to gravity could be significant. Assuming a Young's modulus of 4 GPa, the deflection of 1 mm long cantilever beams with thickness from 1 μm to 5 μm with 4.5 μm air gap is calculated and plotted as shown in Fig. 4-1. It can be seen from the calculation that the gravitational effect can be negligible (<1 μm for 1mm beam) in the case of 4.5 μm thick Parylene structures. Therefore, Parylene, despite its low Young's modulus, is suitable for integration into MEMS microstructures with CMOS circuitry on the same single chip.

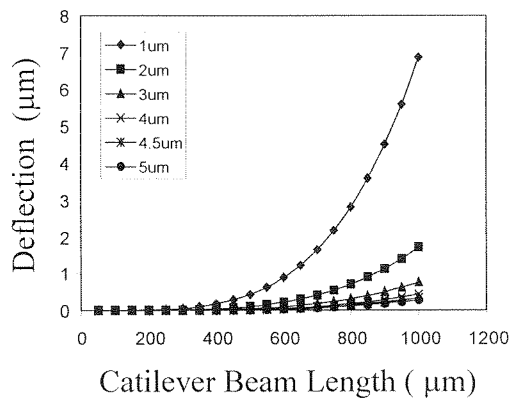

Fig. 4-1:Theoretical calculation of beam deflection due to gravity

4.2 Selection of the Sacrificial Layer Material

For surface micromachined processes, the selection of the sacrificial material is one of the most important steps. First, the previous fabrication steps have to be compatible with the sacrificial processes. For example, aluminum is usually not used as a sacrificial layer on post-CMOS processes because the releasing steps, if not taken care of properly, could damage the metal lines used in integrated circuits. Second, the remaining processes have to be compatible with the sacrificial layer removal processes. For example, the aluminum sacrificial layer can not be used for polysilicon surface micromachined processes because the temperature of LPCVD processes would melt the aluminum used for sacrificial layer as discussed in Chapter 2. Third, the releasing agent has to be able to etch the sacrificial layer at an applicable rate without creating damage for both MEMS material and underlying materials such as electronics.

There has recently been a surging interest on post-CMOS MEMS. The reason for the post-CMOS process is that the electronics can be readily designed and fabricated using foundry services, and the desired material can then be added later on to integrate the MEMS structure with electronics as earlier discussed in Chapter 2. Parylene, which is the main focus in the thesis, has attracted great attention for post-CMOS integration because of its room-temperature deposition and low temperature processing advantages. Accordingly, the focus in this chapter is to develop the processes for building Parylene surface micromachined structures ideally on CMOS wafers. This section will focus on the selection of the sacrificial material for Parylene MEMS.

4.2.1 LTO/PSG as Sacrificial Material

CVD silicon dioxide is by far the most mature sacrificial layer material used in MEMS research and industry due to its fast etching rate and selectivity over polysilicon structural material. However, the most important reason lies in its low deposition temperature. CVD silicon dioxide is usually deposited on the wafer from the vapor phase reaction of silane (SiH_4) with oxygen at a relatively low temperature (300°C to 500°C) and low pressure. In electronics, CVD silicon dioxide is usually used for electrical insulation, diffusion/ion implantation masks, and gettering impurities. In micromachining, LPCVD silicon dioxide, often called Low Temperature Oxide (LTO), and its derivative Phosphorous-doped glass (PSG), is often used for sacrificial layers due to their fast etching rates[4]. Several successful products including ADXL50 from analog devices have used LTO as the sacrificial material in their processes. MCNC also demonstrated the MUMPs foundry services using LTO to realize the 3 layer polysilicon MEMS processes.

However, the application of LTO/PSG for sacrificial layers in Parylene processes has encountered many difficulties. First of all, although the etching rate of the LTO is considerably fast, the etching time is still relatively long for releasing channels longer than 5mm[5]. Moreover, the buffered hydrofluoric acid (BHF) used for etching LTO/PSG would eventually attack the Parylene/silicon nitride interface and even the Parylene/Parylene interfaces. Therefore, these approaches have been abandoned for further investigation especially for this reason.

4.2.2 Metals as Sacrificial Material

Metals such as aluminum and copper have been investigated for their use as the sacrificial layer material on post-CMOS wafers[6, 7]. Aluminum is usually sputtered or e-beam evaporated to achieve films thicker than a few microns. Thermal-evaporation is seldom used because the temperature of the wafer would get very high and thus prevent the placement of any Parylene layer underneath the sacrificial layer. The aluminum layer, which is usually etched using a HCl solution, does not damage the Parylene material. However, aluminum is not used because for most of the CMOS interconnections, aluminum is still the dominant material.

Electroplated copper is a widely available material since it is a well-understood process. However, electroplated material is often rough, and without controlling the current and disposition rate well, the roughness is often intolerable. For example, for a 6 μm thickness sacrificial layer thickness, the roughness can be on the order of 1 μm, posing a significant inconvenience for various MEMS structures that require a smooth surface.

4.2.3 Polysilicon as Sacrificial Material

Polysilicon has recently attracted great attention to be used as the sacrificial layer. The primary reason includes the selectivity of polysilicon over LTO/PSG in BHF and the possibility of CMOS-compatible processes using other materials such as silicon nitride as the structural material. However, as was discussed in detail in Chapter 2, the releasing agents for polysilicon BrF_3 or XeF_2 do not have infinite selectivity over Parylene and, therefore, long exposure of Parylene to BrF_3 may cause damage as shown by Fig. 4-2.

The Parylene surface is exposed for 5 minutes to BrF_3 vapor, and the surface is roughened by the vapor, turning microscopically black. Moreover, the undercutting rate of polysilicon underneath the Parylene is slow, finally reaching a diffusion-limited region as described by Wang *et al.*[8]. Therefore, to create long channels or large-area structures, many etching holes have to be created, thus increasing the process difficulty. Moreover, for channel applications, the etching hole has to be sealed by another Parylene deposition, which inherently poses a challenge on lithographic steps to create the etching hole.

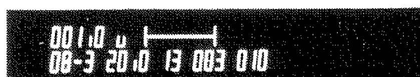

Fig. 4-2: SEM of Parylene surface after long BrF_3 exposure

Therefore, pure polysilicon sacrificial technologies are not explored and studied here. However, a combination of thin-polysilicon and thick-photoresist method will be used in this study to combine the wet-etching and dry-etching techniques to realize large area freestanding Parylene microstructures.

4.2.4 Photoresist as sacrificial Material

Photoresist lithographic steps are inherently low temperature processes. The typical temperature for soft-baking photoresist is around 100°C and can be further lowered to 60°C by prolonged low temperature baking. Several devices using photoresist

as the sacrificial layer have been demonstrated. The most successful example is the Digital Mirror Display (DMD) developed by Texas Instruments [9]. However, in most cases, the photoresist is hard-baked up to 200°C, then CMOS-compatible aluminum is evaporated and patterned as the structural material.

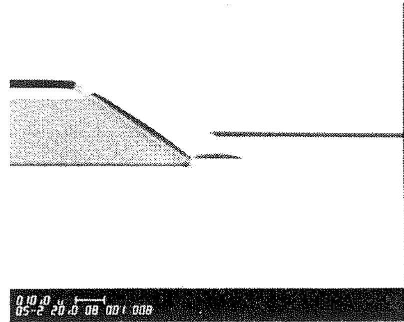

Fig. 4-3: SEM of Parylene microchannel using photoresist as sacrificial layer

Some researchers have also explored the possibility of combining photoresist and Parylene to make devices for genetic analysis applications [10]. Figure 4-3 shows a SEM photo of a microchannel using photoresist as the sacrificial layer and Parylene as the wall material. The photoresist is only soft-baked and used as the sacrificial layer, so the releasing step is relatively easy and is often done by immersion of devices into acetone solutions overnight. The potential problem of combining photoresist and Parylene is that to achieve a quick etching rate of photoresist in acetone, the photoresist can not be hard-baked for too long (>30 mins) at high temperatures (>120°C); otherwise, the photoresist etching processes will become too long and loses its advantage of being used as the sacrificial layer. However, the photoresist does have to be hard-baked to prevent further reflowing at subsequent processes. For example, Parylene is usually deposited after the formation of the sacrificial layer, followed by the evaporation/sputtering of metal in

succeeding steps. Without a hard-bake, the photoresist reflows and damages the Parylene/substrate interface.

In this chapter, we developed a dry release technology for making large freestanding surface micromachined Parylene MEMS. The technology is a two-step process that combines wet photoresist dissolution with dry silicon etching by bromine trifluoride (BrF_3), which will be discussed in detail in the next following paragraphs. With photoresist as the sacrificial layer that is dissolved using acetone, large Parylene MEMS devices can be achieved. A final dry release in BrF_3 vapor helps to free the devices.

4.2 Problems of Freestanding Parylene

Although much study has been focused on using Parylene for MEMS applications, large (> mm) freestanding Parylene MEMS structures have not been realized. This is because Parylene has a small Young's modulus (~4 GPa) compared to polysilicon (~130 GPa), and so during the final release in acetone, surface tension can easily pull the structure down to the substrate and cause stiction. The fabrication processes of testing structures for freestanding Parylene starts with 4'' silicon wafer with thermally grown oxide. First, the wafer is always primed with Parylene adhesion promoter, followed by a deposition of Parylene about 1 μm in thickness. The reason for this is twofold: first, without the first adhesion layer of Parylene, the Parylene usually has a weak interface with the substrate, and therefore acetone often leaks through the interface during the releasing stage. Second, Parylene is usually deposited on metal, silicon dioxide substrate or photoresist, and without the adhesion promoter, the adhesion is so weak that

oftentimes, the Parylene will peel off during the dicing steps while using dicing saw. After the adhesion layer is deposited, the photoresist sacrificial layer is photo-patterned and defined, and the structural Parylene layer is then deposited and patterned using O_2 plasma. The wafer is then spun with an additional photoresist layer for protection during the dicing processes, and the die is then released overnight using acetone.

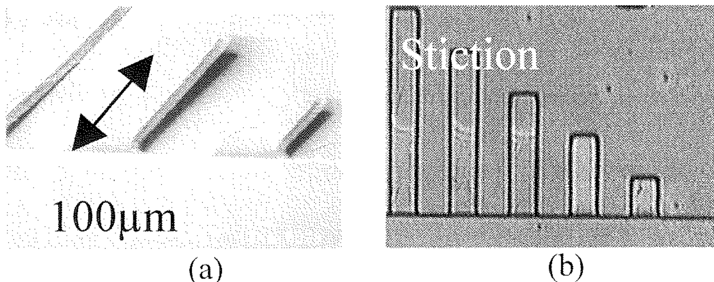

Fig. 4-4: Pictures of stiction of Parylene cantilever beams and diaphragms (a) SEM picture (b) microphotograph of cantilever beams

For example, our experiments (see Fig. 4-4 (a)) show that for 4.5 μm thick Parylene structures with a 4.5μm thick sacrificial layer, freestanding cantilever beams longer than 100 μm can not be made. The reason for this phenomenon is due to the low Young's modulus of the Parylene layer. The surface tension from drying processes can easily put down the cantilever beam and cause stiction to occur. Therefore, to make large freestanding Parylene MEMS, stiction processes have to be understood and resolved by avoiding or reducing the surface tension that causes stiction.

Many researchers have conducted detailed studies of stiction due to surface tension in micromachining. Mastrangelo *et al.* [11] has separately studied the stiction phenomena in two parts (i.e., mechanical collapse and adhesion to the underlying substrate). Tas *et al.* [12] proposed the theoretical limit for the detachment length of

cantilever beams using simple mechanical and surface energy balances, which will be described below and subsequently used in our experiment to explain the phenomena.

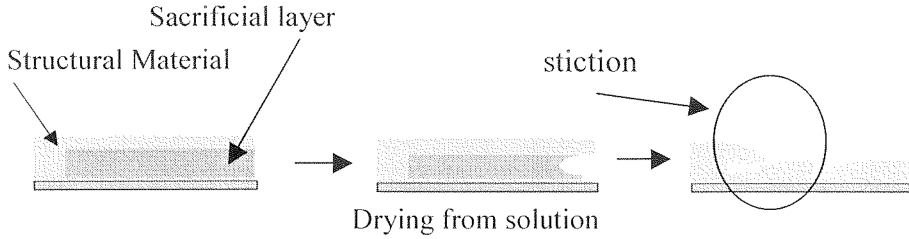

Fig. 4-5: Schematics of evaporation drying process: surface tension force bring the cantilever down in the drying process

As shown in Figure 4-5, stiction does not happen while the sample is being released. Instead, stiction occurs while the sample is dried in the air where the air/liquid interface exists. To understand the effect of surface tension, consider the free-body diagram shown in Fig. 4-6(a), which depicts the force-balance during the drying processes. First, if the contact angle θ_c is less than 90° at the liquid/air interface as shown in Fig. 4-6, the pressure inside the fluid will be lower than outside and a net attractive force between the plates will pull the plate down. An extra force F therefore is required to maintain the separation of the plates. This pressure ΔP_{la} at the air/liquid interface is often called the Laplace pressure and is given by $\Delta P_{la} = \frac{\gamma_{la}}{r}$ where γ_{la} is the surface tension of the air/ liquid interface and r is the radius of curvature of the meniscus. The attractive force required to maintain plate separation can be expressed as

$$F = -\Delta P_{la} * A = \frac{2A\gamma_{la}\cos\theta_c}{g} \qquad (4\text{-}1)$$

Moreover, the surface energy of air/liquid interface γ_{la} can be calculated using Young's equation from the free-body diagram of the steady liquid droplet on the solid surface:

$$\gamma_{sa} = \gamma_{sl} + \gamma_{la} \cos\theta_c \tag{4.2}$$

Thus, the total surface energy of the area between the plates can be calculated by adding the surface tensions of solid-air, solid-liquid and liquid-air interfaces. Assume the liquid is confined in a bridged area A_b, which is smaller than the total area A_T. For non-spreading liquids, the total surface energy can be expressed as

$$E_s = [A_T \gamma_{sa} - A_b(\gamma_{sa} - \gamma_{sl})] = [A_T \gamma_{sa} - 2A_b \gamma_{la} \cos\theta_c] \tag{4.3}$$

Thus, this drying process would provide an attractive force to pull down the cantilever.

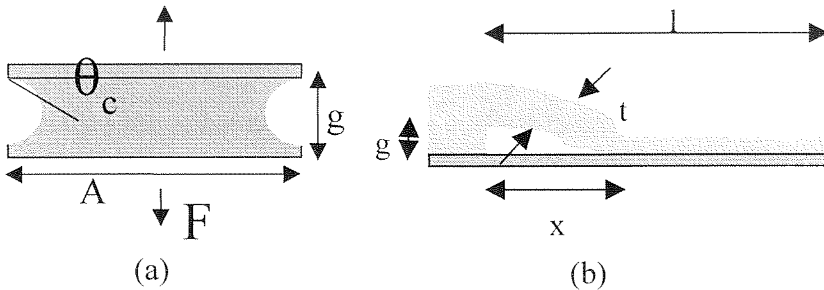

Fig 4-6: Schematics used to explain the Laplace pressure
(a) Laplace pressure from surface tension pull the cantilever down
(b) Coordinate used to calculate the detachment length

Now, let us consider the critical detachment length of beams and membranes. As shown in Fig. 4-6, as soon as the structure touches the substrate, the total surface energy is lowered. The structure would permanently stick to the substrate if during the peel-off the total energy of the system reaches a minimum. While the beam attaches to the substrate at a distance x from the anchor, the elastic energy stored in the cantilever is given by

$$E_m = \frac{Et^3 g^2 w}{2x^3} \tag{4.4}$$

where E is the Young's modulus of the cantilever beam material and w is the width of the beam. The surface energy as a function of the detachment length l-x is given by

$$E_s = C - \gamma_s (l - x) w \tag{4.5}$$

where γ_s is the adhesion energy per unit area (for our case γ_s can be replaced with $2\gamma_{la}\cos\theta_c$). In equilibrium, the total energy $E_m + E_s$ should reach a minimum. Thus,

$$\frac{\partial E_m}{\partial x} + \frac{\partial E_s}{\partial x} = 0 \tag{4.6}$$

and therefore, the critical length l_{crit} can be expressed as

$$l_{crit} = \left(\frac{3}{8} \frac{E t^3 g^2}{\gamma_s} \right)^{1/4} \tag{4.7}$$

For the case of the capillary force of a drying fluid, the final state is only reached if (i) the tip touches the substrate and (ii) the surface energy plus the deformation energy has a minimum for a detachment length x smaller than the beam length l. The critical length is expressed as

$$l_{crit} = \left(\frac{3}{16} \frac{E t^3 g^2}{\gamma_{la} \cos\theta_c} \right)^{1/4} \tag{4.8}$$

where

γ_{la}: the surface tension of air-liquid interface,

E: Young's modulus of the material,

θ_c: contact angle,

t: thickness of the cantilever beam,

g: air gap distance

Furthermore, assuming that the residual stresses and stiffening due to stretching can be neglected, the critical length of doubly supported beams is about 2.5 times larger and the critical radius of circular membrane is about 1.7 times larger. Based on this model, the theoretical limit of detachment length of cantilever beams with various thicknesses from

1μm to 5μm released with acetone and water is calculated and plotted in Fig. 4-7. The calculated detachment length for releasing in acetone and water are 84 μm and 56 μm, respectively. These small lengths would pose a big constraint on designing practical devices, which must be greatly increased to utilize the Parylene for any real Parylene MEMS applications.

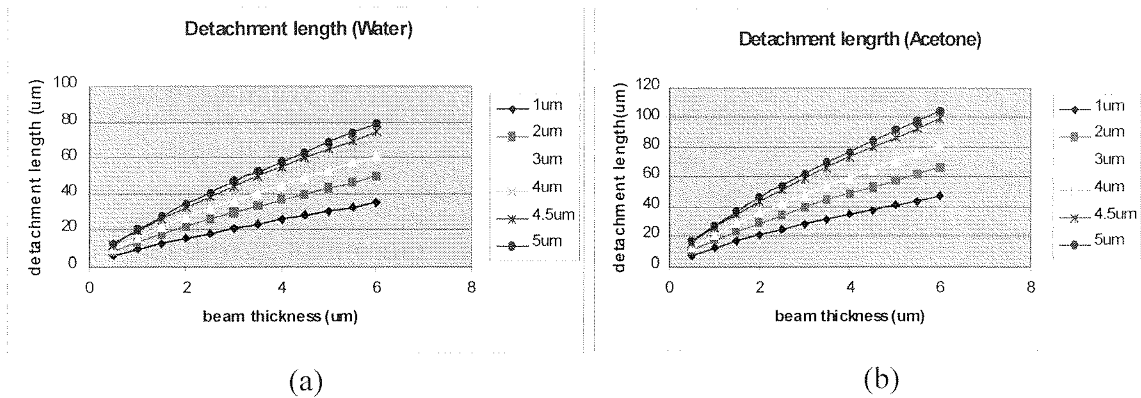

(a) (b)

Fig. 4-7: Theoretical calculation of detachment length for (a) water (b) acetone

4.4 Existing Methods for Dry-Release Freestanding Microstructures

In polysilicon micromachining, common approaches to avoiding stiction can be categorized as follows: (1) evaporation drying of the DI water, (2) evaporation drying with methanol, (3) sublimation drying with t-butyl alcohol, (4) sublimination drying with p-dichlorobenzene, (5) supercritical drying with CO_2 at the air/liquid, (6) Teflon anti-stiction layer (7) HF vapor phase etching, and (8) Self-assembled monolayers. All of these methods have been adapted for polysilicon MEMS by different researchers with varying degrees of success. This section is intended to review the existing technologies and try to apply them for Parylene.

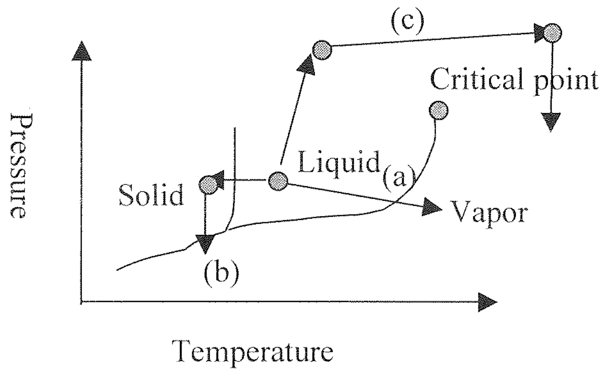

Fig. 4-8: Schematics of different drying processes
(a) Evaporative drying (b) sublimation drying (c) supercritical drying

Evaporation drying with water and methanol

For evaporation drying with DI water and methanol as shown in path (a) of Fig. 4-8, it has been found experimentally that drying with methanol produces a longer detachment length due to the lower surface tension of methanol. However, as described in the previous section, the resulting detachment length is still not long enough for a useful design. Many researchers have also tried using anti-stiction tips along the cantilever beam as those in [13] to reduce the contact area of the cantilever beam and the substrate and hence reduce the adhesion force. Mastrangelo *et al.* [14] has developed a two-step dry-release method for polysilicon MEMS. A series of Parylene posts are formed along the cantilever beams to hold the structure while BHF is used as releasing agent for PSG etching. After the structure is released, the Parylene post is etched away using O_2 plasma etching. Nevertheless, for Parylene microstructures, the result from methanol drying is not promising even if the drying process is speeded up by spin-drying. Therefore, it is believed that in order to achieve successful results, the air/liquid interface has to be completely eliminated.

Sublimation drying with t-butyl alcohol and p-dichlorobenzene

Sublimation is an obvious way to avoid the liquid-air interface as shown in Fig. 4-7(b) [15]. Typically, water is first replaced with methanol because of the solubility of water compared with those of sublimation liquids, while the sublimation liquid is replaced with methanol. After replacing with methanol, the device along with the solution is then refrigerated to solidify the liquids. (Melting point of t-butyl alcohol is 26°C and p-dichlorobenzene is around 56°C.) The samples are then taken out and left at room temperature. Due to the high vapor pressure of the sublimation solid (for t-butyl alcohol, it is 27 torr at 20°C; for p-dichlorobenzene, it is one torr at 25°C), the sublimation is typically done within 15 minutes for t-butyl alcohol and several hours for p-dichlorobenzene. This method requires several special setups and chemicals for the dry releasing, but most importantly, it has been found experimentally that the solidified chemical sublimates off from underneath the beam and oftentimes forms a solid bridge. When this bridge is finally broken, a small amount of trace moisture may condense at the broken tips and thus reattach the bridges. This sequence may ultimately cause stiction for Parylene structures. In addtion, the Parylene film tends to behave more brittle when it is refrigerated and also because of the large temperature coefficient of expansion difference between Parylene and the substrate. Hence, this method is not further pursued here.

Supercritical CO_2 drying

By far, this method is the most established and one which gives the best yield for polysilicon MEMS structures [16]. As shown in the Fig. 4-7(c), instead of the sublimation, the CO_2 pressurized and temperature is increased to its critical point. Fortunately, the critical point for CO_2 is around 1350psi and 40°C, which can be obtained. This method has been used for several years by biologists to prepare their fragile samples.

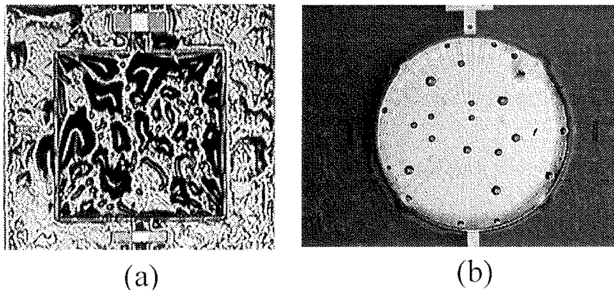

(a) (b)

Fig. 4-9: Photos of Parylene diaphragms after CO_2 supercritical drying
(a) Big diaphragms(2mm*2mm) showing completely ruining of the structure
(b) Small chambers (200μm diameter) showing delamination

However, as shown in Fig. 4-9, this method remarkably does not alleviate any stiction for Parylene microstructures; instead, the structures are ruined during the processes. It is believed that the trace methanol inside the Parylene structure expanded during the process. It is also possible that CO_2 diffused across the Parylene and expanded during the release processes. The large pressure gradient occurring during the processes could have also moved the microstructures and wrinkled the substrate.

Based on the unsuccessful attempts of various Parylene MEMS structures including cantilever beams and chambers using CO_2 supercritical drying processes, this method is not pursued for further investigation.

Teflon-Like Coating for Anti-stiction

Teflon-like film has been explored by many groups to reduce the in-use stiction [17]. For example, plasma-polymerized fluorocarbons resembling PTFE (Teflon) possess many good qualities; they are very hydrophobic (θ_c=109°), smooth, and durable. This method is often applied after the release of the sacrificial layer and is intended to prevent in-use stiction or moisture condensation. Recently, a special Teflon-like polymer, Cytop®, has been developed for MEMS applications [18]. This material is spin-coated and has relatively good adhesion on various MEMS material such as aluminum, copper, silicon dioxide, silicon nitride, and quartz. Besides, it also has a low surface energy (19dyne/cm), high volume resitivity ($>10^{17}\Omega$-cm) and good chemical resistance to most common solvent sand etchants in micromachining. This material was first tested for use as a KOH masking material. KOH solution is famous for attacking the interface between the spun-on material and the substrate and, therefore, very little mask material alternatives can be used. The most common masking materials for KOH are silicon dioxide and silicon nitride. These films require high-temperature deposition steps and therefore can not be easily integrated for post-CMOS processes. However, it has been found experimentally that 1 μm Cytop® film can be spun on bare silicon wafers without a prior adhesion promoter treatment. The film can also withstand the KOH solution up to 80°C for at least 25 hours, which is more than enough for 500 μm silicon etching.

Due to the positive results of this method, the intent is to put the Cytop® layer underneath the Parylene cantilever beams and use Cytop® to convert the pull-down capillary force to become a pull-up force to reduce the stiction as shown in Fig. 4-6(a). However, the experiment showed that the Parylene beams will still stick down to the

substrate, while the detachment length is seemingly less than the case without the Cytop® layer. It is believed that although the Cytop® film provides hydrophobic meniscuses, the Parylene-side is still hydrophobic and therefore pulls down the Parylene cantilevers. It is also suspected that residual charges may be deposited on the Cytop® film, acting as the source of the pulling force similar to the situation that will be discussed in detail in Chapter 5. Therefore, the Cytop® film is no longer under consideration for Parylene anti-stiction structures.

HF vapor phase etching

Although it is believed that HF vapor phase etching can increase the yield drastically, HF is only used for etching for PSG/LTO, which is not chosen as the sacrificial material in our study. Furthermore, the use of HF vapor is believed to be extremely dangerous and therefore will not be used in our study.

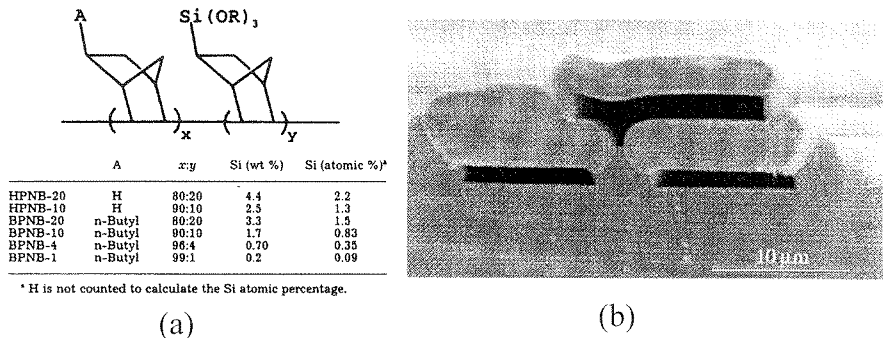

	A	x:y	Si (wt %)	Si (atomic %)[a]
HPNB-20	H	80:20	4.4	2.2
HPNB-10	H	90:10	2.5	1.3
BPNB-20	n-Butyl	80:20	3.3	1.5
BPNB-10	n-Butyl	90:10	1.7	0.83
BPNB-4	n-Butyl	96:4	0.70	0.35
BPNB-1	n-Butyl	99:1	0.2	0.09

[a] H is not counted to calculate the Si atomic percentage.

(a) (b)

Fig. 4-10: Pictures of polynorborene decomposition sacrificial layer technology
(a) Chemical structures of polynorborene
(b) Demonstrated three layer air-channel using polynorborene sacrificial layer

Polynorborene Decomposition Method

The recently developed polynorborene material as shown in Fig. 4-10 can be spun on and patterned using O_2 because of its polymeric essence [19]. To release the MEMS structure, the system is placed at 450°C, under which polynorborene would decompose into carbon dioxide. Because there is no air/liquid interface involved, no surface tension or stiction can take place. Multiple layers of channels and structures have been demonstrated using this material as the sacrificial layer and PECVD silicon nitride or oxide as the structural material. However, due to its decomposition temperature at 450°C, none of the LPCVD materials can be used as the structural material. The readily available material left is therefore spun-on materials such as polyimide and polymers, PECVD material, or metal by evaporation or sputtering. It has been found that sputtering materials such as aluminum or silicon dioxide usually come with huge compressive stresses and therefore, it is hard to control the film quality. Moreover, since Parylene has a low melting point of 250°C, it would be melted at the high decomposition temperature. Therefore, this method is also not suitable for Parylene applications.

Self-Assembly Monolayer (SAM Layer)

Several groups have investigated the use of octadecyltrichlorosilane (OTS) [20] or 1H,1H,2H,2H-perfluorodecyltrichlorosilane (FDTS) for anti-stiction purposes. In principle, the organic groups are usually long-chain alkane-based polymers with active groups at the other end to link with silicon or silicon dioxide. The long alkane chain provides a hydrophobic head group to make the surface hydrophobic and thus reduce the capillary force. This method has been tested with Parylene. However, due to lack of full

understanding of the surface chemistry, the results are varied. Experimentally, it is found the SAM layer does reduce stiction. However, the yield is still quite low without implementing additional methods. Therefore, the SAM layer is only used as an extra method for Parylene microstructure, still leaving the anti-stiction problem to be solved.

After reviewing the previous methods for anti-stiction, a new method still has to be developed that is tailored for Parylene applications. It has also been realized that in order to achieve high-yield stiction free structures, the air/liquid interface has to be completely eliminated because the detachment length is in proportion to $\gamma_{la}^{-1/4}$. Therefore, in the next section, a new technique that combines wet-photoresist dissolution and dry-BrF_3 method is developed to make large freestanding Parylene microstructures.

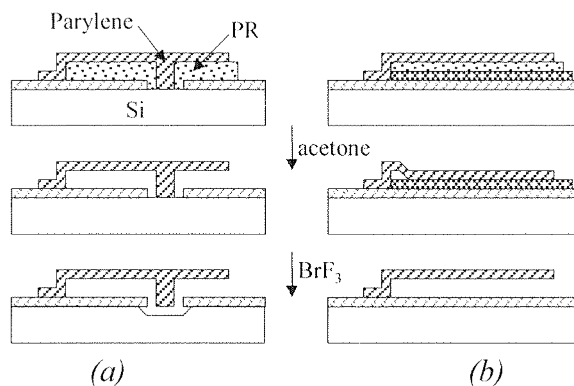

Fig. 4-11: Anti-stiction methods for Parylene freestanding microstructures (a) Post structures (b) sputter silicon structures

4.5 Dry-Release Technology for Parylene Microstructures

Here, based on BrF_3 dry release, two anti-stiction approaches to making large freestanding Parylene structures are demonstrated. Fig. 4-11 shows the two approaches that were developed to avoid stiction in Parylene structures. In both cases, Parylene is used as the structural layer and photoresist as the sacrificial layer.

The first approach (Fig. 4-11 (a)) is similar to Mastrangelo's approach in [14]. Basically, an array of posts is fabricated in the Parylene structural layer. During the process of photoresist dissolution in acetone, these posts support the Parylene structures and prevent them from sticking to the substrate. Then the structures are freed by etching away the silicon area underneath the posts with BrF_3 vapor. Since BrF_3 has a fairly high etching selectivity of silicon over Parylene and other materials [8], the integrity of the Parylene structure is not attacked. In the second approach (Fig. 4-11(b)), a composite sacrificial layer of photoresist and sputtered amorphous silicon is used. The structure is first released by dissolving the sacrificial photoresist in acetone. Stiction could occur in large structures after this step, but a subsequent etch of the sacrificial amorphous silicon in BrF_3 vapor totally frees the structures.

In next section, a simple review of bromine trifluoride (BrF_3) dry vapor etch of silicon will first be given. Second, the design and fabrication of Parylene microstructures using both technologies shown in Fig. 4-11 will be used to demonstrate large area Parylene microstructures.

4.5.1 Review of BrF_3 vapor etching of silicon

Bromine trifluoride (BrF_3) vapor etching system has been recently developed in our group by Wang *et al.* [8]. The BrF_3 is a fluorine-containing interhalogen that etches silicon spontaneously and isotropically at room temperature. Hence, plasma etching is not required for BrF_3 to etch silicon. Moreover, because of its isotropic etching characteristics, the silicon underneath the Parylene or other mask materials can be etched with relatively high selectivity. The physical properties of BrF_3 are listed in Table 4-1.

From the figure, it is clear that BrF_3 is a liquid with high vapor pressure at room temperature.

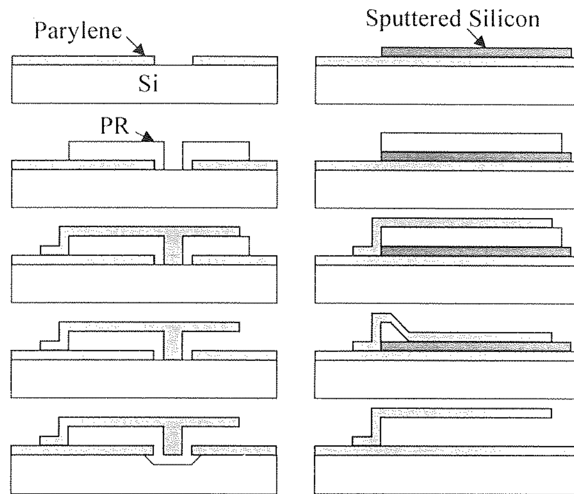

Fig. 4-12: Process flow for Anti-stiction approaches
(a) post structure (b) sputtered silicon

Table 4-1: Physical properties of BrF_3

Molar Mass	Liquid Density	Melting Point	Boiling Point	Vapor Pressure
137	2.8 kg/L	8.8°C	125°C	7torr

Although some similar etchants such as XeF_2 have been proposed, the advantage of using BrF_3 is that is has a high etching rate and is commercially available. The etching mechanism of BrF_3 is believed to be similar to fluorine containing interhalogens with the volatile etching products of Br_2 and SiF_4 as shown in the following equations.

$$BrF_3 + Si \rightarrow Br_2 + SiF_4 \tag{4.9}$$

4.5.2 Design and Fabrication of Freestanding Parylene Microstructures

Using both methods outlined in Fig. 4-11, various surface micromachined Parylene structures have been designed, fabricated, and tested. Fig. 4-12 shows the fabrication process. The process starts with 4-inch silicon wafers. First, the silicon wafer surface is roughened in BrF_3 vapor [21] to enhance the adhesion of Parylene layer deposited later. The wafers are then primed with A-174 adhesion promoter followed by the deposition of a layer of 1 μm thick Parylene C. In the first approach, the Parylene C layer is patterned to expose the substrate silicon area on which the posts in the structural layer can anchor to. In the second approach, a layer of 1000 Å thick amorphous silicon is sputtered on the Parylene C layer. The sputtering is performed in a MRC Model 8667 sputtering machine at 200 W RF power for one hour. With the cooling and constant rotation of the wafer platform during sputtering, the temperature of the process is kept low; no thermal damage to the Parylene layer can be found visually. However, the thin amorphous silicon layer tends to crack and delaminate from the bottom Parylene layer due to its high compressive stress. Experimentally, we found that a pre-annealing of the Parylene C layer at 150°C in nitrogen ambient for 30 minutes before the amorphous silicon sputtering can eliminate the cracking problem. Next, a layer of 4.5 μm sacrificial photoresist is spin-coated and patterned, followed by deposition and patterning of a 4.5 μm thick Parylene structural layer. Finally, the structures are freed by dissolving the photoresist in acetone and etching away the silicon/amorphous silicon layer in BrF_3 vapor.

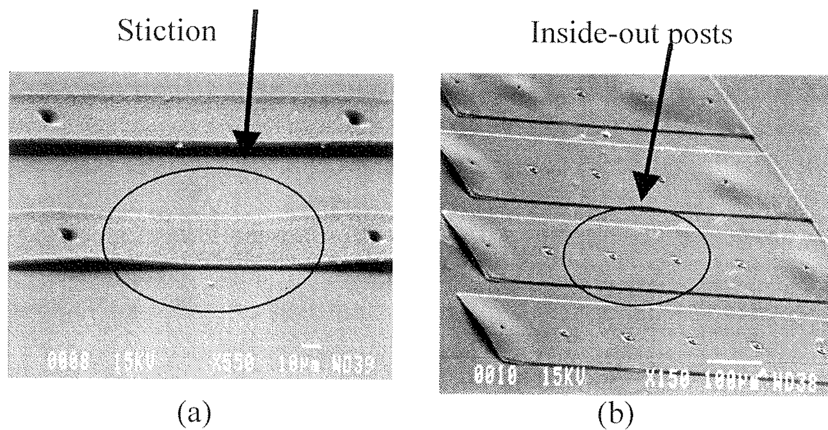

Fig. 4-13: Stiction of Parylene microstructures due to large post spacing
(a) The stiction happens in the middle of the posts
(b) The surface tension pull the posts inside-out

4.6 Results and Discussion of Anti-stiction methods

In the first anti-stiction approach with post structures, the distance between two neighboring posts is an important parameter. To minimize the effect of the posts on the integrity of the Parylene structures, the minimum number of posts should be used. However, if too few posts are used and the distance between two posts is too large, stiction could happen in the area between the posts as shown in Fig. 4-13 (a) during the photoresist releasing process. Moreover, as shown in Fig. 4-13 (b) the surface tension force is large enough to turn the fabricated posts inside-out.

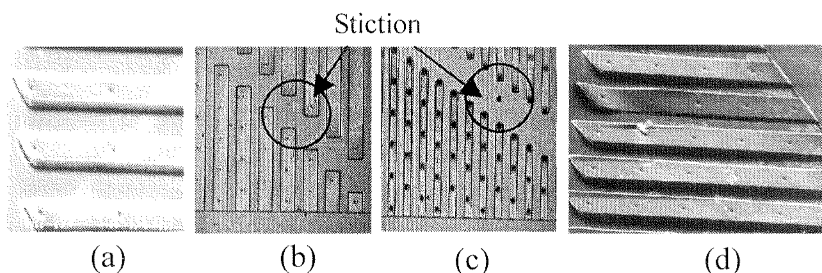

Fig. 4-14: Structures fabricated with the first approach

Our experimental results are consistent with this model. Fig. 4-14 shows the freestanding cantilever beams with post structures. The maximum distance between two posts without stiction of the Parylene structural is 150μm. It can be also seen from Fig. 4-14 (b,c,d) that cantilever beams with widths larger than 150μm show stiction at the edge of the beams. This indicates that the maximum distance between the post and the edge of the beam is 75μm.

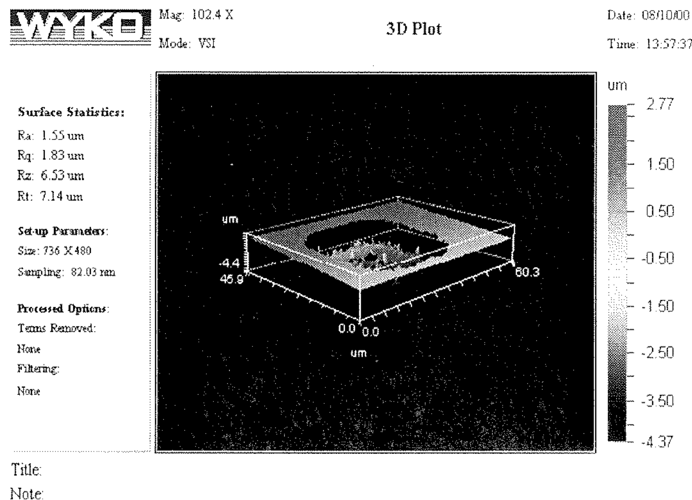

Fig. 4-15: WYKO profile of the hole underneath the post etched by BrF_3

Fig. 4-15 is a WYKO surface profile of a hole underneath a post etched by BrF_3 vapor for one minute at four torr. The hole is measured to be 35 μm in diameter and 4.4 μm deep. This confirms the isotropic etching of silicon by BrF_3.

Surface micromachined structures fabricated using the second approach are shown in Fig. 4-16. From Fig. 4-16(a), it can be seen that at the end of almost every Parylene cantilever beam, there is a gray area followed by a series of optical interference fringes. This suggests that the cantilever beams stick to the sputtered silicon layer after photoresist removal. Fig. 4-16(b) shows the same structures after the BrF_3 etching of the sputtered silicon layer. The elimination of stiction is clear. It is suspected that the fringes are the result of the etch front of BrF_3 vapor. The fringes also indicate that the beams do

not come back to their original positions. However, by touching the beams with a probe under an optical microscope, we confirmed that the beams are indeed freestanding.

To eliminate the etching of substrate silicon underneath post structures, this sputtered silicon approach can be combined with the post structures by making thin sacrificial sputtered silicon layers only at the bottom of the posts. With these technologies, almost any Parylene surface micromachined structures with horizontal and vertical movements can be developed.

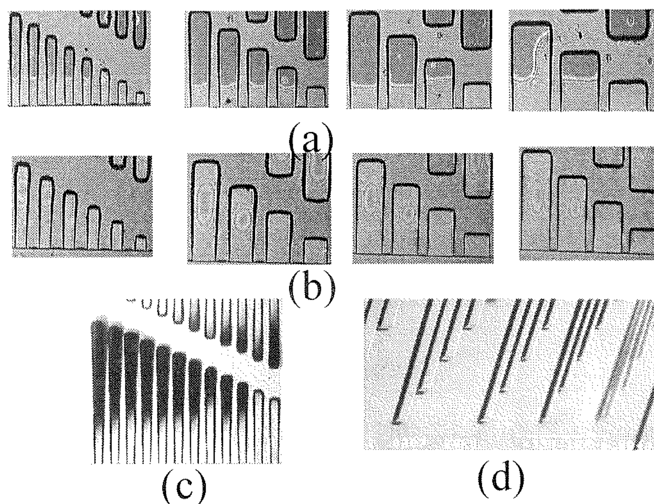

Fig. 4-16: Structure released by sputter silicon method
(a) Most of beams stuck down when drying after Acetone releasing
(b) All the beams become freestanding after BrF3 releasing
(c) Freestanding Parylene beams curving up due to stress of Au
(d) SEM of freestanding Parylene beams

Aside from the deflection limitation due to gravity, there is no obvious upper limit on the dimensions of the structures that can be made with these technologies. These technologies can also be applied to other structural materials such as polymers and metals as long as the structural material is not etched significantly by BrF_3 vapor.

Finally, in order to demonstrate that the above methods are capable of making large area surface micromachined freestanding Parylene microstructures, Fig. 4-17 shows miscellaneous surface micromachined structures such as flaps, Guckel rings, and membranes that have been fabricated using both technologies.

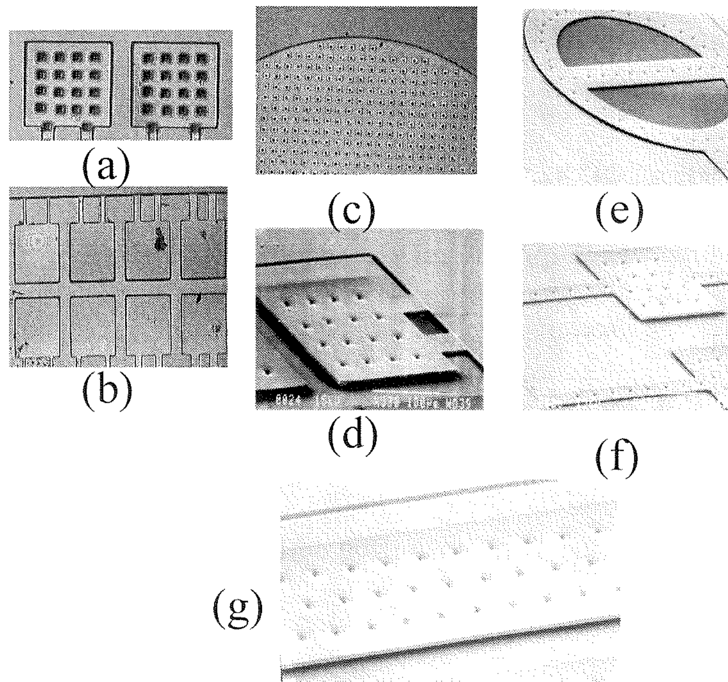

Fig. 4-17: Miscellaneous freestanding Parylene microstructures

(a) Flaps (200μm*200μm) demonstrated by post method
(b) Flap (200μm*200μm) by sputter silicon method
(c) 2mm diameter diaphragm by post methods
(d) SEM of flaps (200μm*200μm) by post method
(e) SEM of Guckel ring by post method
(f) SEM of torsional plate by post method
(g) SEM of 2mm long cantilever beam by post method

4.7 Conclusion

In this chapter, novel technologies to fabricate large freestanding Parylene microstructures have been demonstrated to overcome the pulling force from surface tension. A release process of wet photoresist dissolution followed by dry BrF_3 etching completely eliminates the air/liquid interface and thereby eliminates stiction. Freestanding 1 mm long cantilever beams and 2 mm diameter diaphragms have been demonstrated. This technique is suitable for integrated MEMS devices and systems such as accelerometer, gyroscopes, microphones with on-chip electronics, etc. Although the demonstrated technology is geared toward Parylene application, it should be readily applicable for many polymer MEMS applications as long as the selectivity between polymer and BrF_3 etchant is adequate. Moreover, many other combinations of dry sacrificial materials and etchants can be potentially used, and therefore, the technologies presented here are not restricted to only sputtered amphorous silicon and BrF_3 vapor etchant studied here.

4.8 References

[1] P. F. Man, D. K. Jones, and C. H. Mastrangelo, "Microfluidic Plastic Capillary on Silicon Substrates: A New Inexpensive Technology for Bioanalysis Chips," Proceedings of International Workshop on Micro Electro Mechanical Systems (MEMS '97), Nagoya, Japan, 1997.

[2] X. Yang, C. Grosjean, and Y.C. Tai, "A Low Power MEMS Silicone/Parylene Valve," Technical Digest, Solid State Sensor and Actuator Workshop, Hilton Head Island, SC, USA, 1998.

[3] C. H. Han and E. S. Kim, "Parylene Diaphragm Piezoelectric Acoustic Transducers," IEEE International MicroElectroMechanical Systems Conference (MEMS'00), Miyazaki, Japan, 2000.

[4] J. Q. Liu, Y. C. Tai, J. Lee, K. C. Pong, Y. Zohar, and C. M. Ho, "In Situ Monitoring and Universal Modeling of Sacrificial PSG Etching Using Hydrofluroic Acid," Proceedings of IEEE Workshop on MicroElectroMechanical Systems (MEMS '93), Fort Lauderdale, USA, Feburary 1993.

[5] S. Wu, Q. Lin, Y. Yuen, and Y.C. Tai, "MEMS Flow Sensor for Nano-Fluidic Applications," Thirteenth IEEE International Conference on Micro Electro Mechanical Systems (MEMS '00), Miyazaki, Japan, 2000.

[6] T. R. Tsao, T. Y. Hsu, and Y. C. Tai, "Copper Sacrificial Layer Technology for use in surface micromachining," Micromachining Workshop III, Southern California Chapter of American Vacuum Society, Anaheim, CA, September, 1996.

[7] M. A. Schmidt, R. T. Howe, S. D. Senturia, and J. H. Haritonidis, "Design and Calibration of a Microfabricated Floating-Element Shear Stress Sensor," *IEEE Transactions on Electronics Devices*, vol.ED-35, pp.750-757, 1988.

[8] X. Q. Wang, X. Yang, K. Walsh, and Y. C. Tai, "Gas-Phase Silicon Ecthing with Bromine Trifluoride," Technical Digest, International Conference on Solid-State Sensors and Actuators, Chicago, IL, USA, 1997.

[9] L. J. Hornbeck, "Spatial Light Modulator and Method," Proceedings of the SPIE Workshop on Micromachining and Microfabrication Processes, U.S., 1995.

[10] J. R. Webster, "Monolithic Structures for Integrated Capillary Electrophoresis Systems," Ph.D. thesis, University of Michigan, 1999.

[11] C. H. Mastrangelo and C. H. Hsu, "Mechanical Stability and Adhesion of Microstructures Under Capillary Forces: Part I: Basic Theory," *IEEE Journal of Microelectromechanical Systems*, vol. 2, pp. 33-43, 1993.

[12] N. Tas, T. Sonnenberg, H. Jansen, R. Legtenberg, and M. Elwenspoek, "Stiction in Surface Micromachining," *Journal of Micromechanics and Microengineering*, vol. 6, pp. 385-397, 1996.

[13] L. S. Fan, "Integrated Micromachinery--Moving Structures in Stiction Chips," *Ph.D. Thesis, University of California, Berkeley*, 1990.

[14] C. H. Mastrangelo and G. S. Saloka, "A Dry-Release Method Based on Polymer Columns for Microstructure Fabrication," Proceedings of IEEE Workshop on Micro Electro Mechanical Systems, Fort Lauderdale, FL, USA, 1993.

[15] N. Takeshima, K. J. Gabriel, M. Ozaki, J. Takashashi, H. Horiguchi, and H. Fujita, "Electrostatic parallelogram actuators," *Transducers '91*, pp. 63-66, 1991.

[16] G. T. Mulherm, D. Soane, and R. T. Howe, "Supercritical carbon dioxide drying for microstructures," *Transducers '93*, pp. 296-299, 1993.

[17] P. F. Man, B. P. Gogoi, and C. H. Mastrangelo, "Elimination of post-release adhesion in microstructures using thin conformal fluorocarbon films," Proceedings of IEEE MicroElectroMechanical System Workshop, San Diego, CA, USA, 1996.

[18] http://www.bellexinternational.com/main.asp

[19] P. A. Kohl, Q. Zhao, K. Patel, and D. Schmidt, "Air-Gaps for Electrical Interconnections," *Electrochemical and Solid State Letters*, vol. 1, pp. 49-51, 1998.

[20] M. Houston, R. Maboudian, and R. T. Howe, "Self-assembled monolayer films as durable anti-stiction coatings for polysilicon microstructures," *International Workshops on Solid-State Sensors and Actuators (Hilton Head '96)*, pp. 42-47, 1996.

[21] X.-Q. Wang, "Integrated Parylene Micro Electro Mechanical Systems (MEMS)," Ph.D. thesis, CA, California Institute of Technology, 2000.

CHAPTER 5

Parasitic Charging Effect on Parylene Electrostatic Actuators and a Surface Micromachined In-Channel Flow Restrictor

Abstract

In this chapter, characteristics and problems of Parylene electrostatic actuators will first be studied, especially regarding the issue of dielectrics charging and its influence on electrostatic actuators. After some understanding into the issues of dielectrics charging, a surface micromachined in-channel flow restrictor will be characterized. A flow restrictor, though ac-actuated, can change the flow rate up to 50% in nl/min range with several psi pressure.

5.1 Preface

Electrostatic actuation has provided an elegant way to move microstructures that are within several micrometers apart. The fundamental principle behind this electrostatic actuation is the attraction force between opposite charges as discussed earlier in Chapter 1. Although the electrostatic force is a strong function of distance, the force generated by this principle at micrometer distances has powered various interesting microdevices. A famous example of this is the ADXL-150 micromachined accelerometer [1], which uses interdigitated fingers to sense the capacitance change due to the acceleration as shown in

Chapter 1. This device, to the author's knowledge, will be well-employed in air bag systems by the end of 2001. Another famous example that uses this electrostatic actuator is the DMD (Digital Mirror Display) [2] developed by Texas Instruments in the late 1980s as shown in Fig. 5-1. The mirror itself is a torsional electrostatic actuator which assumes only two stable positions: ON (when voltage is applied) and OFF (when voltage is removed). DMD devices have been used in projection TV systems and more recently have been used to fabricate mask-less DNA chips and protein chips for genomics applications [3].

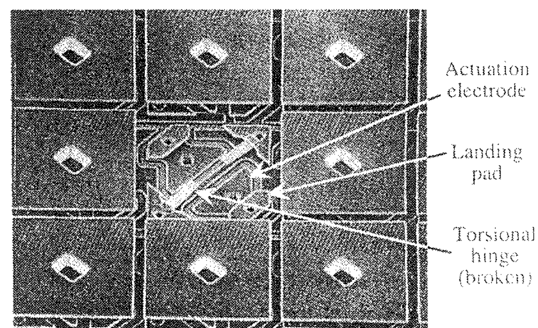

Fig. 5-1: A SEM photo showing the Digital Mirror Display and its underlying elements

Many other devices that employ electrostatic actuation principles have been developed over the last 10 years. They can all be roughly divided into two categories. One of them is a sensor, which uses electrostatic force to sense physical parameters such as accelerometers, gyroscopes, etc.; the other is an actuator, which uses electrostatic force to move microstructures such as comb-drives, RF capacitive switches, and micro-optical switches. Thus it is important to understand the limitations of electrostatic actuators before designing suitable physical parameters that can lead to better device performance and functionality.

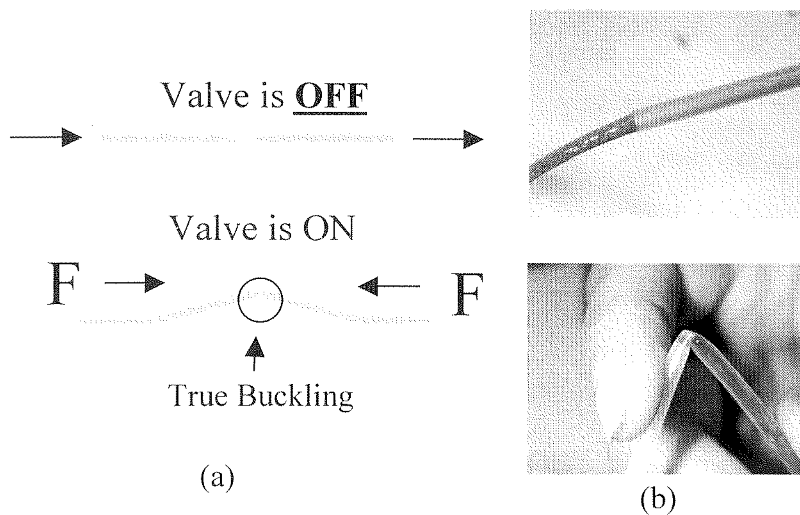

Fig. 5-2: Schematics of original buckling valve ideas
(a) The schematics showing possible bulking at center of the flow channel
(b) The macroscopic bulking of the straw

Using polymers such as Parylene to make microstructures has its inherent advantages, such as low Young's modulus, good electric insulation, low-deposition temperature (room temperature), fast prototype time and, most importantly, CMOS compatibility and integration. The original goal of this chapter is to demonstrate an in-channel buckling microvalve (see Fig. 5-2) to stop flow rate at several nL per minute under a few psi inlet pressure. The microvalve is intended to be used as one of the components for "lab-on-a-chip" applications such as DNA sequence, or a drug delivery system [4] with the potential of being integrated on CMOS circuitry. The advantage of an in-channel microvalve compared to traditional valves such as the one demonstrated in Chapter 3 is that the dead-volume is minimal and the flow path can remain fairly planar. Besides, for electrostatic actuation, the electric field would not drop across the fluid. The ionic or charged molecules in fluids would be attracted to the electrode if the electric field is large enough. To the author's knowledge, no in-channel micro-valve has been demonstrated thus far.

Due to its excellent dielectric performance, several interesting charging phenomena have first been observed on Parylene electrostatic actuators. These interesting phenomena provide important design information for electrostatic actuators with dielectrics in between air gaps. Most importantly, these findings can also be applied to other dielectric-based electrostatic actuators and not only limited to Parylene.

Due to the charging effect that will be discussed later, the originally designed microvalve can not be permanently held on the "ON" (flow-stopped) condition. AC-actuation has to be used to demonstrate the idea. The microvalve therefore behaves as a flow restrictor that can be used to slow down the flow rate while the application demands.

This chapter will be divided into six sections. First, the problems of Parylene-based electrostatic actuators will be illustrated in section 5.2. In section 5.3, a theoretical investigation of the interfacial charging effect on Parylene electrostatic actuators will be studied, and the breakdown of air at micrometer separations will be surveyed. Section 5.4 will then use the knowledge of previous sections to correlate the experimental results. Section 5.5 will then focus on the design and characterization of the flow restrictor aforementioned. Finally, section 5.6 will then conclude the findings gathered from previous sections and correlate those findings to other dielectric based electrostatic actuators. Design principle of these devices to avoid charging will be summarized.

5.2 Parylene Electrostatic Actuator and its Interesting Problem

In the last chapter, a technology was demonstrated to make freestanding Parylene microstructures using photoresist as the sacrificial layer. This technology, combining wet acetone dissolution of photoresist and BrF_3, provides a way to overcome the inherent stiction problem in polymer microstructures with low Young's modulus. It is therefore suitable to integrate electrostatic actuators with this technology. The process flow shown in Fig. 5-3 that is used to make electrostatic actuators is similar to those described in the last chapter except for the thermal evaporation of the top and bottom Cr/Au electrodes.

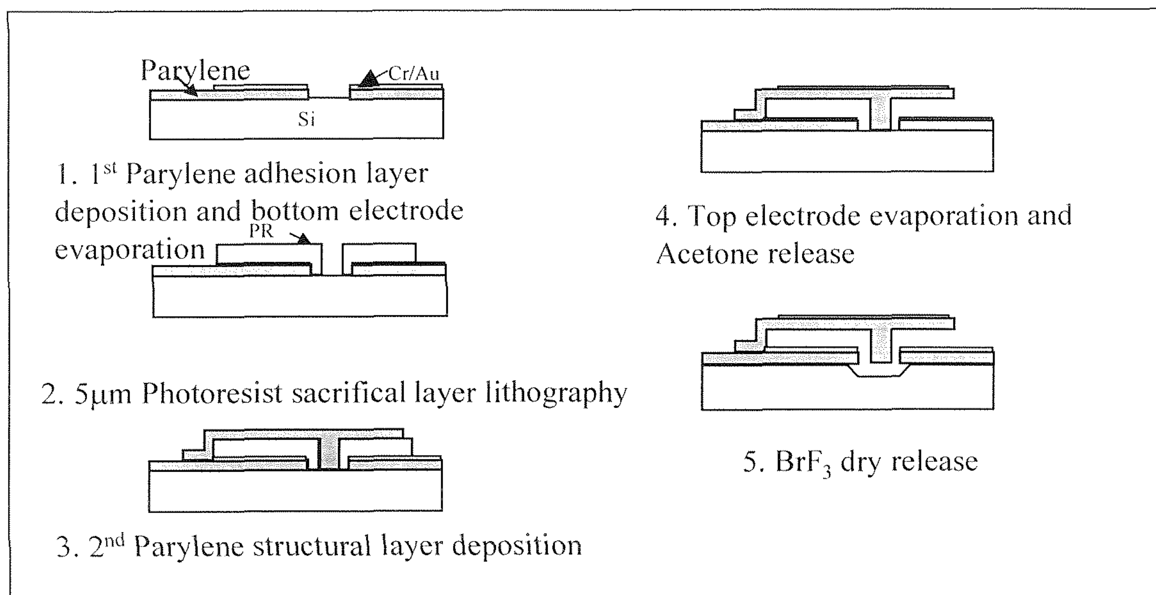

Fig. 5-3: Simplified process flow for Parylene electrostatic actuators

The finished devices as shown in Fig. 5-4 were operated by applying a high voltage supply; the up-and-down movement was recorded under a microscope. The up or down position can be distinguished clearly because residual stress in the Au and Parylene composite structural layer causes the beam to warp a little bit, which helps to distinguish the on or off positions of the beam.

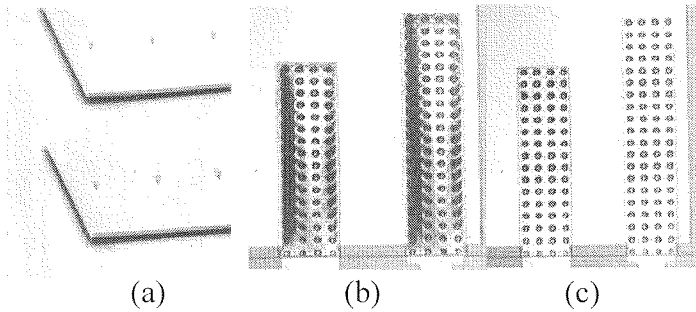

Fig. 5-4: Photos of fabricated Parylene electrostatic actuators

(a) SEM photo (b) Actuators at freestanding position (OFF)

(c) Actuators at touched-down position (ON)

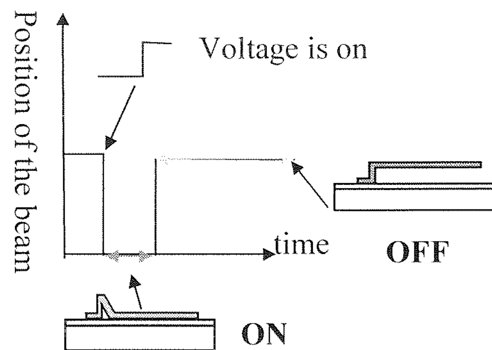

Fig. 5-5: Schematics of "bounce-back" effect

5.2.1 Bounce-Back Problem

Electrostatic actuation has been observed under either D.C. or A.C. conditions at high voltage (~160V). However, a new "bounce-back" phenomenon that has never been previously described was observed. Under high voltage, the beam initially comes down and makes a firm contact with the substrate. However, instead of continuing to make that contact at the ON position, the beam bounces back within seconds and remains at the OFF position while the high voltage is still on. This phenomenon is described pictorially in Fig. 5-5.

5.2.2 High Pull-in voltage

An even more surprising observation was made; the threshold voltage required to pull the cantilever beam down is tremendously high and even higher than that for polysilicon microstructures with the same geometrical dimensions (see Fig. 5-6). The pull-in voltage measurement is therefore conducted on an array of cantilever beams with the same width (200μm) but various lengths from 100μm to 1 mm. The devices all have the same Parylene thickness (2.5μm) and air gap height (5μm). The theoretical threshold voltage is calculated by the formula from Petersen [5]:

$$V_{th} = \sqrt{\frac{18(EI)_{eff}\, d_g^{\,3}}{5\varepsilon_0 L^4 w}} \tag{5.1}$$

where $(EI)_{eff}$ is given as

$$(EI)_{eff} \approx \left(\frac{wt_1^3}{12}\right)\left(\frac{4+6\frac{t_2}{t_1}+\frac{E_1t_1}{E_2t_2}}{1+\frac{E_1t_1}{E_2t_2}}\right) \tag{5.2}$$

where t_1, t_2, E_1, E_2, are the thicknesses and Young's modulus, respectively, of the lower (1) and upper (2) layers of the beam. This also illustrates the point that most micromachined structures need to be treated as composite materials. The result shows a significant deviation from the theoretical calculation, implying a different mechanism is at play for this device.

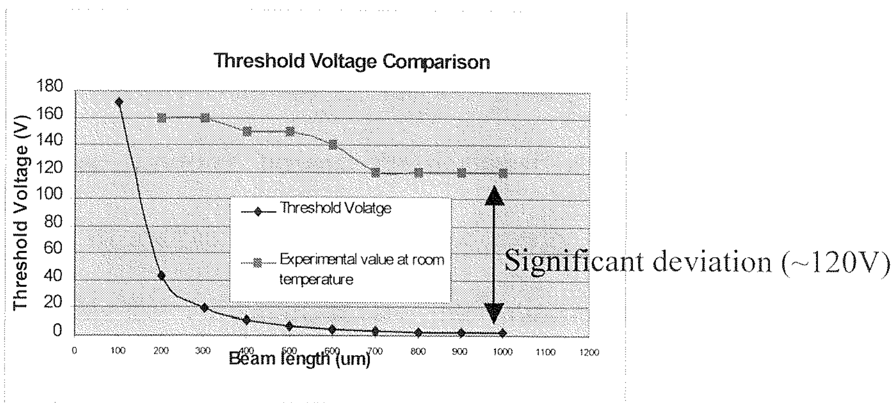

Fig. 5-6: Experimental and theroretical pull-in voltage for Parylene electrostatic actuators

5.2.3 Parylene Microstructures under SEM irradiation

The earlier work on Analog Devices ADXL50 accelerometer under proton and radiation irradiation showed that the ionization effects in both the sensor and the electronics contributed to the radiation response of the devices [6]. However, Knudsen *et al.* [7] have demonstrated that irradiation via an aperture on the sensor caused a shift in the output voltage. This phenomenon is caused by the charging of the dielectric below the sensor. Charging dielectrics is a contest between the emission of low-energy secondary electrons and the absorption of higher-energy electrons backscattered from other locations (e.g., a substrate below passivation layers). The latter mechanism to the former is greatest when the primary electrons are high-energy and hit the device at normal incidence. It is empirically known that the dielectrics typically charge negatively when the primary electrons hit the device at normal incidence for energies greater than 10KeV.

In this section, the behavior of Parylene microstructures under SEM is investigated. The sample is fabricated according to the steps described in Chapter 4. In addition, a thin 200Å Au layer is also thermally evaporated on top of the chip. This is a

common practice to prepare the sample prior to SEM imaging. This thin gold layer typically serves as electrodes so all the surface will form a common ground to prevent charging of dielectrics. However, because the thickness of this gold is not enough to prevent the charging of Parylene film, and higher energy electrons will have enough energy to penetrate this thin gold film, several interesting phenomena were discovered and will be explained qualitatively here. This study alludes to clues that suggest the interesting phenomena aforementioned may be caused by charging.

Although charging of dielectrics under SEM has been investigated extensively by previous researchers, none of them have investigated freestanding dielectrics inside the SEM. It is well known that the total electron yield is $\sigma = \eta + \delta$ [8]. As the sum of the backscattering coefficient η and the secondary electron yield δ becomes larger than unity between two critical energies E_1 and E_2, the specimen becomes negatively charged (surface potential $U_s<0$). When $\sigma<1$ for $E>E_2$ along with the case of infinite leakage resistance to ground, the surface potential becomes $U_s=-(E-E_2)/e$ (E_2 is the landing energy of electrons that makes $\sigma=1$). It is also known from the study of dielectrics irradiated with γ quanta that the space charge region is formed within the dielectrics samples, thus creating a built-in electric field [9].

From the above, it is clear that under SEM environment, the Parylene layers will have a space charge region inside with an effective negative surface potential. The phenomenon is also observed using the test sample described in the previous sections. Fig. 5-7 shows both SEM and schematics of the Parylene microstructures under SEM environment. When the sample is viewed with a tilted angle and electron is irradiated

between the air gaps, the microstructure would gradually curve up and finally turn with angles greater than 90° after continuous irradiation for more than two minutes.

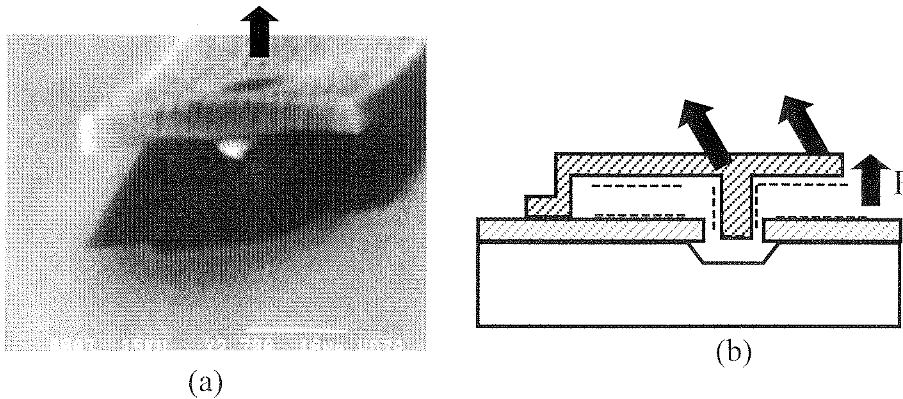

Fig. 5-7: Movement of freestanding cantilever beams under SEM
(a) SEM photo of cantilever beams curving up
(b) Schematic of charge accumulation and the Columb force under SEM

It is now clear that the phenomenon is caused by continuous charging of the Parylene samples both on the bottom of the Parylene cantilever and at top of the substrate. At the top of the substrate, there is no metal coverage, and thus no conduction path to leak out the excessive negative charge deposits on the surfaces. Furthermore, the negative charges both on the bottom of the cantilever beam and top of the substrate provide a repulsive Columbic force and thus push the cantilever upwards. While the irradiation time increases, the samples are deposited with more negative charges and thus provide larger force to finally push the cantilever beam to curl upwardly by more than 90 degrees.

In this section, the behavior of Parylene microstructure inside SEM is analyzed. In order to prevent the undesirable charging effect, samples have to be covered with enough gold to provide both conduction path and irradiation barrier for the dielectrics. Experimentally, 500Å thermally-evaporated gold seems to be able to achieve this goal. The experiment conducted here, although restricted to Parylene dielectrics, should be

capable of being applied to all dielectrics in general. Parylene, however, has a much higher resistivity and requires special attention.

5.3 Theoretical calculation of the charging effect and air breakdown mechanisms

In this section, two important questions will be answered. First, is it really possible to break down the air using the voltage range that is applied in the air gap? Second, if air indeed breaks down and generates residual charges on Parylene/air interface, how would this affect the performance of electrostatic actuators?

5.3.1 Breakdown mechanism of air medium

For a long time, air has been treated as a perfect insulator in the micromachining research society. Therefore, most devices, especially electrostatic actuated/sensing devices such as accelerometers, gyroscopes, comb drives, scratch drive actuators, and micromirrors are built without consideration of the air medium. However, it is well known that air is not a perfect insulator and breakdowns during many occasions in our daily lives. Some of the breakdowns are natural and bring us disasters such as lightning, and thus electric shocks. Others have been utilized by human beings to aid us in several diverse areas such as electrostatic imaging, vacuum tubes and electret microphone.

Although it is well accepted that devices operating under atmospheric environments should be operated well below the safety limit of 3 MV/m [10], many micromachined devices do not follow to this rule. 3MV/m may sound astonishingly large, but in the micromachining domain, especially in the electrostatic field, it is actually only

equivalent to 3V/μm. Nevertheless, to the author's knowledge, no one has reported problems associated with using high electrical fields across short air gaps. It is possible that most researchers use polysilicon, which is semiconducting, as the actuation material. Thus, even if the air breaks down during operation, electrodes can still exchange the ions and electrons freely at the interface. However, as more and more researchers are using advanced materials such as polymers for structural materials, this problem becomes more important and have to be put into consideration at the initial stages of the design.

Derivation of the Paschen curve

The voltage derived by Paschen's law [11] is the most well accepted number for considering breakdown. Let us consider breakdown of air with two plane electrodes, separated by a distance d, with a DC voltage V_a connected across them. Townsend gave the first developed quantitative model [11] to explain the ionization process, which is valid over a wide range of density and electric field. Let's assume $V_a >> V_j$ (V_j is the ionization voltage) and the gas density is such that the mean free path for collision ionization is much smaller than the distance between the electrodes, then $\lambda e_j << d$, where λe_j corresponds to the σ_j maximum. N_0 electrons are emitted per unit time and unit area from the cathode with negligible initial velocity by, for example, photoemission. Thus, electrons will gain sufficient energy from the electric field to ionize gas particles after a distance $x >= V_j/E$. When an electron gains enough energy to ionize a neutral gas molecule, an ion-electron pair is formed. The ion moves toward the cathode, and both the projectile and liberated electrons move towards the anode. The liberated and projectile

electron can again ionize the neutral molecules and cause avalanche breakdown, conducting a huge current.

Let us assume in a layer of thickness *dx*, through which *N(x)* electrons flow per unit time:

$$dN = N(x)\alpha dx \tag{5.3}$$

where α is the number of electron/ion pairs that each electron creates per unit length on its way to the anode; α is thus named Townsend's first coefficient. The current multiplication factor η is defined as the ratio of currents with and without breakdown.

Although ions can ionize the gas particles on their way to the cathode, the probability is much smaller than that for electrons. According to a Townsend theory,

$$\eta = \frac{N_a}{N_0} = \frac{i_a}{i_0} = e^{\alpha d} \tag{5.4}$$

$$\alpha = nAe^{-B/(E/n)} \tag{5.5}$$

The secondary emission from the cathode starts a new electron avalanche, which generates new electron-ion pairs and new secondary electrons. The first electrons in the first avalanche generate $e^{\alpha d}$ electrons, which reach the anode, while $e^{\alpha d}$-1 ions reach the cathode. If every ion releases γ_j electrons, there are

$$\gamma_j(e^{\alpha d} - 1) = K \tag{5.6}$$

second-generation electrons. Eventually $Ke^{\alpha d}$ electrons reach the anode. Correspondingly, ions at the cathode produce $\gamma_j K\ (e^{\alpha d}-1)=K^2$, the third generation secondary electrons. For every electron leaving the cathode,

$$n_a = e^{\alpha d}(1 + K + K^2 + \ldots) = e^{\alpha d}\frac{1-K^n}{1-K} \tag{5.7}$$

electrons reach the anode. If K is greater than 1, the current in the discharge increases are limited only by the power supply. If K is less than 1,

$$\lim_{n\to\infty}\frac{1-K^n}{1-K}=\frac{1}{1-K} \quad (5.8).$$

The current multiplication factor can then be written as:

$$\eta=\frac{e^{\alpha d}}{1-\gamma_j(e^{\alpha d}-1)} \quad (5.9)$$

Different phenomena can affect a discharge: photons created in the gas, X-ray at the anode, and thermionic emissions from the cathode. We can include all the secondary electron generation processes and lump them as:

$$\eta_0=\frac{e^{\alpha d}}{1-\gamma(e^{\alpha d}-1)} \quad (5.10)$$

where γ is the secondary ionization or Townsend's second coefficient, which accounts for all secondary processes. This parameter γ depends strongly on the cathode material and on the gas, but it is independent of the electric field strength in the discharge regions. As the denominator of the above equation goes to zero, the theory becomes invalid and breakdown happens.

$$e^{\alpha d}\geq 1+\frac{1}{\gamma} \quad (5.11)$$

where α depends on the electric field strength. At the moment of breakdown $E=V_b/d$ (where V_b is the breakdown voltage). So, approximately,

$$\alpha d=\frac{\alpha/p}{E/p}V_b=A'pde^{-B'pd/V_b}=\ln(1+\frac{1}{\gamma})=M_d=const \quad (5.12)$$

where $A'=An/p$ and $B'=Bn/p$, and thus the breakdown voltage is

$$V_b = \frac{B' pd}{\ln(A' pd) - \ln M_d} = f(pd) \tag{5.13}$$

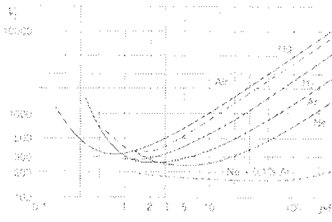

Fig. 5-8: Paschen's curve (pd in mm.Hg.mm, V_b in volt) (from [11])

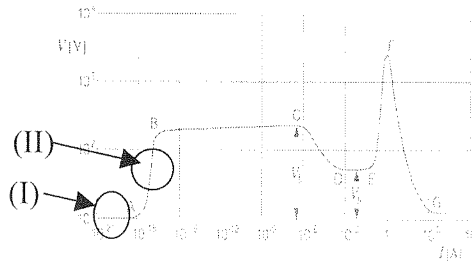

Fig. 5-9: voltage vs. current in a discharge tube (from [11])

The above equation suggests that breakdown voltage only depends on the product of the interelectrode spacing and pressure. The above equation is also known as Paschen's law and is drawn graphically as Fig. 5-8. The breakdown voltage becomes very large when *pd* approaches infinity where the mean free path is small so the molecules can not reach the ionization energy. The breakdown voltage also become very large when *pd* approaches zero where very few molecules can be ionized.

Breakdown at micrometer range

The dielectric strength of an air gap is represented by Paschen's law which is plotted as the breakdown voltage V_{br} vs. the product *pd* of air pressure and spacing (see Fig. 5-8). The absolute minimum of this curve amounts to V_{br}=340V at pd=6-8*10^{-3} bar mm for air at room temperature. However, Germer [12] and Dhariwal *et al.* [13] have found that the Paschen's law is only applicable for electrode spacing above 4 μm. In the range below 4 μm, the breakdown voltage deviates strongly towards lower values. Dhariwal et al. have found the lowest breakdown voltages of 20V at a spacing of 1 μm.

However, in order for charges to accumulate, air breakdown may not be necessary. The breakdown voltage in Paschen's curve is the effect of avalanche breakdown; however, only the initial ionization current is needed to cause charge deposition. As shown in Fig. 5-9 (point II), Townsend's discharge current grows tremendously before the breakdown voltage is reached. The charges in those currents will travel and finally deposit on the Parylene/ air interface.

In the next subsection, the effect of the charge deposited on Parylene electrostatic actuators will be examined. This fundamental background will be also used again in the next chapter to calculate the sensitivity of the electret microphones.

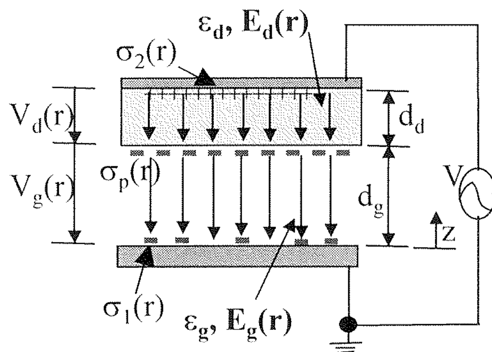

Fig. 5-10: Schematic of residual charge on Parylene/air interface

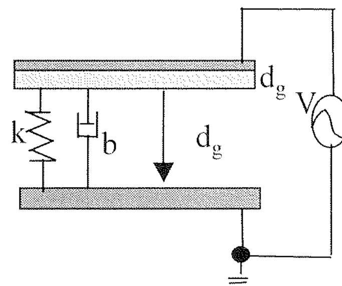

Fig. 5-11: Schematics of mechanical representation of electrostatic actuator

5.3.2 Theoretical examination of the charging effect on electro-static actuators

In this section, the effect of residual charge on Parylene electrostatic actuators will be examined. First, the pull-in voltage shift due to the residual charges will be calculated. Second, the residual charge density in our system will be calculated to approximate the voltage shift in Parylene electrostatic actuators.

Theoretical examination of force-shift caused by parasitic charge accumulation

The following presents a rough theoretical estimation of parasitic charging effects on the behavior of electrostatic actuators, especially the effect of pull-in voltage shift and the enhancement of electric field across the dielectric. However, at the present moment, we assume the parasitic charge is uniformly distributed on the dielectrics, and the area under consideration is big enough to neglect the fringing effect at the edge of the device. The model presented here can also be applied to other dielectric material systems such as silicon nitride and silicon dioxide systems.

As shown in Fig. 5-10, we assume an accumulated charge density of $\sigma_p(r)$ at the dielectric interface [14]. The capacitive system under consideration must maintain electrical neutrality because of the ground connection. Thus,

$$\sigma_1(r)+\sigma_2(r)+\sigma_p(r)=0 \tag{5.14}$$

By neglecting the fringing field outside the system, the Gauss flux theorem can be used to determine the field in the air gap and the field inside the dielectrics.

$$\begin{aligned} E_g(r) &= \frac{D_g}{\varepsilon_g} = -\frac{\sigma_1(r)}{\varepsilon_g} \\ E_d(r) &= \frac{D_d}{\varepsilon_d} = \frac{\sigma_2(r)}{\varepsilon_d} = \frac{-(\sigma_1(r)+\sigma_p(r))}{\varepsilon_d} \end{aligned} \tag{5.15}$$

Here, D_g, D_d are the electric flux densities. The voltage applied on the system can be divided into the voltage drop across the dielectrics and the voltage drop across the air gap as:

$$\begin{aligned} V &= V_g + V_d = E_g(d_g - z) + E_d d_d \\ &= -\sigma_1(r)\frac{d_g - z}{\varepsilon_g} - [\sigma_1(r)+\sigma_p(r)]\frac{d_d}{\varepsilon_d} \end{aligned} \tag{5.16}$$

Using the above equations, the charge density can be calculated as

$$\sigma_1(r) = -\frac{V + \sigma_p(r)\dfrac{d_d}{\varepsilon_d}}{\dfrac{d_g - z}{\varepsilon_g} + \dfrac{d_d}{\varepsilon_d}} = -C'V - \frac{\sigma_p(r)}{\dfrac{C_d^{'}}{C_g^{'}} + 1}$$

$$\sigma_2(r) = -(\sigma_1(r) + \sigma_p(r)) = -\frac{V - \sigma_p(r)\dfrac{d_g - z}{\varepsilon_g}}{\dfrac{d_g - z}{\varepsilon_g} + \dfrac{d_d}{\varepsilon_d}} = C'V - \frac{\sigma_p(r)}{\dfrac{C_g^{'}}{C_d^{'}} + 1} \qquad (5.17)$$

where $C_g^{'} = \dfrac{\varepsilon_g}{d_g - z}$, $C_d^{'} = \dfrac{\varepsilon_d}{d_d}$, and $C^{'} = \dfrac{1}{\dfrac{d_g - z}{\varepsilon_g} + \dfrac{d_d}{\varepsilon_d}}$

Intuitively, $C_g^{'}$ represents the capacitance per unit area of the air gap assuming the lower electrode is displaced by z, $C_d^{'}$ represents the capacitance per unit area of the dielectrics, and the $C^{'}$ represents the capacitance of $C_g^{'}$ and $C_d^{'}$ in series. The attracting force of the electrostatic actuators can be expressed as:

$$dF = -\frac{E_g dQ_1}{2} = \frac{\sigma_1(r)^2 dA}{2\varepsilon_g} = \frac{dA}{2\varepsilon_g}\left(\frac{V + \sigma_p(r)\dfrac{d_d}{\varepsilon_d}}{\dfrac{d_g - z}{\varepsilon_g} + \dfrac{d_d}{\varepsilon_d}}\right) = \frac{[V - V_p(r)]^2}{2}\frac{dC^{'}}{dz}dA \qquad (5.18)$$

$$F = \int_{(A)} dF = \frac{dC^{'}}{dz}\int_{(A)} \frac{[V - V_p(r)]^2}{2} dA \qquad \text{where } V_p(r) = -\sigma_p(r)\frac{d_d}{\varepsilon_d} = -\frac{\sigma_p(r)}{C_d^{'}}$$

So from the above equation, it is clear that the parasitic charge provides an un-wanted force shift, and this force shift causes the pull-in voltage shift. Thus, higher voltage will be required to cancel the surface potential $V_p(r)$ generated by the parasitic charge. Intuitively, to minimize this voltage shift caused by the parasitic charge (i.e. assuming the parasitic charge density remains constant), one has to either decrease the dielectric layer thickness or to use a dielectric with higher permittivity.

Theoretical investigation of pull-in effect on dielectrics-coated system

An electrostatic actuator is a nonlinear, dynamic capacitor. In general, it can be modeled by a transfer function from voltage V to charge q. As shown in Fig. 5-11, the equation of motion can be described as:

$$m\ddot{z} + b\dot{z} + kz = \frac{dC'}{dz}\int_{(A)} \frac{[V - V_p(r)]^2}{2} dA = \frac{A}{2\varepsilon_g} \frac{(V - V_p(r))^2}{(\frac{d_g - z}{\varepsilon_g} + \frac{d_d}{\varepsilon_d})^2} \tag{5.19}$$

At steady state ($\dot{z} = \ddot{z} = 0$), the equation reduces to the balance of spring force and electrostatic force. The relationship of the force and displacement can be calculated as:

$$z * (d_g + \varepsilon_g \frac{d_d}{\varepsilon_d} - z)^2 = \frac{A\varepsilon_g}{2k}(V - V_p(r))^2 \tag{5.20}$$

It is clear that at $z = \frac{1}{3}(d_g + \varepsilon_g \frac{d_d}{\varepsilon_d}) = 1/3 * d_{eff}$, the system will undergo a catastrophic unstable condition [5] and hence, the voltage required to pull the cantilever beam to $z = 1/3 * d_{eff}$ is called the pull-in voltage and can be calculated as:

$$V = V_p + \sqrt{\frac{8 * kd_{eff}^3}{9A\varepsilon_g}} = \sqrt{\frac{18EId_{eff}^3}{5\varepsilon_g L^4 w}} \quad \text{(for cantilever beam situation)} \tag{5.21}$$

The next question is how severe is this voltage shift V_p or how large is the charge σ_p that will deposited on the interface to cause the force shift.

Residual Charge calculation (I)-- Low electric field across the air gap

Consider the electric fields to be in an isotropic and linear medium. At low electric field (see region I in Fig. 5-9), the air medium is treated as a giant resistor [15].

Based upon Ohm's law, charge conservation and basic equations of classical electrodynamics under steady state, one can obtain:

$$\begin{aligned}
&\frac{\partial \sigma}{\partial t} = -\nabla \bullet j = -\nabla \bullet (\frac{D}{\varepsilon r}) = 0 \\
&\varepsilon_g E_{gn} - \varepsilon_d E_{dn} = \sigma \\
&((1/r_g)E_g - (1/r_d)E_d) \bullet n = 0 \\
&(1/r_g)E_{gn-q} - (1/r_d)E_{dn-q} = 0
\end{aligned} \qquad (5.22)$$

From the above equation, it can be seen that if the charge accumulation does not change the sign of E_n, then from the equation,

$$\sigma = \varepsilon_d E_{dn} (\frac{\varepsilon_g}{\varepsilon_d}\frac{r_g}{r_d} - 1) \qquad (5.23)$$

and

$$\begin{aligned}
&\varepsilon_g r_g = \varepsilon_d r_d \quad \text{zero charging} \\
&\varepsilon_g r_g > \varepsilon_d r_d \quad \text{positive charging} \\
&\varepsilon_g r_g < \varepsilon_d r_d \quad \text{negative charging}
\end{aligned} \qquad (5.24).$$

The above formula can be further rearranged using eq.5-17 into:

$$\begin{aligned}
\sigma_p &= \sigma_2 (\frac{\varepsilon_g}{\varepsilon_d}\frac{r_g}{r_d} - 1) \\
&= (C'V - \frac{\sigma_p}{\frac{C_g^{'}}{C_d^{'}} + 1})(\frac{\varepsilon_g}{\varepsilon_d}\frac{r_g}{r_d} - 1) \\
\Rightarrow \sigma_p &= C'V((\frac{\varepsilon_g}{\varepsilon_d}\frac{r_g}{r_d} - 1)^{-1} + (\frac{\varepsilon_g}{\varepsilon_d}\frac{d_d}{d_g - z} + 1)^{-1})^{-1}
\end{aligned} \qquad (5.25)$$

and the voltage shift V_p can be calculated as:

$$V_p = \sigma \frac{d_d}{\varepsilon_d}$$
$$= V \frac{1}{\frac{\varepsilon_d}{d_d}\frac{d_g - z}{\varepsilon_g} + 1}\left(\left(\frac{\varepsilon_g}{\varepsilon_d}\frac{r_g}{r_d} - 1\right)^{-1} + \left(\frac{\varepsilon_g}{\varepsilon_d}\frac{d_d}{d_g - z} + 1\right)^{-1}\right)^{-1} \tag{5.26}$$

Two simple conclusions can be drawn from the above equations: (1) if $\varepsilon_g r_g = \varepsilon_d r_d$, charge will not be accumulated at the dielectric/air interface and the surface potential will be $V_p=0$ (2) when $\varepsilon_g r_g << \varepsilon_d r_d$, the dielectrics/air interface will be charged to $V_p=V$. Then no voltage will be dropped across the air gap and thus no electrostatic force will be generated to pull down the cantilever beam. Of course, our case will be in-between those extreme cases and can be accounted for by the equation above.

Residual charge calculation (II)-- Saturation current-limited region

Considering the current-limited region where the current is saturated. (see region II in Fig. 5-9.)

$$j = j_0 = \frac{E_d}{r_d} = \frac{\sigma_2(r)}{\varepsilon_d}\frac{1}{r_d} = \left(C'V - \frac{\sigma_p(r)}{\frac{C_g'}{C_d'} + 1}\right)\frac{1}{r_d * \varepsilon_d}$$
$$\Rightarrow \sigma_p(r) = \left(\frac{C_g'}{C_d'} + 1\right)(C'V - j_0 r_d \varepsilon_d) \tag{5.27}$$
$$\Rightarrow V_p = -\sigma_p(r)\frac{d_d}{\varepsilon_d} = \left(\frac{\varepsilon_g}{\varepsilon_d}\frac{d_d}{d_g - z} + 1\right)\left(\frac{1}{1 + \frac{\varepsilon_d}{d_d}\frac{d_g - z}{\varepsilon_g}}V - j_0 r_d d_d\right)$$
$$\approx -j_0 r_d d_d$$

From eq. 5.27, we can calculate the results shown in Fig. 5-6. The voltage shift of 120V in our example would correspond to a saturation current of $j_0=8*10^{-8}V/m^2$ and an

accumulated charge density of $1.3*10^{-3}C/m^2$. Moreover, if we assume that the current density at 120V reaches saturation current using the resistor model in the previous section, the density should reach approximately $j_0=8*10^{-8}V/m^2$, giving us:

$$\frac{\varepsilon_g}{\varepsilon_d}\frac{r_g}{r_d} \approx 10^{-3} \qquad (5.28).$$

This result is consistent with our model that the resistivity of air is smaller than that of Parylene dielectric. Therefore, the charging mechanism is two-fold. First, the Parylene would be charged to the applied potential when the voltage increases until the saturation current density is reached. Beyond that point, the voltage applied would generate an electric field in the air gap and pull-in the cantilever beams.

5.4 Experimental Results and Discussion

In this section, the phenomena described in section 5.2 such as high-threshold and bounce-back will be explained in terms of the theoretical and experimental results. Some of the new effects such as snap-down and threshold-voltage shift will also be discussed here. In addition, previous devices directly or indirectly showing air breakdown and dielectrics charging will be reviewed and discussed.

5.4.1. High threshold voltage

In Section 5.2.2, a high threshold voltage phenomenon was discovered. As shown in Fig. 5-6, the calculated threshold voltage is much lower than the experimental values with a constant voltage shift around 120V. This phenomenon is actually one of the main motivations for studying the parasitic charging effect at the Parylene/air interface. It is

clear now that the threshold voltage can be explained using the theory developed in the previous sections.

When the electric field across the air gap is lower than 3MV/m, the air acts as the perfect insulator, and the cantilever beam can move with the voltage signal according to traditional pull-in theory. As shown in eq. 5.18, the movement can be determined by setting $V_p=0$. However, in our experiments, even the longest beam with pull-in voltage less than 1V has a threshold voltage shift around 120V. This could be due to the errors from the calculation of the theoretical threshold voltage. While calculating the pull-in voltage, the cantilever beam is assumed to be extremely flat without corrugation. However, the corrugation (posts) here is necessary to prevent stiction as described from the last chapter. Second, the calculation neglects the stresses inside both Parylene and thin-gold electrodes. This could also induce calculation errors. Therefore, the estimated pull-in voltage should be higher than the calculated value even by the first factor alone. As a result, when the electric field inside the air gap is less than 3MV/m, no Parylene cantilever beam moves with the excitation voltage.

The second region starts with the electric field within the air gap exceeding 3MV/m, the maximum safe operation region for the air medium. Breakdown should happen and may be accompanied with initial ionization. However, because of Parylene is an insulator, those breakdowns should be transient. Once the air breaks down, the conductivity of air becomes significantly higher than that of Parylene. According to eq.5-26 described in Section 5.3, the Parylene surface will be charged to nearly the negative of the excitation voltage and thus, very little of the electric field will drop across the air gap. As a result, the Parylene cantilever beam will remain freestanding with this voltage range.

The third region starts when the electric field inside the air gap that is large enough to initiate the saturation current mode. As shown in Fig. 5-9, the saturation current can sustain a large voltage change without significantly changing the current magnitude. Thus, according to the eq. 5.15, the electric field inside the air gap starts to increase with excitation voltage and of course, some of the voltage will be used to compensate the parasitic charge deposits during currents shown in Fig. 5-9 region I. As in eq. 5.27, the surface potential is approximately $V_p \approx -j_0 r_d d_d$.

Thus, the effect of this high-threshold voltage clearly comes from the high resistivity Parylene material used here. The saturation charging current should remain universal, since most of the measurements were made in ambient atmospheric conditions. However, to the author's knowledge, no one has quantified this parameter in great detail. It is also possible that this parameter may vary significantly with light, humidity, temperature, and even cosmic rays. Although somewhat thick, the thickness of dielectrics is within the reasonable range of most micromachined devices.

In conclusion, the resistivity of Parylene is higher than the air medium when the electric field is larger than 3MV/m. This high resistivity causes the residual parasitic charge to start to accumulate on the surface. However, when the surface accumulates the charges, current conducts through both air and Parylene samples until the saturation current density is reached. At this point, the residual charge density stops increasing and the electric field inside the air gap starts to build up and finally pulls in the cantilever beams.

5.4.2. "Bounce-Back" effect

This section qualitatively explains the "bounce-back" effect that has been described in the beginning of the chapter. This is the most important reason to study the parasitic charging effect in Parylene electrostatic actuators. Similar phenomena have been reported but never studied [14, 16]. When applying a high voltage excitation signal on the actuators, the actuators will first touch the substrate but will eventually bounce back from the substrate while the voltage is still on. This phenomenon may be caused by several reasons.

First of all, as we have explained earlier, the breakdown of air molecules can generate extra charges, and those charges can travel under the influence of the electric field and deposit on the Parylene/air interface. The dielectric strength of an air gap can be represented by Paschen's curve, which the plots the breakdown voltage against the pressure-distance product. The absolute minimum for the air molecule is V_{br}=340V at pd=6-8 bar-μm. It is important to realize that the breakdown described by Paschen's curve is not the same as the breakdown region described above. Thus, *pd* of our experimental samples fall right on this range before the actuator touches the substrate. When the actuator moves closer to the substrate, the *pd* product decreases, and so the breakdown voltage for the Paschen's curve should increase accordingly. However, as described in section 5.3, many researchers have concluded that Paschen's curve is not only applicable for electrodes spaced larger than 4 μm apart; even 20V can breakdown air at an electrode spacing of 1 μm. Thus, it is very likely that the extra charges are caused by breakdown of air molecules.

Second, it is well known that extra charges can be generated by contacting an insulator surface with a metal. For example, Cunningham used an etched gold-coated tungsten wire as the probe of a potentiometric scanning probe microscope [17] on which films of PMMA were contacted. After contact charging a surface, the probe is then raised about 50nm above the surface, at the position in which it is used to monitor the surface potential below it. PMMA was found to first charge positively and then negatively over five successive contacts. Thus, it is possible that the contact between the cantilever beam and the substrate covered with a gold electrode generates excessive charges and therefore bounces the cantilever back. The space charge generated in Parylene in the high-field region (see Chapter 2) could also generate the extra charges that bounce back the cantilever [18].

A test was made to determine which of the above hypotheses contributed mainly to the bounce-back effect. A device was packaged and wire-bonded into a vacuum chamber. If the breakdown of the air molecules causes the effect, then at extremely high vacuum where the mean free path of the air molecules is much larger than the electrode spacing, there will not be enough molecules to break down and thus, no bounce back effect will be observed. Otherwise, if the charge is generated through contacting the insulator with metal, then the bounce-back effect should still be expected, because the contact charge will still be generated to bounce back the cantilever beam.

The devices were packaged and tested in two different degrees of vacuum. One is at a higher vacuum $\sim 10^{-6}$ torr and the other at a lower vacuum around 200mtorr. The devices under lower vacuum (200mtorr) still showed a strong bounce-back effect after several cycles of operation. However, at higher vacuum, the bounce-back effect was not

observed. The threshold voltage also decreased significantly and became closer to the theoretical values. The deviation of the theoretical values and the experimental values show that residual charge still exists at Parylene/air interface. The effect of air breakdown had almost been diminished.

In conclusion, the bounce-back effect can be explained as follows. When the cantilever beam moves closer to the substrate, the air continues to breakdown. When the cantilever beam touches the substrate, the electric field developed across the air gap becomes enormously high (the actual value depends on how close the cantilever beam is to the substrate) and thus the air breaks down and deposits excessive charges at the Parylene/air interface. After the beam is bounced-back to the original position, the electric field across the air gap is so low that it is not large enough to bring down the cantilever beams. Hence, the beams are left in the freestanding position even when the excitation voltage is still on.

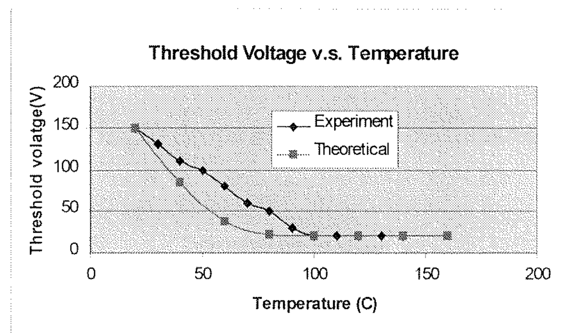

Fig. 5-12: Threshold voltage of electrostatic actuator as function of temperature

5.4.3. Temperature effects

It is also very interesting to note that the pull-in voltage of the Parylene cantilever system studied here changes with temperature as shown in Fig. 5-12. It is known that the

resistivities of polymers change with temperature and thus, polymers have large temperature coefficients of resistance (TCR) compared to metals. As provided by the manufacturer, the resistivity of Parylene undergoes large changes over the temperature range from 20°C to 150°C as shown in Fig. 2-14. The testing temperature is limited to 150°C because of the melting point of the Parylene material. In addition, studies from the manufacturer show that the Parylene surface undergoes oxidation processes in an environment where the temperature is higher than 100°C, causing the material to become crystalline and brittle.

The maximal parasitic charge on the Parylene/air interface (see eq.5-27) can be calculated as $V_p \approx -j_0 r_d d_d$; thus the threshold voltage shift should be a linear function of resistivity of Parylene dielectric. As the temperature increases, the resistance of the Parylene dielectrics drops and so do the parasitic maximal charges. As the residual charges (surface potential) drop, the voltage required to pull in the cantilever beam drops accordingly. As shown in Fig. 5-12, the pull-in voltage of the cantilever beam (400μm long*200μm wide *2.5μm high) drops as temperature increases.

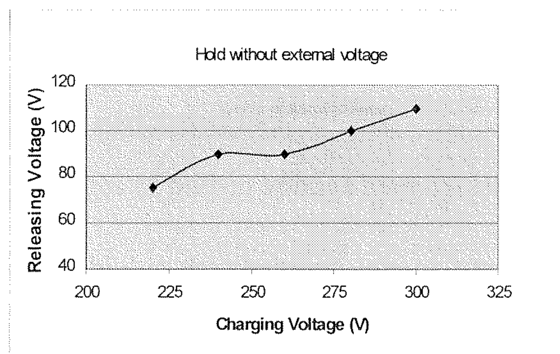

Fig. 5-13: "Snap-down" effect– The Parylene dielectrics would be charged permanently and require an external voltage to bring it up.

5.4.4. Permanent charge damage—"Snap-down" effect

Repetitive operation of the cantilever system under high voltage will finally damage the material and cause the charge to be permanently stored in the Parylene dielectric. This effect can be demonstrated by a cantilever beam undergoing repetitive high-voltage ON/OFF cycles. The cantilever will first bounce-back as described by the previous sections. However, after repetitive cycles at a high voltage (200V-300V), or an equivalent electric field (0.8MV/cm to 1.2MV/cm), the cantilever beam will automatically pull-in when the external voltage is released. This force to pull in the cantilever beam is created from the residual parasitic charges stored inside the Parylene dielectrics. Thus, when the cantilever snaps down on the substrate, an extra voltage is required to pull the cantilever up to the original freestanding position. This voltage as shown in the figure is a function of the voltage at which the cantilever repetitively undergoes.

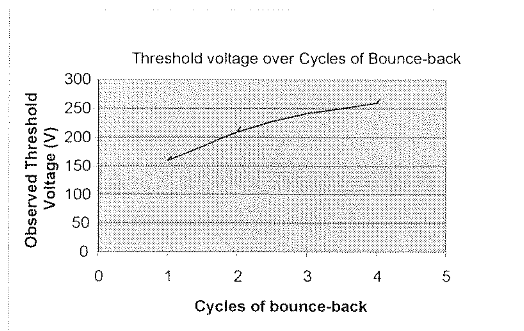

Fig. 5-14: Changes of pull-in voltage over cycles of "bounce-back"

It is clear that the higher the charging voltage, the higher the extra voltage has to be to pull back the cantilever. Thus, we can conclude that the higher the voltage, the more damage it can do to the Parylene and thus more residual charges can reside in the Parylene thin film when the voltage is removed. To prevent permanent charges from

residing in the Parylene thin film, the devices have to be operated at lower electric field regions (0.8MV/cm).

5.4.5. Threshold voltage shift with cycles of operations

It has also been found experimentally that the pull-in voltage of the cantilever gradually increases with cycles of high-voltage operation (see Fig. 5-14). Thus, it is possible that after every cycle of bounce-back, the surface potential is created to nullify the electric field in the air gap. After this voltage is released, most of the residual charges are released as well. Some residual charges may still exist either at the Parylene/air interface or inside the Parylene dielectrics. Thus, the subsequent voltage will have to nullify the effect of the residual charges to change the direction of the electric field inside the air gap. This voltage is consumed to balance the effect of the residual charges. Over cycles, when the residual charges of the cantilever beam increase, the pull-in voltage will increase accordingly to balance the residual charges.

5.5 A Normally-Open In-channel Microflow Restrictor

In this section, a normally open in-channel microflow restrictor will be developed and tested using the fundamental knowledge described in the previous sections. As shown in Fig. 5-2, in-channel fluidic components have the advantage of minimizing the dead volume. The dead volume is usually defined as the volume of sample fluid that would never arrive in at the detection section. Using the in-channel mechanism, the dead volume is dropped from typically μl to nl range. The reason why the electrostatic actuation is explored here is because, as discussed earlier in Chapter 1, electrostatic

actuation has the advantage of low power consumption and, most importantly, a possibility of high integration level. The original valve is intended for "lab-on-the-chip" applications which attempts to miniaturize all the microfluidic components of the system such as sample preparation and flow control unit (valves, pumps, mixers) on the same single chip.

This section is divided into two subsections. The first section will discuss the original buckling concepts, and measurements taken on the initial prototype. The second section will be focused on the modified microvalve (flow restrictor) design and its results.

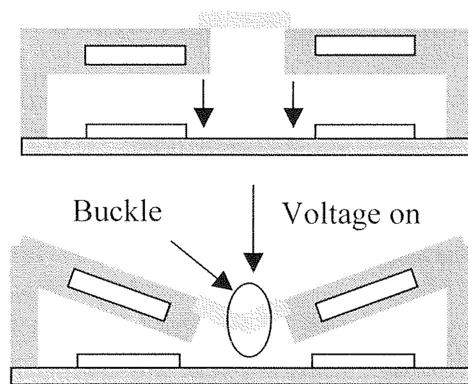

Fig. 5-15: The original idea of buckling valve

5.5.1 Initial buckling valve concepts and problems

As shown in Fig. 5-15, the original idea for a buckling valve was to apply an electrostatic force on two clamped structures with a freestanding microfluidic channel on top. The processes for making this microvalve are similar to those developed in Chapter 4, and the processes used to fabricate the electrostatic actuators (except for the extra lithographic steps) are used to generate the freestanding channel on top. The electrostatic force would bring down the structure and force the channel to change dimension and buckle in the middle to restrict the flow.

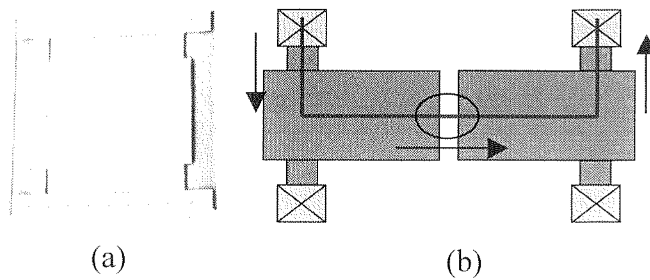

Fig. 5-16: The initial prototype of buckling valve—torsional plates
(a) SEM pictures (b) schematic

Initially, two different structures were under consideration. One is the torsional type (see Fig. 5-16); the microfluidic channel is suspended across two torsional plates. The other is the cantilever type (see Fig. 5-17) where the channel is freestanding on two cantilevers. The device sizes are the same for both designs (200μm*200μm plate, 5μm air gap). The spacing between the two plates is kept at 50 μm apart. If the spacing is too small, the channel would become too rigid and difficult to buckle. However, if the spacing is too large, the channel may not be freestanding and the buckling may not be able to restrict the flow.

Both types of microvalves are electrostatic actuated. However, two major problems were raised. First, the center part of the channel, which is supposed to be buckled, showed no signs of compression. Moreover, observations under the microscope indicate that the channel was stretched rather than compressed. Therefore, the buckling mechanism shown in Fig. 5-15 is not practical. The second problem is the aforementioned "bounce-back" problem that has been studied earlier. The valve would not make permanent contact with the substrate under the actuation voltage used here (400-700Volt). Therefore, in the remainder of the work, only the AC-actuation tests were performed; the microvalve could only stop the flow for a period of time for each cycle.

Thus, the device is a microflow restrictor rather than a true microvalve, which can control the flow rate at nl/min range if the application demands it.

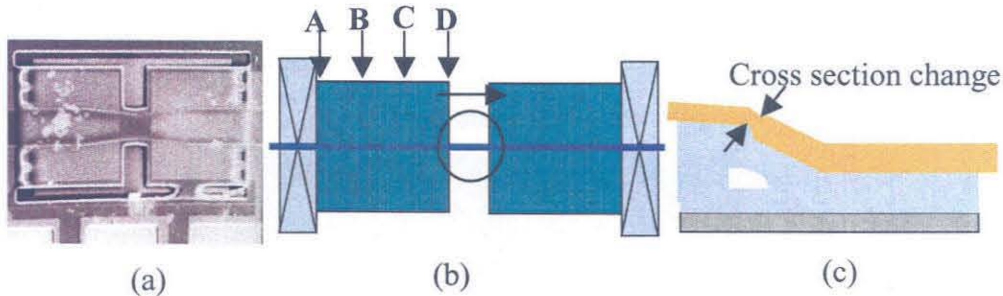

Fig.5-17: The initial prototype of buckling valve—cantilever plates
(a) SEM pictures (b) schematics (c) alternative mechanism to stop the flow

A second mechanism of stopping the flow may be possible, as shown schematically in Fig. 5-18. By pushing the freestanding channel down for a long distance (pre-determined by the air gap), the cross-section of the flow channel at the corners could change the cross section and therefore change the flow rate or even stop the flow.

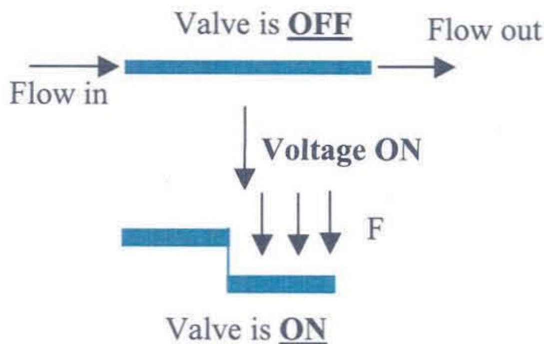

Fig. 5-18: The modified concept for in-channel flow restrictor—bending the microfluidic channel

The first cantilever-beam prototype (see Fig. 5-17) used to test the buckling principle is used here again to test the validity of this concept. The flow rate of the channel is plotted against the inlet pressure up to seven psi (see Fig. 5-19). The measured flow rate is around 20.5 nl/min/psi using the liquid displacement method (to reach 1 μl)

similar to the one used in Chapter 3. Because the time for data collection is long (e.g. at 1 psi, it would take around 45 minutes to reach 1μl), the inlet pressure used afterwards was 2 psi to reduce the data collection time.

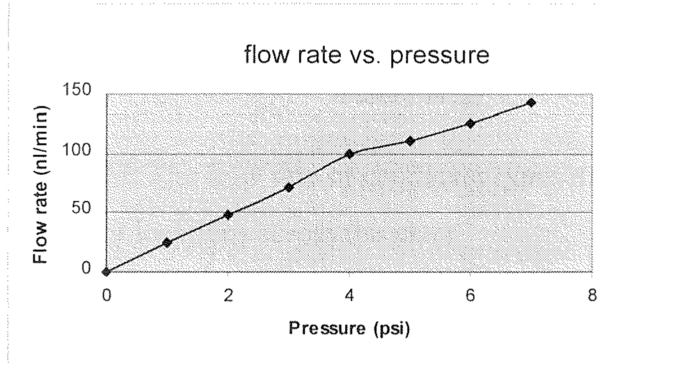

Fig. 5-19: The flow rate vs. inlet pressure for cantilever type flow restrictor

Once the channel was calibrated, the probe tips were used to push the cantilever plate down (see Fig. 5-17) at A,B,C, and D, each separated by 50 μm. The measured flow rates at two psi are shown in Fig. 5-20. The data from Fig. 5-20 suggest that in order for the bending mode to restrict the flow, the plate has to undergo larger deflections to make abrupt changes on the corners to change the cross section. A new type of the flow restrictor has to be designed to fulfill those requirements.

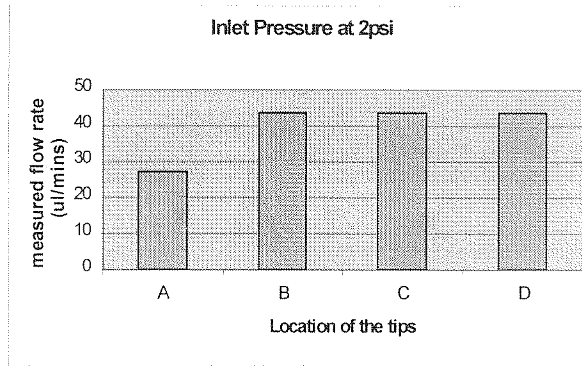

Fig.5-20: The flow rate of cantilever types measured along different locations across the plate

5.5.2 Design and characterization of modified microflow restrictor

From the results presented in the last section, in order to make the cross section of the flow channel change tremendously under electrostatic actuation, the traveling distance has to be increased. Moreover, the stress concentration point also has to be designed in such a way as to force the change of the channel cross-section at pre-determined locations. The corners of the cantilever beam designed in the last section are not rigid enough and can be moved during the actuation; this would significantly reduce the effect of bending and the capability to restrict the flow. The modified design (see Fig. 5-21) uses a sharp edge to create the stress concentration point and to force the channel bending over the area. The distance L is kept to a minimum, which helps to maximize the bending of the channel.

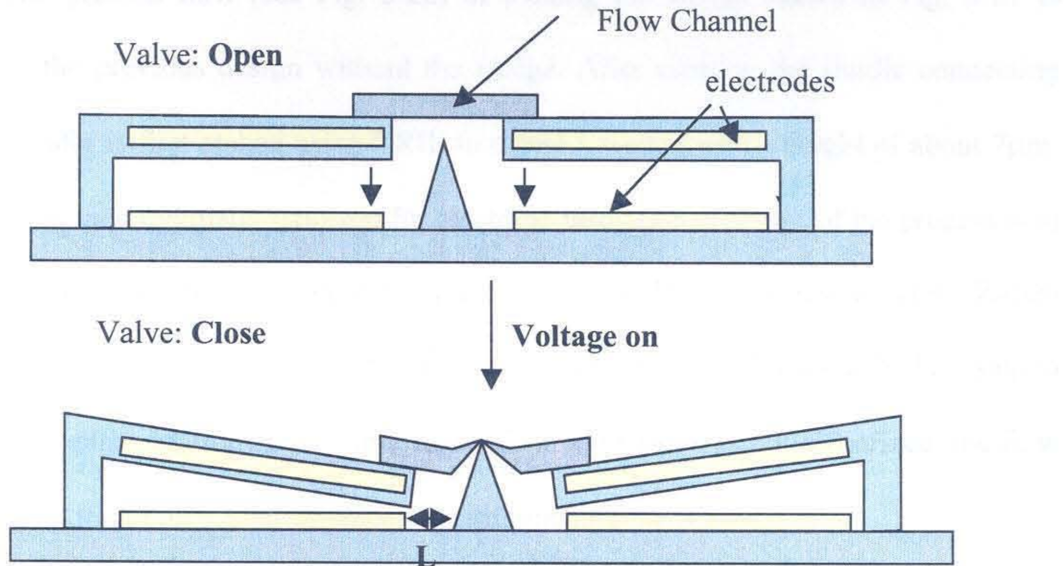

Fig. 5-21: The modified design of in-channel flow restrictor with wedge

1.DRIE wedge + thermal oxidation 1um

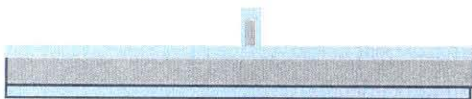

2.Bottom electrode evaporation / post hole definition

3. 1st layer Parylene deposition /post hole definition

4. 1st photoresist sacrificial layer definition

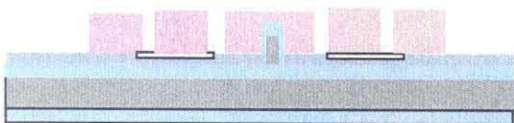

5. 2nd Parylene deposition + post formation + 2nd metal evaporation

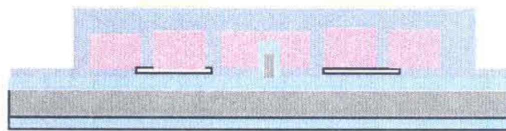

6. Define channel, 3rd Parylene deposition and pattern the channel+actuator

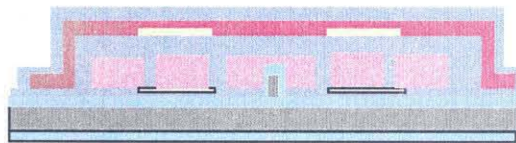

7. Acetone release and BrF_3 release posts

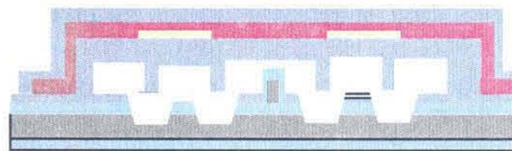

Fig. 5-22: The simplified process flow for in-channel flow restrictor with wedge

The process flow (see Fig. 5-22) of making the wedge shown in Fig. 5-21 is similar to the previous design without the wedge. After creating the fluidic connecting port, the wafer is first etched using DRIE to create a wedge with a height of about 7μm. The wafer is then thermally oxidized for electrical insulation. The rest of the process is to create the post discussed in Chapter 4 to prevent stiction. The wafer is spun with AZ4620 to planarize the surface and at the same time create a high sacrificial layer thickness up to 12 μm. This planarization step is important; if the top surface is not planarized, the flow channel may travel for a long distance without touching the wedge.

As will be shown later, AZ4620 has excellent planarization capability, and the surface of the structure is very smooth. The next steps are used to create the freestanding channels that will finally touch the wedge. The top and bottom channel walls were designed to have minimum Parylene thickness (~2μm) to enhance change in the cross-section when touching the wedge. Finally, the structures were released in acetone and BrF_3 as discussed earlier in Chapter 4.

The finished device (see Fig. 5-23) still incorporates cantilever beams with a freestanding channel on top. In the middle, there is a wedge with a height of 7 μm, and an air gap of around 10 μm. The cantilever plates are 300 μm*300 μm which can be calculated by the number of posts on the figures (post spacing are 50μm). The wedge width is minimized to 5 μm to simulate the effect of the sharp edge. Moreover, the SEM photos in Fig. 5-24(a) indicate that the planarization by photoresist is excellent. The freestanding channel is indeed parallel to the substrate, which is ideal for our applications.

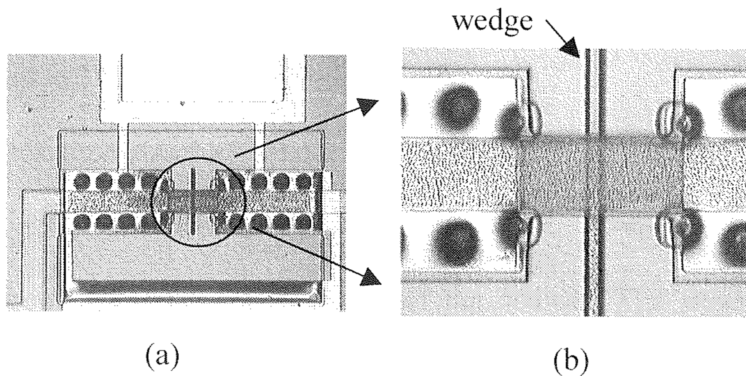

Fig. 5-23: The finished in-channel flow restrictor with wedge

(a) Picture of the whole device

(b) The enlarged view of the wedge area

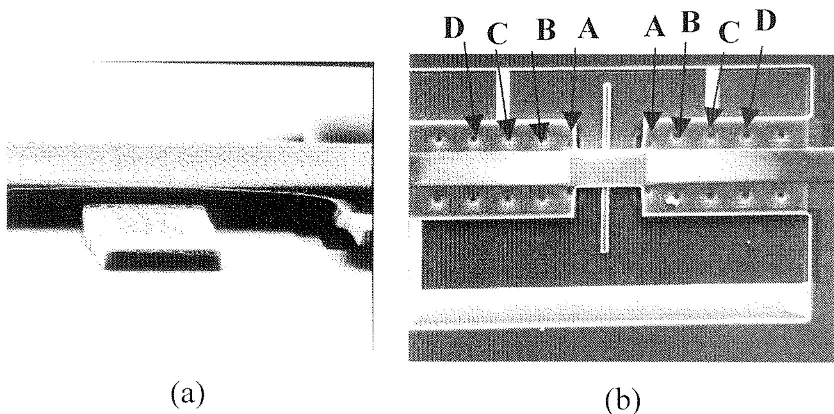

Fig. 5-24: The SEM photo finished in-channel flow restrictor with wedge

(a) Side view showing good planarization capability of AZ4620

(b) The overall structures (marks are used for probe to test the flow rate)

A similar channel flow calibration was also done for the device shown here (see Fig. 5-25). The measured flow rate is somewhat higher than the previous one. The deviation may well come from the channel size and flow path differences. The probe test along the cantilever (A,B,C,D as shown in Fig. 5-24(b)) was also performed at an inlet pressure of two psi with the results given in Fig. 5-26. This result is promising because

the probe at location A where the electrodes are designed can an achieve ON/OFF flow rate ratio of up to 380%.

The designed structure cannot make permanent contact with the substrate due to the charging effect discussed earlier in this chapter. An ac-voltage of 450 volt at 20 Hz was used when measuring the flow rate of the devices. The experimental results are shown in Fig. 5-27. At two psi inlet pressure, the achieved ON/OFF flow-rate ratio is reduced to around 200%, which is significantly less than 380% achieved using probe tips. This result is not surprising because the plate only remains on the substrate for half of the time, so the flow rate that can be changed is only 50%. Taking a 50% of the duty cycle into consideration, the achieved ON/OFF ratio is indeed around 380% if the device could be dc-actuated. Moreover, this result indirectly suggests that the time constant required for the charging effect to take place is longer than 50 ms. It is possible to design other microfluidic components such as mixers and pumps using Parylene electrostatic actuators because these applications would prefer AC-actuation.

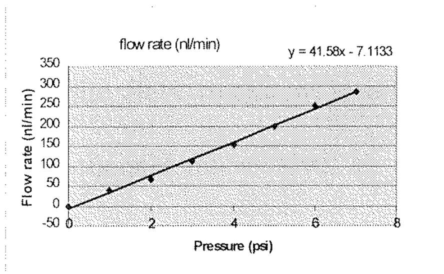

Fig. 5-25: The flow rate vs. inlet pressure for cantilever type flow restrictor with wedge

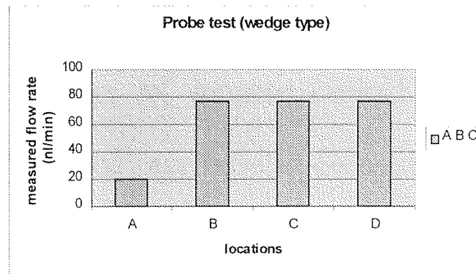

Fig. 5-26: The probe test for cantiever type flow restrictor with wedge

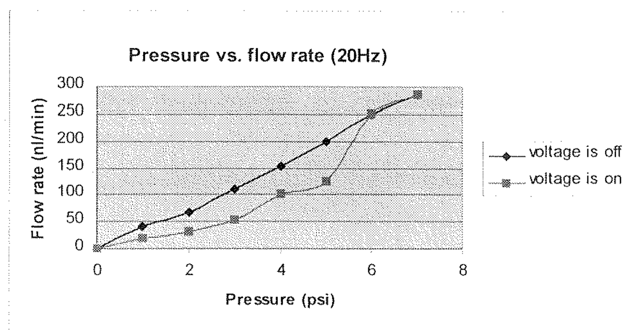

Fig. 5-27: The measured flow rate against inlet pressure using ac-actuated electrostatic force at 20Hz (with a duty cycle of 50%)

From Fig. 5-27, we can see that the flow restrictor loses its capability to modulate the flow rate at high pressures. Under microscope observation, it would be clear that the freestanding channel becomes much more rigid under a higher inlet pressure. Therefore, the voltage used is only able to pull-down the side of the cantilever but not the central part that has freestanding channels running across it.

In this section, an in-channel microflow restrictor using Parylene technology has been demonstrated. The demonstrated flow restrictor can change the flow at an ON/OFF ratio of up to 380% at two psi inlet pressure. However, because of the charging effect of Parylene, the flow restrictor is only operated in an AC-actuated method. To make a perfect in-channel microvalve, an alternative method may have to be used to enable a larger traveling distance for the plate, so the channel on top would completely change the cross section of the flow channel. Moreover, some other actuation, such as electromagnetic actuation, may have to be explored for large deflection applications.

5.6 Conclusion

In this chapter, Parylene-based electrostatic actuators have been designed, fabricated and tested. The un-desired charging effect on Parylene dielectrics has been investigated in detail to understand various problems caused by residual-charge such as high threshold voltage, bounce back, snap-down, temperature-caused pull-in voltage shift, and hysteresis. In the second part, a novel in-channel microflow restrictor is also demonstrated using Parylene electrostatic integration technology to achieve ON/OFF flow ratio up to 200% at 400V, 20Hz operation. The flow restrictor can achieve an ON/OFF flow rate ratio of up to five psi while having minimum dead volume.

Electrostatic actuators, especially those that have dielectrics in the air gap, should be designed for use in the low electric field range (preferably less than 3MV/m). Although most of the dielectrics used in micromachining such as silicon dioxide and silicon nitride have resistivities of several orders of magnitude lower than the Parylene studied here, undesired effects such as bounce-back and threshold voltage shift would become a more severe issue after repetitive operations. Therefore, two different methods can be used to avoid this charging problem completely. First, the dielectrics in the air gap could be eliminated entirely. In our case, the photoresist sacrificial layer has to be modified so the top metal electrodes can be deposited and patterned. Second, the voltage electrode used to drive the actuator should be separate from the signal electrodes so that the signal electrodes are not in close proximity to the dielectric. In the next chapter, an electret microphone will be designed and characterized. The electric field intensity in the microphone is carefully designed to avoid the charging problem.

5.7 References

[1] J. M. Giachino and T. J. Miree, "The Challenge of Automotive Sensors," SPIE Conference on Microlithography and Metrology in Micromachining, Austin, TX, 1995.

[2] L. J. Hornbeck, "Digital Light Processing and MEMS: Timely Convergence for a Bright Future," Proceedings of the SPIE Workshop on Micromachining and Microfabrication Processes, Proceedings of the SPIE- The International Society for Optical Engineering, Austin, TX, Oct. 23-24, 1995.

[3] S. Singh-Gasson, R. D. Green, Y. J. Yue, C. Nelson, F. Blattner, M. R. Sussman, and F. Cerrina, "Maskless fabrication of light-directed oligonucleotide microarrays using digital mirror array," *Nature Biotechnology*, vol.17, pp.947-978, 1999.

[4] P. Dario, M. C. Carrozza, A. Benvenuto, and A. Menciassi, "Micro-systems in biomedical applications," *J Micromech Microeng*, vol.10, pp.235-244, 2000.

[5] K. E. Petersen, "Silicon as a Mechanical Material`," *Proc IEEE*, vol.70, pp.420-457, 1982.

[6] L. D. Edmonds, G. M. Swift, and C. I. Lee, "Radiation Response a MEMS Accelerometer: An Electrostatic Force," *IEEE TRANSACTIONS ON NUCLEAR SCIENCE*, vol. 45, pp. 2779-2788, 1998.

[7] A. R. Knudson, S. Buchner, P. McDonald, W. J. Stapor, A. B. Campbell, K. S. Grabowski, D. L. Knies, S. Lewis, and Y. Zhao, "The effects of radiation on MEMS accelerometers," *IEEE TRANSACTIONS ON NUCLEAR SCIENCE*, vol. 43, pp. 3122-3126, 1996.

[8] R. Rettig, M. Kassens, and L. Reimer, "Measurement of Specimen Charging in Scanning Electron Microscopy with a Kelvin Probe," *Sanning*, vol.16, pp.221-226, 1994.

[9] L. Reimer, U. Golla, R. Bongeler, M. Kassens, B. Schindler, and R. Senkel, "Charging of bulk specimens, insulating layers and free-supporting films in scanning electron microscopy," *Optik*, vol. 1, pp. 14-22, 1992.

[10] A. D. Moore, *Electrostatics and Its Applications*, ed. 1, John Wiley & Sons, Inc., 1973.

[11] Sedlacek, *Electron Physics of Vacuum and Gaseous Devices*.Stockholm, Sweden, John Wiley & Sons, Inc., 1996.

[12] L. H. Gemer, "Electrical Breakdown between Close Electrodes in Air," *Journal of Applied Physics*, vol. 30, pp. 46-51, 1959.

[13] J.-M. Torres and R. Dhariwal, "Electric field breakdown at micrometre separations," *Nanotechnology*, vol. 10, pp. 102-107, 1999.

[14] Jürgen Wibbeler, Günter Pfeifer, and M. Hietschold, "Parasitic charging of dielectric surfaces in capacitive microelectromechanical systems (MEMS)," *Sensors and Actuators A*, vol. 71, pp. 74-81, 1998.

[15] F. Sauli and A. Sharma, "Micropattern Gaseous Detectors," *Annual Review of Nuclear Particle Science*, vol. 49, pp. 341-388, 1999.

[16] P. Cheung, A. A. Berlin, D. K. Blegelsen, W. B. Jackson, and R. Lau, "Experimental Characterization of Printed Circuit Board-Based Cantilever Air Valves", 2000.

[17] S. Cunningham, "Dynamical studies of the single point contact electrification of inorganic and polymer substrates," *Journal of Electrostat*, vol. 40, pp. 225-230, 1997.

[18] T. Mori, T. Matsuoka, and T. Mizutani, "The Breakdown Mechanisms of poly-p-xylyene Film," *IEEE Transactions on Dielectrics and Electrical Insulation*, vol.1, pp. 71-76, 1994.

CHAPTER 6

Thin-Film Teflon Electret Microphone with Parylene Back plate

Abstract

In this chapter, a condenser electret microphone will be demonstrated and characterized. The condenser microphone, which is in principle a capacitive sensor, uses electrostatic force to measure the level of the sound waves. The electret, which has permanent charges buried inside, provides built-in electric field; therefore no external electrical bias is required to power the microphone itself. The demonstrated microphone has a sensitivity reaching up to 45mV/Pa with a bandwidth greater than 10KHz, and with less than 1% of Total Harmonic Distortion (THD) at 650Hz.

6.1 Preface

The microphone in principle is a pressure sensor that measures the pressure differences generated by sound waves. Therefore, many methods applied to pressure sensors are also applied to the microphone. However, for a microphone design consideration, several aspects are different from the pressure sensor. For example, the microphone is not used to measure the DC pressure changes, but instead measures the differential pressure changes so that changes in the barometric pressure would not cause drifts in the output sound level. Second, the bandwidth is usually limited to 20 Hz to 10

KHz for the microphone, which is the normal audible range for human beings. Third, microphones, especially those for hearing aid and calibration applications, should have little noise. Fourth, the microphone should have at least a dynamic range (the range in which the microphone can sense the input sound level) from 30dB SPL to 100dB SPL. The dB SPL(Sound Pressure Level) is the unit used to measure the acoustic level and is defined as:

$$dB\,\mathrm{SPL} = 20\log_{10}\frac{\text{rms pressure in Pa}}{20*10^{-6}\ \mathrm{Pa}}. \qquad (6.1)$$

The $20*10^{-6}$Pa is recognized as the minimum sound level that humans can sense and therefore is used as a reference level. The sound level over 140 dB SPL is usually defined as the threshold of pain.

Over time, many different microphone architectures have been proposed. Among them, the most important are piezoresistive[1], capacitive[2], and piezoelectric[3] microphones. Piezoresistive microphones make use of a diaphragm incorporating four piezoresistors in a Wheatstone bridge configuration, and they usually have sensitivities in the range of 25μV/Pa. The piezoelectric microphone makes use of a piezoelectric material that is mechanically clamped to the diaphragm; the sensitivity is usually at 50 to 250μV/Pa. The most common architecture for microphone by far is capacitive, or condenser microphone as shown in Fig. 6-1. They can be roughly divided into two categories—external biased or self-biased (electret). The principle of capacitive microphone is that while the sound waves impinge on the diaphragm, the diaphragm would move according to the pressure differences. Therefore, the overall capacitance changes and an ac-sinusoidal electric signal would be generated. For an externally biased microphone, the sensing is achieved by the electric field generated by an external bias.

For the electret microphone, the electric field is generated by permanent buried charges in dielectrics (electrets). The generated electric signal is buffered through a pre-amplifier, which provides high input impedance and unit gain. The signal is then further amplified to drive the speaker circuitry.

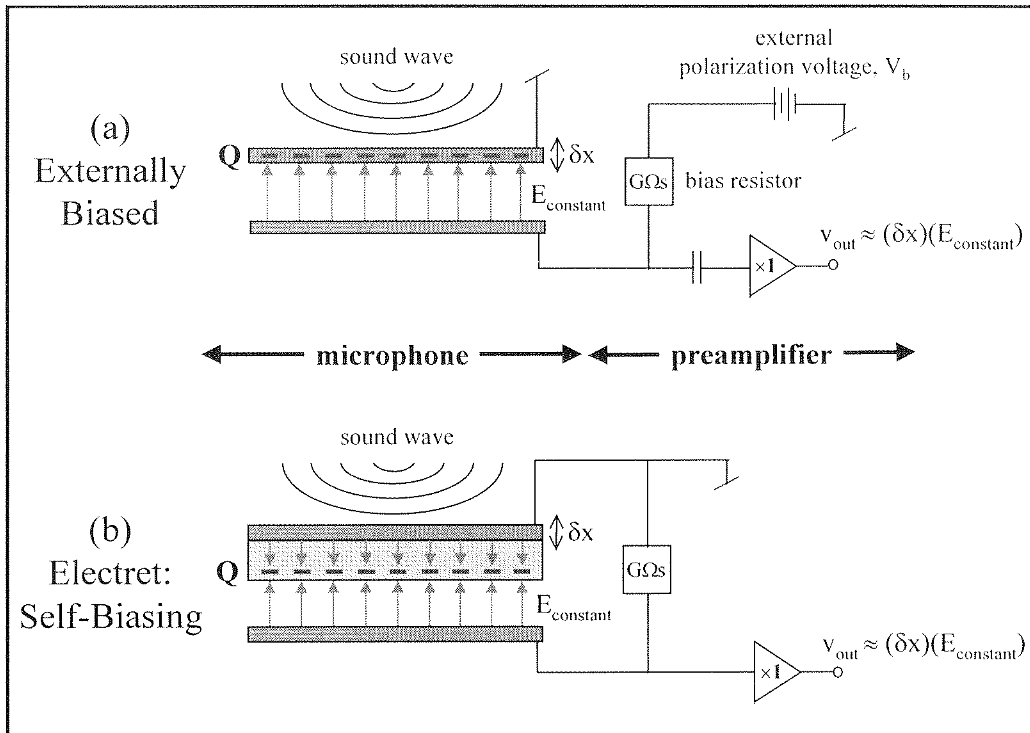

Fig. 6-1: Externally biased and self-biasing (electret) condenser microphones

As far as today, most microphones used in hearing aid, performing arts, or even cellular phones are electret microphones. Since electret microphone inherently do not require an external power supply, the noise level in electret microphones are typically much lower than the external-biased condenser microphones.

This chapter will be subdivided into three sections. In Section 6.2, the fabrication process will first be described to reveal the architecture of the electret microphone. Then, theoretical design consideration for an electret microphone will be discussed. The characterization of the electret microphone will be presented in Section 6.3.

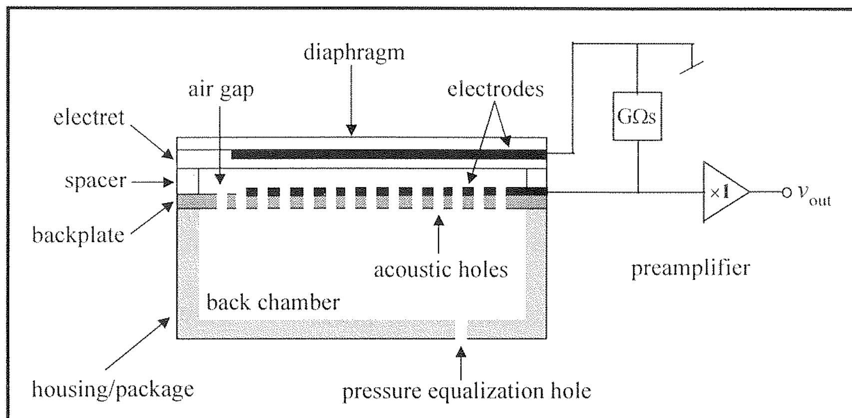

Fig. 6-2: Schematics of an electret microphone

6.2 Design of an Electret microphone

As shown in Fig. 6-2 [9], an electret microphone typically consists of five important components. First, there is a top diaphragm with metal electrodes on which the sound wave will impinge. The diaphragm has to be soft enough so the mechanical sensitivity of the microphone will be reasonable (the diaphragm will actually move). However, by softening the diaphragm, the bandwidth of the diaphragm would be significantly reduced. Therefore, those two issues have to be compromised.

Second, a back plate is required both for providing the other sensing electrode and also for reducing the air-streaming resistance (i.e. damping from the air). This back plate should be designed to be as strong as possible so that it would not move with the sound waves. However, there is another compromise for designing the backplate. The back plate is required to have many acoustic holes to reduce air damping the confined air gap area. If there are no acoustic holes, the air has to be squeezed out of the microphone through the side of the diaphragm, and the overall frequency response of the diaphragm would be significantly decreased. However, by increasing the density of the acoustic

holes, the area of the electrodes also decreases and reduces the overall sensing capacitance. These two issues have to be compromised.

Third, the electret material covered on top of electrodes of the moving diaphragm has to be studied in detail to provide a stable built-in electric field. The electrons buried in the electrets (in this case, a Teflon AF thin-film) have to have long life times for several years and a charge density high enough to provide a strong built-in electric field. Furthermore, the electret material should have minimum effects to change in ambient humidity or temperature.

Fourth, a spacer that separates the top and bottom electrode has to be high enough so the dynamic range of the microphone is reasonable. The air gap also has to be designed so the electric field generated by electrets would not break down the air molecule and cause the undesired charging effect as discussed earlier in the last chapter.

Fifth, the housing and packaging of the microphone should furnish a large enough volume to provide constant pressure. A pressure equalization hole is usually used to maintain the pressure equilibrium.

Sixth, a pre-amplifier that has several GΩ input impedance is also required to match the output impedance of the microphone, which is also in several GΩ range at low frequency.

This section will focus on the design issue of an electret microphone. First, the output sensitivity will be formulated and the frequency response will be considered. Second, the effect of the acoustic holes in backplates will be investigated. Third, the electret material, thin-film Teflon AF, will be overviewed with its charge holding capability; the method of electron implantation using BLT (Back-light Thyratron) [4] into

the electret will also be reviewed. Finally, a series of design parameters for the electret microphone will be given using the conclusion from the above discussion.

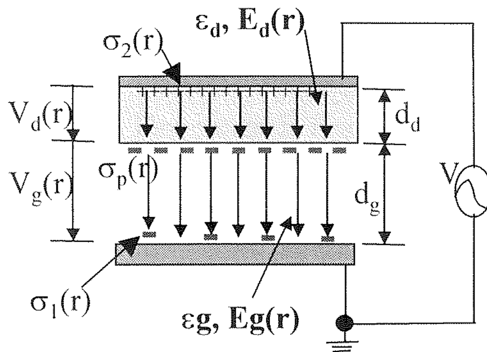

Fig. 6-3: Schmeatics of Teflon AF electret/air interface

6.2.1 Open Circuit Sensitivity

The open circuit sensitivity of the microphone can be divided into two separate components: mechanical and electrical sensitivity. The sound waves impinge on the diaphragm and move the diaphragm; thus the mechanical sensitivity determines the softness of the diaphragm. Then, the diaphragm moves and the capacitance of the microphone changes to induce a small electric signal. Thus, the electrical sensitivity determines the magnitude of the electric signal related to the diaphragm movement.

As shown earlier in eq. 2-10 (please refers to eq. 2-10 for all the symbols), the load-deflection relationship of a diaphragm can be described as:

$$P = \frac{C_1 \sigma t h}{a^2} + \frac{C_2 E t h^3}{a^4} \tag{6.2}$$

where C_1 and C_2 are 3.04 and 1.83 respectively for a square diaphragm. For microphone applications, the second term due to Young's modulus is usually neglected because

$$\frac{C_1 \sigma}{C_2 E}\left(\frac{a^2}{h^2}\right) >> 1 \tag{6.3}$$

for most of cases. Therefore, the mechanical sensitivity can be written as:

$$S_m = \frac{h}{P} = \left(\frac{a^2}{3.04t\sigma}\right) \quad (m/Pa) \tag{6.4}$$

In eq.6-4, the deflection h is in the center of diaphragm (where the largest deflection takes place), so the overall movement is usually averaged with a factor of ½. Therefore, the mechanical sensitivity is:

$$S_m = \frac{h}{P} = \left(\frac{a^2}{3.04t\sigma}\right)\left(\frac{1}{2}\right) \quad (m/Pa) \tag{6.5}$$

The electrical sensitivity is coming from the induced electrical signal while the air gap distance changes during the movement of the diaphragm. Therefore, this system can be calculated using the same charging model as shown previously in Fig. 5-10 (redrawn in Fig. 6-3) with an external voltage source V=0. Therefore,

$$\sigma_1(r) = -\frac{V + \sigma_p \frac{d_d}{\varepsilon_d}}{\frac{d_g - z}{\varepsilon_g} + \frac{d_d}{\varepsilon_d}} = -\frac{\sigma_p}{\frac{C_d'}{C_g'} + 1} = -\frac{\sigma_p}{\frac{\varepsilon_d}{d_d}\frac{d_g}{\varepsilon_g} + 1}$$

$$S_e = E_g = -\frac{\sigma_1}{\varepsilon_g} = \frac{\sigma_p / \varepsilon_g}{\frac{\varepsilon_d}{d_d}\frac{d_g}{\varepsilon_g} + 1} \quad \text{(V/m)} \tag{6.6}$$

Thus, the overall sensitivity of microphone can be calculated as:

$$S_{oc} = (S_m)(S_e) = \left(\frac{a^2}{6.08t\sigma}\right)\left(\frac{\sigma_p / \varepsilon_g}{\frac{\varepsilon_d}{d_d}\frac{d_g}{\varepsilon_g} + 1}\right) \quad \text{(V/Pa)} \tag{6.7}$$

6.2.2 Frequency Response

The frequency response of the microphone can be thought of as a band pass filter. The frequency cut off would be determined by the acoustic holes on the backplate. The acoustic hole on the back plate is initially used to prevent the moving diaphragm from damping, and also to prevent the microphone from having an un-desired DC-response to ambient pressure changes. However, at low frequency, a small portion of the sound wave would be able to leak through the back chamber and equalize the pressure difference across the moving diaphragm; at this point, the overall sensitivity of microphone begins to suffer. The other factor that would determine the low frequency cut off is the overall transfer function of the system. Microphones are usually equipped with a high-impedance pre-amplifier and therefore, the overall system works as a high-pass filter. Thus, the low frequency cut-off from the overall equivalent circuit response would usually determine the actual low-frequency cut-off.

The ideal high-frequency cut-off [5] should be determined by the mechanical frequency response of the moving diaphragm (electronics bandwidth are usually higher than 20KHz) as:

$$f_0 = \sqrt{\frac{\sigma}{2a^2\rho}} \tag{6.8}$$

σ : residual tensile stress in the membrane $[\mathrm{N/m^2}]$
a : square membrane size [m]
ρ : density of the membrane material $[\mathrm{kg/m^3}]$

However, the air would unavoidably damp any mechanical system that is not operated under vacuum. In the microphone case, the situation is much worse because the air gap between the diaphragm and back plateis usually only several microns wide. Therefore, the acoustic holes are important. Ideally, the back plate should have many

large holes to prevent the moving diaphragm from damping. However, the back plate also provides the other electrode for capacitive sensing. By increasing the hole size and the number of holes, the capacitance would be significantly decreased and more prone to the effect of stray capacitance. The air-damping effect has been modeled [6] by calculating an equivalent air-streaming resistance as:

$$R_a = \frac{12\eta_a a^2}{n\pi s_a^3}\left(\frac{1}{4}\ln\frac{1}{F} - \frac{3}{8} + \frac{F}{2} - \frac{F^2}{8}\right) \tag{6.9}$$

η_a : viscosity of the air [$17.1*10^{-6}$ Ps - s]
a : square membrane size [m]
n : number of acoustic holes per unit area [$/m^2$]
s_a : air gap thickness [m]
F : fraction of backplate covered by acoustic hole

and if the diaphragm is strongly damped by fulfilling the following criteria,

$$\frac{0.5R_a}{\sqrt{MK}} \geq 1 \tag{6.10}$$

M : diaphragm mass [kg]
K : stiffness of the diaphram ($13.57\sigma t$ for square membrane) [N/m]
n : number of acoustic holes per unit area [$/m^2$]

The overall microphone system can be treated as two 1st order systems in a series and the fundamental frequency of the system can be calculated as:

$$f_{streaming} = \left(\frac{K}{2\pi R_a}\right) \text{ [Hz]} \tag{6.11}$$

It is clear from eq. 6-11 that the frequency response would be significantly improved by reducing the streaming resistance. It is important to note, however, that reducing the streaming resistance would decrease the sensitivity of the microphone.

6.2.3 Dynamic Range

The dynamic range of the microphone is defined as the range of acoustic pressure that a microphone can sense. For most cases, the electronics rather than the microphone itself would determine the maximum and minimum bounds of the dynamic range. This section will focus on calculating the fundamental limit of microphone.

The upper limit of the microphone is reached when the pressure is large enough to push the diaphragm to the backplate (the sound level would be distorted before this occurs). The pressure required to do so can be calculated by eq.6.2 by setting the deflection to the air gap height.

The lower limit of the microphone would be determined by the thermal motion of the diaphragm itself [7]and can be calculated as:

$$P_n = \sqrt{4kT(\frac{R_a}{a^4})\delta f} \text{ [Pa]} \tag{6.12}$$

In this section, the fundamental parameters of designing an electret microphone have been given. The next section will focus on the electret material itself and how to implant electrons into the electret.

6.3 The Electret – The Material and Formation

An electret is a dielectric that produces an external electric field from quasi-permanent electrical charges trapped inside the material. Over the past several decades, many different electret materials have been proposed and demonstrated, such as polyethylene, methacrylate, aluminum oxides, or even silicon dioxides.

By far, the most stable electrets [8] are still those made from polytetrafluoroethylene (PTFE), polyfluoroethylenepropyle (FEP), and polystyrene (PS)

because of their high charge-retention capability (10^{-5} to 10^{-4} C/m^2) and stability (-20 to 100°C). However, these materials are insoluble below 300°C, and therefore cannot be spin-cast as a polymer suspension for MEMS thin-film applications. Thus, this section will focus on the newly synthesized Teflon AF 1600 from Dupont and the charge implantation method developed for this thin-film.

Table 6-1: Selected properties for Teflon AF1601S

Property	ASTM Method	Unit	Value
Physical and Mechanical Properties			
Glass Transition Temperature	D3418	°C (°F)	160 (320)
Tensile Strength	D638	MPa	27
Ultimate Elongation	D638	%	15
Tensile Modulus	D638	GPa	1.55
Volume Coefficient of Thermal Expansion	E831	ppm/°C	260
Specific Gravity	D792		1.78
Melt Viscosity	D3835	Pa·sec	5000 at 250°C (482°F), 100 sec^{-1}
Electrical Properties			
Dielectric Constant	D150	at 1 MHz	1.934
		at 3.5 MHz	1.933
		at 9.5 MHz	1.933
		at 100 MHz	1.933
		at 1 GHz	1.930
		at 3 GHz	1.928
		at 8.5 GHz	1.927
		at 13.6 GHz	1.927
Dissipation Factor	D150	at 1 MHz	0.00012
		at 3.5 MHz	0.00012
		at 9.5 MHz	0.000073
		at 100 MHz	0.000099
		at 1 GHz	0.00018
		at 3 GHz	0.00022
		at 8.5 GHz	0.00015
		at 13.6 GHz	0.00020
Other Properties			
Optical Transmission	D1003	%	>95%
Refractive Index	D542	–	1.31
Contact Angle with Water		degrees	104
Critical Surface Energy		dynes/cm	15.7
Brookfield Viscosity in Fluorinert FC-75		Pa·sec	5500 at 18 wt%
Water Absorption	D570	%	<0.01
Solubility in Fluorinert FC-75		%	25–30 wt% at RT

6.3.1 Teflon AF thin film

The Teflon AF is a newly synthesized amphorous polytetrafluoroethylene derivative suspended in various perfluorinated solvents (Fluorient, Flutec, and Galden), which allows the Teflon AF to be spin-cast using regular photoresist processs [9, 10]. Specifically, AF 1601S (see Table 6-1 for properties) is chosen for our purposes for its low viscosity, therefore allowing us to create thin-films of 0.5 to 2.5μm for the MEMS microphone process.

The detailed electret preparation method can be found elsewhere [9] which involves a two-step baking process. First, the sample spun with Teflon AF is baked at 100°C for 45 minutes to get rid of most of the solvent. Second, the sample is baked at 170°C for another 15 minutes. This second step is to re-flow the Teflon AF to achieve uniformity of the film and to enhance the adhesion. (The glass transition temperature T_g of Teflon AF 1600 is around 165°C.)

6.3.2 Charge implantation method

The electrons are buried into the Teflon film by using Back-Lighted-Thyratron (BLT) as shown in Fig. 6-4. The BLT [4, 11] is triggered by external UV light-pulse to break down the helium gas and to generate free electrons. The electrons are subsequently drawn by the strong electric field up to 20KV towards to the anode where the sample is located.

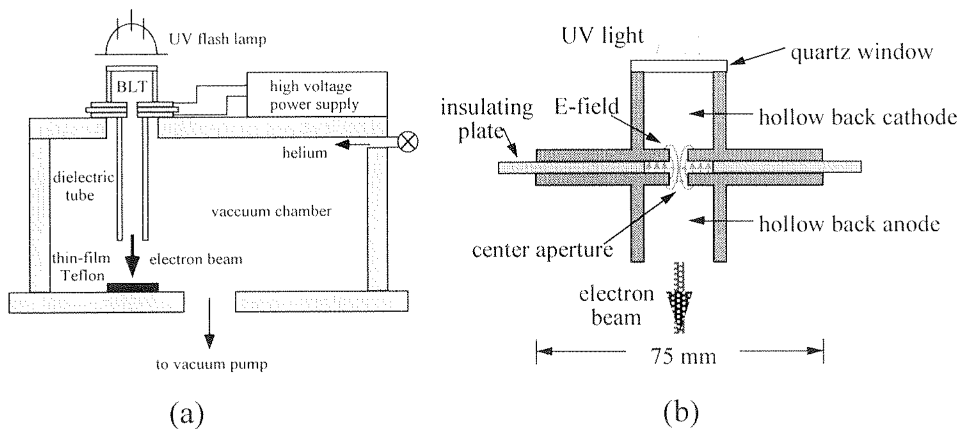

Fig. 6-4: The Back-Lighted Thyratron

(a) The schematic of the overall system

(b) The schematic of the working principle

The stability of Teflon electrets generated using BLT has been calibrated [9]. The Teflon AF electret generated by BLT (see Fig. 6-5[9]) has the capability to hold negative charges with densities from 10^{-4} to 10^{-5} C/m^2 and a relaxation time longer than 3 years. This result is not surprising because the dielectrics relaxation time of Teflon can be calculated as:

$$\tau = \frac{\varepsilon}{\sigma} \geq 100 \; years \tag{6.13}$$

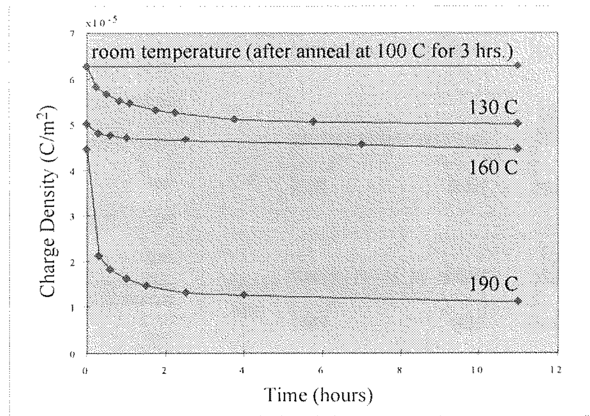

Fig. 6-5: The Teflon AF electret generated by BLT at various annealing temperatures

In this section, the Teflon AF electret has been discussed in terms of material processing and electret generation. In the next section, a MEMS electret microphone will be designed and fabricated to achieve an open-circuit sensitivity larger than 10mV/Pa and a bandwidth larger than 10KHz.

6.4 Designs and Fabrication of a MEMS Electret Microphone

In this section, a MEMS electret microphone will first be designed to achieve an open sensitivity larger than 10mV/Pa with a frequency response of 10KHz. Second, the designed microphone will be fabricated with micromachining technologies discussed in the earlier chapters and Parylene will be used to both increase the yield and rigidity of the plate.

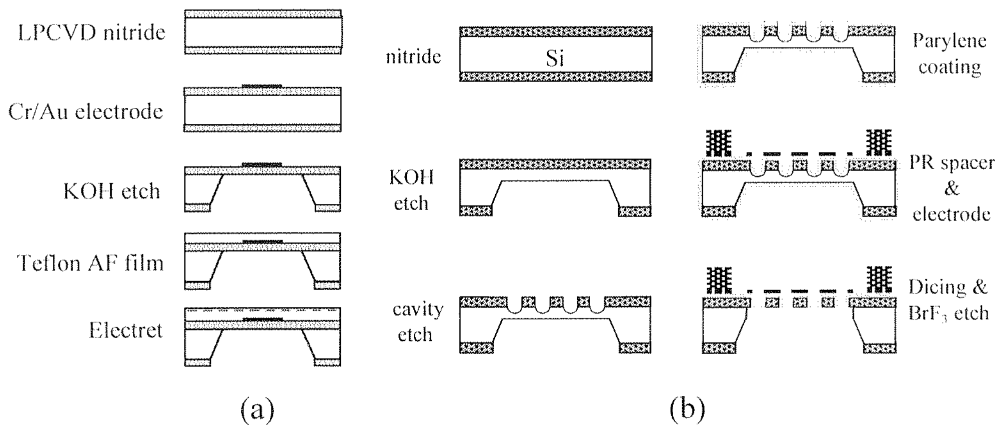

Fig. 6-6: Simplified fabrication Process flow for an electret microphone
(a) The moving diaphragm
(b) The back plate with acoustic holes

6.4.1 Fabrication Process and Issues

Shown in Fig. 6-6 [11] are the fabrication steps used for the electret microphone, which includes both the moving diaphragm and the rigid backplate. Diaphragm formation begins with a 4'' silicon substrate coated with 0.5 μm low stress LPCVD silicon nitride. Then, 1000 Å Cr/Au is evaporated and patterned for the electrode. KOH is used to anisotropically etch the backside of the substrate to form an 8mm × 8mm free-standing nitride membrane. Teflon AF is then spun over the front surface of the membrane to a thickness of 0.9 μm and baked at 250°C for 3 hours to drive off the Fluoroinert® FC-75 solvent. Electrons with 7-10 keV of energy are then implanted into the Teflon using a

Back-Lighted Thyratron. The electret is then stabilized by baking at 100°C in air for three hours. For the electret microphone reported in this thesis, a charge density on the order of 10^{-4} C/m^2 was obtained, as measured by the charge compensation method by Monroe Isoprobe [12].

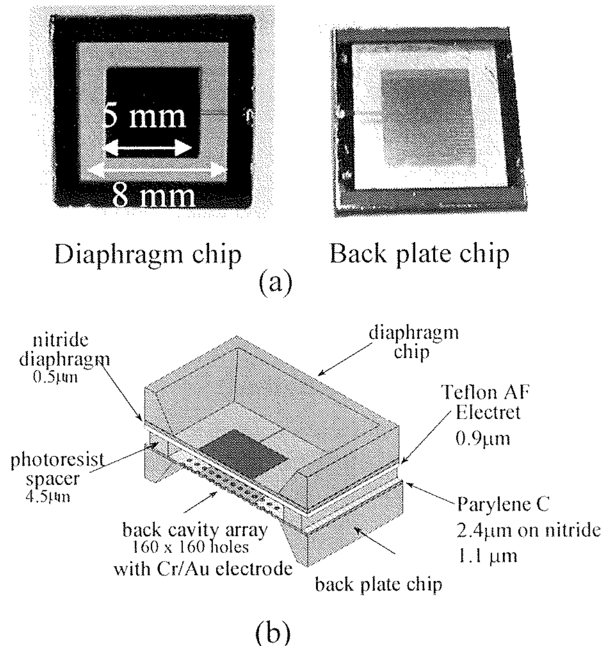

Fig. 6-7: Photos of fabricated microphone chips
(a) Diaphragm and back plate chip (b) Schematic of the package

The back plate of the microphone is fabricated from a 4'' silicon substrate coated with 1.1 μm thick low stress LPCVD silicon nitride. A KOH anisotropic bulk etch is also used to form a 20 μm thick silicon diaphragm. A 160 × 160 array of holes is then etched 5 μm deep into the silicon membrane. Each hole with a diameter of 30μm is spaced 50μm apart (center-to-center). A 2.4μm layer of Parylene C is then deposited to the front side of the wafer. This step is critical because silicon nitride as a rigid material has a fracture strain of around 2.8% [13]. A fabricated silicon nitride diaphragm with a large percentage of acoustic holes would be fragile and induce overall low yield [14]. The Parylene/silicon nitride composite diaphragm first used to increase the burst pressure of

the microfilter[14] is therefore adapted here to increase the yield of the back plate used in microphone application.

After the deposition of Parylene, a 1000Å thick Cr/Au electrode is then deposited and patterned. A 5 μm thick hard-baked photoresist spacer is used to define the air gap between the electrodes. The final step involves a BrF_3 etch which frees the perforated back plate nitride membrane. Fig. 6-7 shows pictures of the microphone diaphragm and back plate.

6.4.2 Designs of a MEMS Electret Microphone

The open circuit sensitivity of the microphone can be calculated from eq. 6.7. If t=1μm, σ=100Mpa (optimistic estimation), a=8mm, $\sigma_p=10^{-4}$ C/m^2, d_g=5μm, and d_d=1μm, the open sensitivity should be:

$$S_{oc} = (S_m)(S_e) = \left(\frac{a^2}{6.08t\sigma}\right)\left(\frac{\sigma_p/\varepsilon_g}{\frac{\varepsilon_d}{d_d}\frac{d_g}{\varepsilon_g}+1}\right)(R) \approx 30\,(\text{mV/Pa}) \tag{6.13}$$

where R=0.273 is used to account for the fill factor of the backplate. Certain areas on the back plate are covered with acoustic holes and thus not used for sensing. The bandwidth of the microphone can be calculated with eq.6-11 where

$$\begin{aligned} R_a &= \frac{12\eta_a a^2}{n\pi s_a^3}\left(\frac{1}{4}\ln\frac{1}{F}-\frac{3}{8}+\frac{F}{2}-\frac{F^2}{8}\right) \approx 0.006\ \text{Ns/m} \\ n &: 4*10^8\ [/\text{m}^2]\,(160*160\ \text{holes}, 30\mu\text{m in diameter}) \\ F &: 0.273 \\ f_{streaming} &= \left(\frac{K}{2\pi R_a}\right) \approx 35\ \text{kHz} \end{aligned} \tag{6.14}$$

However, because eq. 6-10 is not satisfied, the above bandwidth may be overestimated.

The maximum input level of the microphone is calculated using eq. 6-2 to give a value larger than 120 dB SPL and a value of almost zero dB SPL for the lowest noise level (with eq. 6-12). Most importantly, to prevent the charging phenomena that was observed in the previous chapter, the electric field across the air gap has to be examined. According to eq. 6-6:

$$E_g = -\frac{\sigma_1}{\varepsilon_g} = \frac{\sigma_p / \varepsilon_g}{\frac{\varepsilon_d}{d_d}\frac{d_g}{\varepsilon_g} + 1} \approx 1\,(\mathrm{MV/m}) \qquad (6.15)$$

The 1 MV/m electric field is below the safety limit of 3MV/m. Therefore, the charging effect and its associated high pull-in voltage should not be an issue. However, if the potential optimization of the microphone is required to increase the sensitivity, careful consideration has to be given for the ionization of air in-between the air gaps, especially because Teflon has a much higher resistivity compared to Parylene.

In this section, an electret microphone has been designed and fabricated. Parylene is used to increase the overall yield of the back plate chip. Without a reinforced Parylene layer, the silicon nitride would usually be broken especially under such high-perforation ratio. The electric field intensity inside the air gap is investigated to prevent the undesired charging effect, which would significantly lower the sensitivity of microphone.

6.5 Testing of a MEMS electret Microphone

The frequency response and open circuit sensitivity of the electret microphone is measured using a Standard Research Systems Model SR785 Dynamic Signal Analyzer to apply an input sound level from 100Hz to 12.896KHz in a Brüel & Kjaer (B&K) Type 4232 anechoic test chamber. The devices is packaged with a custom-made package (see Fig. 6-7.)

The measured microphone has a relatively flat frequency response of 45mV/Pa from 100Hz to 10KHz. This result is somewhat higher than the expected sensitivity of 45mV/Pa; the reason for this sensitivity is because the electron density is higher than the expected 10^{-4}C/m^2. The theoretical calculation show that the electron density should be around $1.5*10^{-4}$C/m^2.

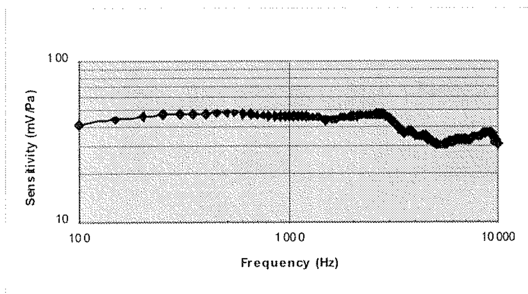

Fig.6-7: The frequency response of the electret condenser microphone

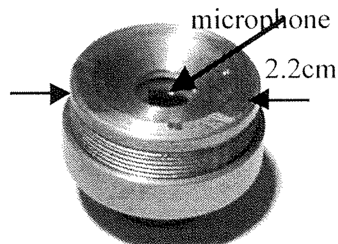

Fig.6-8: The custom-made package for electret microphone measurement

The measured noise level of the MEMS electret microphone (with B&K Type 2669 preamplifier) is less than 30dB SPL at 20°C. The open circuit distortion limit of the electret microphone was found to be above 110 dB SPL (the maximum output of the anechoic sound chamber speaker). This test was conducted at 650 Hz and the measured

Total Harmonic Distortion of the electret microphone was less than 1 %. Given that the lowest detectable sound pressure level is 30 dB SPL, this translates into a microphone dynamic range that is greater than 80 dB SPL.

6.6 Conclusion

In this chapter, a Teflon AF-based electret microphone is designed, fabricated and tested. The demonstrated microphone has an open circuit sensitivity of up to 45mV/Pa with a bandwidth larger than 10KHz. More importantly, to avoid the air-gap breakdown and associated charging problems discussed in Chapter 5, the electric field between the air gap is controlled to be around 1MV/cm. Therefore, to apply an electrostatic force across microgaps with dielectrics in between, the electric field has to be designed to be lower than the initial breakdown field (approximately 3MV/m). However, the demonstrated electret technology can be used to design various electrostatic sensors such as accelerometers, gyroscopes, and vibration sensors.

6.7 References

[1] R. Schellin and G. Hess, "A Silicon Subminiature Microphone Based on Piezoresistive Polysilicon Strain Gauges," *Sensors and Actuators A*, vol.32, pp. 555-559, 1992.

[2] P. R. Scheeper, A. G. H. v. d. Donk, W. Olthuis, and P. Bergveld, "A Review of Silicon Microphones," *Sensors and Actuators A*, vol. 44, pp. 1-11, 1994.

[3] J. Bernstein, K. Houston, L. Niles, S. Finberg, H. Chen, L. E. Cross, K. Li, and K. Udayakumar, "Micromachined Ferroelectric Transducers for Acoustic Imaging," Proceedings of Transducers '97, the 1997 International Conference on Solid-State Sensors and Actuators, Chicago, IL, 1997.

[4] T. Y. Hsu, "A Novel Electron Beam Source Based on the Back-Lighted Thyratron," Ph.D thesis, University of Southern California, 1992.

[5] R. D. Blevins, *Formulas for Natural Frequency and Mode Shapes*. New York, Van Norstrand Reinhold Company, 1979.

[6] Z. Skvor, "On the Acoustical Resistance due to Viscous Losses in the Air Gap of Electrostatic Transducers," *Acoustica*, vol.19, pp. 295, 1967.

[7] T. B. Gabrielson, "Mechanical -Thermal Noise in Micromachined Acoustic and Vibration Sensors," *IEEE Transactions on Electon Devices*, vol. 40, pp. 903-909, 1993.

[8] G. M. Sessler, *Electrets,* 2nd ed. Darmstadt, Springer-Verlag, 1987.

[9] W. H. Hsieh, "MEMS Thin Film Teflon Electret Condenser Microphones," Ph.D. thesis, California Institute of Technology, 2000.

[10] W. H. Buck and P. R. Resnick, "Properties of Amphorous Fluoropolymers Based on 2,2-Bistrifluoromethyl-4,5-Difluro-1,3-Dioxole," 183rd Meeting of the Electrochemical Society, Honolulu, HI, USA, 1993.

[11] W. H. Hsieh, T. J. Yao, and Y.C. Tai, "A High Performance MEMS Thin-film Teflon Electret Microphone," 1999 International Conference on Solid-State Sensors and Actuators (Transducers '99), Sendai, Japan, 1999.

[12] Instruction Manual: Isoprobe Electostatic Voltmeter Model 244A, "Monroe Electronics," New York, 1991.

[13] X. Yang, "Micromachined Silicone Rubber Membrane Valves for Fluidic Applications," Ph.D. thesis, California Institute of Technology, 1999.

[14] X. Yang, J. M. Yang, X. Q. Wang, E. Meng, Y. C. Tai, and C. M. Ho, "Micromachined Membrane Particle Filter," 1998 The Eleventh Annual International Workshop on Micro Electro Mechanical Systems (MEMS '98), Heidelberg, Germany.

CHAPTER 7

Conclusion

This thesis described the development of Parylene-based MicroElectroMechanical Systems (MEMS) technologies and their applications for many micromachined devices. The design, fabrication, and testing of devices such as a thermopneumatic microvalve, an in-channel integrated microflow restrictor, and an electret microphone were presented in this thesis. Parylene, with the ability of being CVD-deposited at room-temperature, provides an alternative material selection for integrating micromachined devices on post-CMOS wafers obtained from foundry services.

First, the properties of Parylene, which includes electrical, mechanical, thermal, and surface properties, were examined specifically for micromachining applications in Chapter 2. The dielectric strength of Parylene was determined to be around 250V/μm. The mechanical properties, in particular the Young's modulus and residual stresses, were tested using micromachining fabricated structures. The surface properties of Parylene, which could significantly influence the flow characteristics in microchannels, were then calibrated using contact-angle measurements and the marching meniscus method.

With the high-elongation-to-break and good solvent barrier characteristics of Parylene, a thermopneumatic microvalve with a silicone/Parylene composite membrane was built and tested in Chapter 3 for gas flow up to several slpm. The lowest power consumption to turn off the gas flow was determined to be around 73mW. In the second part of Chapter 3, a microfluidic coupler using silicone was also demonstrated and tested

for the packaging of the microvalve developed in the first part of Chapter 3. Chapter 4 dealt with one of the most notorious problems in the surface micromachining field—stiction. Surface tension generated from the drying processes easily pulls down the Parylene microstructures due to its low Young's modulus. A combined wet-acetone photoresist and dry BrF_3-etch process were developed to overcome this problem. The demonstrated Parylene microstructures are larger than mm*mm size using the developed process.

In Chapter 5, the charging problems on Parylene electrostatic actuators were studied. The "bounce-back" issues on polymer-based electrostatic actuators were studied in detail for the first time. Parylene, being a good electrical insulator, causes several undesired parasitic charging problems when it is used between air gaps in electrostatic actuators. The electric field, when larger than 3MV/m, easily breaks down (ionizes) the air molecules and causes charges to be deposited on the Parylene/ air interface. In the second part of Chapter 5, the design of an in-channel microflow restrictor was presented. The in-channel approach of microfluidic components has an inherent advantage of small dead-volume. Furthermore, no electric field would be dropped across the fluids. The high electric field, which may potentially influence the charged species in the fluids to be attracted on the electrodes for actuation purpose, is eliminated. An ac-actuated in-channel flow restrictor (originally a microvalve) was demonstrated to modulate the microchannel flow of tens of nl/min at several psi inlet pressure. The demonstrated flow restrictor can create an ON/OFF flow rate ratio up to 200%.

In Chapter 6, an electret microphone with a thin-film Teflon AF electret was demonstrated. Parylene was used in the fabrication of the microphone to increase the

rigidity of the back plate and therefore to increase the overall yield. The demonstrated microphone was designed in such a way that the electric fields inside the air gaps is much lower than the safety limit (3MV/m), in order to avoid the charging phenomena that was discussed previously in Chapter 5. The microphone, with an open circuit sensitivity 45mV/Pa and bandwidth of larger than 10KHz, can potentially be integrated with CMOS amplifying electronics. Although the electret technology in Chapter 6 was only explored for microphone applications, it could also be explored for many different sensor applications such as accelerometers, vibration sensors, or even micropower generators.

To avoid charging problems, the research focused on choosing alternative sacrificial layer materials that could be compatible with metal evaporation/sputtering and patterning process, so the dielectrics could be avoided in-between the air gaps in electrostatic actuators.

Nevertheless, to fully utilize its room-temperature CVD-deposited characteristics, further research on Parylene is necessary. First, one of the reasons that semiconductors have had such tremendous applications is that the conductivity of the material can be controlled (or the material can be doped). As seen in Chapter 5 for electrostatic devices, an extra step has to be taken to put down the metal as electrodes. If the conductivity of Parylene can also be manipulated, this extra step (which often causes problems) is unnecessary. Future research could be focused on a new synthesized CVD-deposited Parylene derivative in which the conductivity can be controlled. Using another approach, as conductive polymers have emerged on the market, it may also be possible to mix Parylene with conducting polymers to control its conductivity and eliminate the extra metal evaporation/sputtered steps. However, conductivity of conducting polymer (usually

PH-related) is usually not compatible with many chemical processes used in fabrication. Therefore, a new process may have to adapt the necessary changes associated with the conducting polymers.

Moreover, the integration of microfluidic devices such as pumps, valves, and mixers to reach the ideal "lab-on-the-chip" using Parylene still requires lots of effort. The ideal approach should be able to demonstrate various microfluidic components using a simple, uniform platform without affecting the analytes in microchannel.

Finally, Parylene (as mentioned earlier) as a room-temperature CVD deposited material does provide an alternative material selection as discussed in this thesis. The future work should extend the research effort not only to Parylene but also to other polymers, which offer many different properties that could be tailored for specific applications. The study in this thesis (stiction-reduction, charging) hopefully could (theoretically could) also well apply to other polymer MEMS devices.